

University of Windsor

Scholarship at UWindor

Electronic Theses and Dissertations

Theses, Dissertations, and Major Papers

2013

Theory of a Hybrid Plasmonic - Waveguide Biosensor for the Detection of Turbid Analytes

Daniel-Anthony Travo
University of Windsor

Follow this and additional works at: <https://scholar.uwindsor.ca/etd>

Recommended Citation

Travo, Daniel-Anthony, "Theory of a Hybrid Plasmonic - Waveguide Biosensor for the Detection of Turbid Analytes" (2013). *Electronic Theses and Dissertations*. 4936.
<https://scholar.uwindsor.ca/etd/4936>

This online database contains the full-text of PhD dissertations and Masters' theses of University of Windsor students from 1954 forward. These documents are made available for personal study and research purposes only, in accordance with the Canadian Copyright Act and the Creative Commons license—CC BY-NC-ND (Attribution, Non-Commercial, No Derivative Works). Under this license, works must always be attributed to the copyright holder (original author), cannot be used for any commercial purposes, and may not be altered. Any other use would require the permission of the copyright holder. Students may inquire about withdrawing their dissertation and/or thesis from this database. For additional inquiries, please contact the repository administrator via email (scholarship@uwindsor.ca) or by telephone at 519-253-3000ext. 3208.

Theory of a Hybrid Plasmonic – Waveguide Biosensor for the Detection of Turbid Analytes

by

Daniel-Anthony Travo

A Thesis

Submitted to the Faculty of Graduate Studies
through the Department of Physics in Partial Fulfillment
of the Requirements for the Degree of Master of Science at the
University of Windsor

Windsor, Ontario, Canada
2013

© 2013 Daniel-Anthony Travo

All Rights Reserved. No part of this document may be reproduced, stored or otherwise retained in a retrieval system or transmitted in any form, on any medium by any means without prior written permission of the author.

Theory of a Hybrid Plasmonic – Waveguide Biosensor for the Detection of Turbid Analytes

by

Daniel-Anthony Travo

APPROVED BY:

G. W. F. Drake, Department Reader
Department of Physics

R. J. Caron, Outside Department Reader
Department of Mathematics and Statistics

C. Rangan, Advisor
Department of Physics

University of Windsor

August 9, 2013

Author's Declaration of Originality

I hereby certify that I am the sole author of this thesis and that no part of this thesis has been published or submitted for publication. I certify that, to the best of my knowledge, my thesis does not infringe upon anyones copyright nor violate any proprietary rights and that any ideas, techniques, quotations, or any other material from the work of other people included in my thesis, published or otherwise, are fully acknowledged in accordance with the standard referencing practices. Furthermore, to the extent that I have included copyrighted material that surpasses the bounds of fair dealing within the meaning of the Canada Copyright Act, I certify that I have obtained a written permission from the copyright owner(s) to include such material(s) in my thesis and have included copies of such copyright clearances to my appendix. I declare that this is a true copy of my thesis, including any final revisions, as approved by my thesis committee and the Graduate Studies office, and that this thesis has not been submitted for a higher degree to any other University or Institution.

Abstract

The characterization of turbid media, such as colloidal suspensions such as milk, is a challenging task due to the attenuation of incident fields within the medium. In this work, the potential performance of a novel sensing technology is assessed for the characterization of such media. The device is a hybrid plasmonic-waveguide biosensor and consists of an array of gold nanoparticles deposited atop a waveguide multilayer structure. The performance of the device is modelled using a Green function approach and is benchmarked to a surface plasmon resonance (SPR) sensor. The results of the analysis show the hybrid sensor to be several orders of magnitude more sensitive to changes in the turbid medium than the SPR sensor.

This work is dedicated to my friends and family, whose support and encouragement were as valuable as the physical techniques and computers I used to complete this work.

Acknowledgements

This work would not have been possible without the guidance of my supervisor Dr. Chitra Rangan. Her patience and mentorship throughout both my undergraduate and Master's work has served as a cornerstone to the development of my research abilities. For this I gratefully acknowledge and thank her for her involvement in this process. Additionally, I would like to thank Dr. John Sipe, who helped develop the initial work this project was based on. This project would not have been possible without his insights and advice. I would also like to thank the members of my committee Drs. Gordon Drake and Richard Caron, both of whom have taught me many skills in the fields of physics and mathematics that I hope to use for many years to come.

Finally, I would like to acknowledge the University of Windsor for the Master's Entrance Scholarship and the NSERC Strategic Network for Bioplasmonic Systems for funding this project.

Contents

Author's Declaration of Originality	iv
Abstract	v
Dedication	vi
Acknowledgements	vii
List of Figures	xi
1 Introduction	1
1.1 Motivation	1
1.2 Light Propagation through Turbid Media	2
1.3 Surface Plasmons and Localized Modes	4
1.4 Other Sensing Platforms	6
1.5 Discussion of Validity of Approximations	6
1.6 Overview of Thesis	8
2 Formalism and Theory	9
2.1 Device Schematic	10
2.2 Conventions and Notation	12
2.3 Assumptions	14
2.4 Method Development	15
2.5 Determining the Selvege Fresnel Coefficients	16
2.6 Determining the Dipole Polarizabilities of the Nanoparticle Array	20

3	Effects of the Finite Layer	23
3.1	Image Electric Field via Green Function Approach	24
3.2	Verification of Image Dipole Contributions Through The Method of Images	27
3.3	Response of the Selvedge to the Additional Image Terms	30
3.4	The Solution Condition for the Waveguide Modes	34
3.5	The Expansion Parameter: ρ_{14}	37
3.6	Limiting Cases	40
3.7	Effects of D_2 on the Hybrid Sensor	42
4	Characterization of Turbid Media	45
4.1	Solution Condition	46
4.2	Expansion Parameter	47
4.3	Limiting Cases	50
4.4	Effects of $\Im(\varepsilon_I)$ on the Hybrid Sensor	51
5	Results	53
5.1	Figure of Merit	53
5.2	Optimal Nanoparticle Configurations and Effects of Particle Size and Spacing	54
5.3	Results for Transparent Media	58
5.4	Results for Turbid Media	59
6	Discussion and Conclusions	61
6.1	Discussion of the Results	61
6.2	Summary of Original Contributions	62
6.3	Conclusions	64
6.4	Future Work	64
A	Integrals Involving Angular Dependence and Bessel Functions	66
B	List Green Functions	72
C	Codes	75

D Copyright Releases	95
Bibliography	97
VITA AUCTORIS	105

List of Figures

2.1	Diagram of the hybrid plasmonic waveguide sensing structure. Here $h = b$ to treat spherical particles, however the method applies to more general geometries for which this may not be true.	11
2.2	Scattering plane shown for s and p-polarized electric fields. Both cases are drawn such that the incident wavevectors of the fields begin in an initial medium characterized by ε_{inc} before impinging upon an interface, the plane of incidence and partially transmitting into a second medium $\varepsilon_{\text{trans}}$	13
2.3	Breakdown of wavevector components in the Cartesian grid system.	13
3.1	Orientation of κ and R in the xy plane.	25
3.2	Effects of various finite layer thicknesses, D_2 on the changes in absorption spectra and waveguide mode results. Particle size and spacing are $b=5$ nm and $a=25$ nm, respectively.	43
3.3	Plots showing the relationship between κ_o and κ'_o as a function of the thickness of the tethering layer for the GNP sensor.	44
4.1	Effects of various imaginary dielectric constants, $\Im(\varepsilon_1)$ on the changes in absorption spectra and waveguide mode results.	52
5.1	Plots of H_1 for nanoparticle arrays with a constant radius of 5 nm and varying interparticle spacings a for (a) a changing real component of the cladding dielectric constant $\partial\varepsilon_{1r}$ and (b) a changing imaginary component $\partial\varepsilon_{1i}$	55
5.2	Comparison of the Taylor series approximation for H_1	56

5.3	H_1 spacing and size eigenvalues over visible spectrum.	57
5.4	H_1 results for a varying $\Re(n_1)$ with the imaginary component held fixed at $\Im(n_1) = 0$ for (a) the SPR sensor and (b) the hybrid sensor. For the hybrid sensor, particles have a radius of 5 nm and are separated by an interparticle spacing of 25 nm.	58
5.5	H_1 results for a varying $\Re(n_1)$ with the imaginary component held fixed at $\Im(n_1) = 0.00618$ for (a) the SPR sensor and (b) the hybrid sensor. For the hybrid sensor, particles have a radius of 5 nm and are separated by an interparticle spacing of 25 nm.	59
5.6	H_1 results for a varying $\Im(n_1)$ with the real component held fixed at $\Re(n_1) = 1.36$ for (a) the SPR sensor and (b) the hybrid sensor. For the hybrid sensor, particles have a radius of 5 nm and are separated by an interparticle spacing of 25 nm.	60

Chapter 1

Introduction

1.1 Motivation

The focus of this work is to examine the potential of a novel type of sensing structure for the characterization of turbid media. The term “turbid” characterizes a medium as a mixture of a host matrix and a distribution of particulates. Examples of such mixtures include many everyday items such as crude petroleum, blood, and milk. For nearly a century a great deal of research has focused on the development of characterization techniques for use with industrial applications [1–6]. One particularly active area, is the characterization of milk to determine its quality and fat content [7–12].

An electromagnetic wave passing through a turbid medium is attenuated because of absorption and scattering. This attenuation is described by a complex refractive index for the medium, in which the imaginary component is proportional to the amount of absorption and scattering. The real component of the medium’s refractive index is still related to the refraction of the wave as it crosses an interface between two media. The many characterization approaches for transparent materials are ineffective for turbid media because of the complicated nature of the optical response of the media. Additional difficulties in modelling arise due to multiple scattering of the incident field. Successful models are used in conjugation with experimental results to determine the optical properties of the

material [6, 13–16].

Optical techniques are often sought for their rapid characterization capabilities. In addition to this, optical methods are amenable to integration within electronic platforms [17–19]. These reasons have led to their widespread use in industry, specifically engineering applications [20–28]. For example, a precise method of characterizing a transparent medium is reflectometry [29]. By determining the angle at which an incident beam experiences total internal reflection, known as the critical angle, a simple and accurate fit can be performed using Snell’s law $n_2 = n_1 \sin \theta_{crit}$. For transparent media, a reflectance profile experiences a significant increase near the critical angle. However, for turbid media the increase is much more gradual, reducing the precision of the results [6, 14, 30–34]. Another popular form of analyte detection and medium characterization is the use of surface plasmon resonance (SPR) sensors. Common to biomedical applications, the sensitivity of these sensors have been shown to match reflectometry measurements for turbid media [35]. SPR sensors are also used for the characterization of turbid media through phase extraction techniques [36–42].

In this work, I have analyzed a hybrid plasmonic-waveguide sensor for the characterization of turbid media. The sensor consists of a layer of gold nanoparticles deposited atop a glass waveguide, affixed to a substrate. For transparent media, it has been predicted to be comparable to SPR sensors [43], for detecting changes in the surrounding dielectric medium while surpassing SPR sensitivity with respect to immobilized analyte detection. The behaviour of the SPR sensor is fundamentally different in that s-polarized light (see section 2.2) cannot excite surface plasmons [44, 45]. SPR sensors cannot operate using s-polarized light, to which the hybrid sensor can, therefore providing new experimental possibilities.

1.2 Light Propagation through Turbid Media

As mentioned in the preceding section, light propagating through turbid media will experience attenuation. The nature of this attenuation is exponential and can be expressed by the Beer-Lambert law as:

$$I(z) = I_0 e^{-\alpha z},$$

where $\alpha = 2n_i\tilde{\omega}$ and n_i refers to the imaginary component of the refractive index of the turbid medium, while $\tilde{\omega} = \omega/c$ is the wave vector of the incident field in vacuum [6,14]. Many approaches have been used to connect the imaginary component of the medium with the distribution of the scattering particles. A common approach is to separate the interacting light into a coherent and a diffuse component [31]. The coherent component is defined as the average of all optical interactions, and can be expected to behave as a wave in a transparent medium, while the diffuse component reflects corrections to the coherent component. It has been shown that both components are affected by the concentration of particles within the matrix, depicted as a measure of the turbidity of the medium [15,31]. The diffuse component has been shown conceptually to be modelled as an incoherent superposition of coherent waves propagating in different directions [31]. The result of this is the ability to model the interaction of the medium through an effective refractive index n_{eff} .

Common effective medium approaches to determine this measure are the Maxwell-Garnett approach [46–49] and the van Hulst equation [31,50–52], respectively given by

$$\frac{\varepsilon_{eff}(\omega) - \varepsilon_m(\omega)}{\varepsilon_{eff}(\omega) + \varepsilon_m(\omega)} = f_{part} \frac{\varepsilon_{part}(\omega) - \varepsilon_m(\omega)}{\varepsilon_{part}(\omega) + \varepsilon_m(\omega)}, \text{ and}$$

$$n_{eff} = n_m (1 + i\gamma S(0)).$$

The subscripts m and $part$ denote the background matrix and suspended particles respectively, $\gamma = \frac{3}{2} \frac{f_{part}}{x^3}$ where f_{part} is the volume fraction of the particles within the matrix, and $x = k_m b$ is the size parameter of the particles. The parameter $S(0)$ is the forward scattering amplitude of an individual particle. This amplitude can be calculated analytically for simple cases, using Mie Theory [4]. Both of these models are restricted to systems with low turbidity. For systems with $f_{part} > 0.1$, the diffuse component is typically determined using radiative transfer approaches due to the increased significance of multiple scattering between particles [15,31,53–56].

For planar characterization of turbid media, such as reflectometry and SPR techniques, there is an experimental discrepancy with Fresnel theory at oblique angles [6,14,30,31,57–60]. This has led to several empirical models that have been developed for determining the refractive indices of turbid media. These empirical models use a fitting procedure. In a

recent paper by Calhoun *et. al.* [14], a modified expression for the imaginary component of the refractive index, inputted into Fresnel theory, was shown to successfully fit experimental results without additional fitting parameters. The expression accounts for the angular dependence of the imaginary component as follows,

$$n_i(\theta) = n_i(0) \left[4\pi \sqrt{\frac{(M-L)}{2}} \right], \quad (1.1)$$

where $n_i(0)$ is the value of the imaginary component at normal incidence and

$$\begin{aligned} M &= \sqrt{P^2 - 2L\sin^2(\theta) - \sin^4(\theta)}, \\ L &= \frac{(n_r^2 - n_i^2)}{n_{\text{substrate}}^2} - \sin^2(\theta), \text{ and} \\ P &= \frac{(n_r^2 + n_i^2)}{n_{\text{substrate}}^2}. \end{aligned}$$

Using the above expression, Calhoun *et. al.* was able to measure the refractive index of highly turbid media, such as cream mixtures, to a precision of 10^{-5} [6] using a least-squares fit of the reflectometry measurements. By developing an analytic model for the sensing platform in a turbid medium, it is believed additional insights can be gained into the response of the system. A theoretically strong performance of the hybrid sensor over the SPR sensor ($> 10\%$) would suggest the hybrid sensor has the potential to compete with or surpass the reflectometry measurements of [6].

1.3 Surface Plasmons and Localized Modes

It was previously mentioned that SPR sensors have been used for the precise determination of the real refractive index of a sample [35]. A surface plasmons is excited when an electromagnetic wave, in resonance with the collective electron oscillation is incident upon a metal-dielectric interface [44]. At the SPR wavelength, the Fresnel reflection coefficient across the interface of the metal and dielectric diverges. Using this, it can be shown that the SPR excitation condition is then

$$\kappa_{SP} = \tilde{\omega} \sqrt{\frac{\varepsilon \varepsilon_m}{\varepsilon + \varepsilon_m}}, \quad (1.2)$$

where κ_{SP} is the propagation constant of the field, $\tilde{\omega}$ is the magnitude of the wave vector in free space, ε is the dielectric constant of the sensing medium (commonly gold), and ε_m is the dielectric constant of the surrounding medium or analyte. The sensitivity of the resonance condition on the surrounding dielectric environment has led to the widespread use of gold SPR sensors [61–64]. As refractive index measurements are most commonly determined via a fit to experimental data, at least two independent parameters are needed. Many systems have accomplished this using measurements with s and p-polarized light (as defined in section 2.2) of the same parameter [30]. This cannot be achieved for standard SPR sensors because s-polarized light cannot excite a surface plasmon [44, 45]. Accordingly, more elaborate methods connecting the real and imaginary components can be applied to determine the complex refractive index. This is achieved through phase-retrieval techniques in the form of maximum entropy models or phase-difference curves [36–42].

A similar phenomenon to that of the propagating surface plasmon discussed above is the localized surface plasmon that occurs in noble-metal nanoparticles. Fundamentally distinct in that they do not propagate, localized surface plasmons experience resonance due to the restoring force of the curved surface on the driven oscillating electrons [44]. The modified resonance is referred to as localized surface plasmon resonance (LSPR). Several distinct features of the LSPR systems, make nanoparticles suitable for sensing platforms. These include the ability to excite the resonance by direct illumination without additional phase matching techniques, and the ability to excite the resonance by both s and p-polarized light. Metals such as gold and silver, experience resonance within the visible spectrum, and the high affinity of gold for thiol groups lends itself well to functionalization to bind a specific analyte, making it a preferred choice for optical sensors [44, 45, 65–67].

For isolated, spherical particles, it is easily shown that this resonance occurs at the divergence of the polarizability of the particles. For a particle of permittivity ε , surrounded by a medium, ε_m , this occurs when $\varepsilon = -2\varepsilon_m$, known as the Frölich condition. However, in the presence of a multilayered structure, the excitation condition must be determined in the poles of the Fresnel coefficients [43]. This will be elaborated upon in chapter 3.

1.4 Other Sensing Platforms

In addition to reflectometry and SPR sensing, additional techniques used to characterize turbid media include holography and refractometry [57, 68, 69]. Although not typically used with turbid media, waveguide-based sensors offer several advantages over other platforms that can be utilized with the hybrid structure [63, 70, 71]. The confinement of the field within the waveguide reduces losses and allows signals to be transmitted over longer distances, allowing them to be incorporated into integrated optical circuits. Furthermore, this confinement results in the production of an evanescent field, which decays exponentially as it extends into the media surrounding the waveguide. This decay results in significantly less scatter [72] and is exploited to reduce noise from non-specific binding in many waveguide sensor systems today. For the purposes of turbid media characterization, this reduction in scattering significantly reduces the complexity of the problem and justifies a sensitivity analysis in terms of a complex refractive index (neglecting extraneous scatter).

1.5 Discussion of Validity of Approximations

In this work we are referencing a hybrid biosensor platform containing a guiding multilayer structure upon which a gold nanoparticle “selvedge layer” is deposited. We want to characterize the optical response of this sensor to a changing dielectric environment above the selvedge layer. We will treat the selvedge layer as an effective medium, to a first approximation. In doing so the results presented are limited to interparticle spacings below 50 nm or ten times the radius of a single nanoparticle. We also assume that the size of the particles and the interparticle spacing in the selvedge are significantly smaller than the wavelength of incident light. Finally, we assume that any scattering of the incident field from interacting with either the turbid media or the multilayer structure below can be neglected.

The approximations in the numerical model of the selvedge are stated explicitly in section 2.3. Under these assumptions, the selvedge is treated as an effective medium to a first approximation. As the spacing between the particles is increased, the nanoparticle array begins to act as a diffraction grating with respect to an incident field [44]. In such a scheme, additional interference effects and their contributions to the waveguide mode

would need to be properly accounted for. As a result of this, the expressions and results presented are limited to interparticle spacings below 50 nm or ten times the radius of a single nanoparticle.

In addition to the limitations imposed on the lattice spacing, the size of the particles must remain significantly smaller than the wavelength of incident light. This is a result of the dipole approximation used to treat the nanoparticle array. It has been shown in numerous works [44] that spherical metallic nanoparticles can be successfully approximated as point dipoles placed at their centres. However, as the size of the particle is increased, retardation effects associated with the interaction of an incident field and the particle become significant and must be accounted for. Accordingly, particle radii are restricted to a maximum of 10 nm in this work.

The remaining approximation is the neglect of any scattering of the incident field from interacting with either the selvedge or the multilayer structure below. This is the most significant limitation of the presented work. Both of these can be justified through the use of Mie theory [4]. With respect to the particles, scattering will be limited by their small size. As shown in [73], the extinction of a propagating wave with a spherical particle is dominated by absorption over scattering at small radii. This is a result of the differing dependence of the two processes on particle size, which are respectively proportional to r^3 and r^6 [44,45,73]. Consequently, as the size of the particle is increased, additional scattering becomes significant and is something that should be addressed in future work.

The interactions with the turbid media however cannot be neglected due to particle size. Using milk as a common example, the particulates in suspension range over several micrometers [6,34]. At these sizes, scattering will dominate the extinction of the incident light. However, justification for the neglect of this scattering lies in the fact that the field interacting with the turbid media from the hybrid sensor will be evanescent in its nature. As such it will decay as it extends into the medium. For the parameters chosen in this work the imaginary component of the wave vector in the turbid medium is approximately ten times greater than that of the propagating real component. This indicates an approximate skin depth of a few hundred nanometers. As such, any field reaching the top of a particulate, or being scattered by a particulate outside the current unit cell being considered would be of

negligible intensity upon its return to the selvage layer or waveguide structure. For these reasons we neglect scattering from the turbid media and treat it as an effective medium.

1.6 Overview of Thesis

As we have discussed several aspects of current competing technologies for the sensing of turbid analytes, the remaining chapters will develop the theory used to assess the performance of the hybrid sensor. The initial theoretical formalism used to model the hybrid sensing platform will be based on [43], will be presented in chapter 2. Chapters 3 and 4 will develop two extensions to [43]. Chapter 3 will focus on the inclusion of an additional layer between the deposited nanoparticles and bare waveguide structure. This model determines the effects of a thin tethering layer, as found in experiments that require such a layer to deposit the particles onto the waveguide, such as organometallic chemical vapour deposition. Chapter 4 extends chapter 2 to include turbid media. Chapter 5 presents the numerical results of a sensor developed through the hybrid platform. In chapter 6 these results are discussed along with future work and the original contributions of the author.

Chapter 2

Formalism and Theory

Through this chapter, the reader will be introduced to the conventions and modelling techniques used to assess the performance of the hybrid plasmonic-waveguide sensor in later sections. A general schematic of the device, along with many variable definitions will be initially presented, before a discussion of the conventions and approximations used throughout this work. With the approximations defined, the method will be developed through the determination of Fresnel coefficients for the selvedge layer and a pole expansion of the multi-layer structure below it. The chapter will conclude with an overview of how the calculations will treat the polarizations of the nanoparticle array.

The motivation behind the development of the Green function formalism is to have an analytic model to study the relationship between the sensing structure and a surrounding turbid medium. The advantage to this approach is the ability to algebraically manipulate various terms to assess the contributions and gain a deeper insight into what is happening in the system. Furthermore, plotting the results of the analytic model, takes far less time than obtained results numerically [74–76].

While this thesis will focus on several significant extensions of the work done by [43], the initial formalism must be presented first. For consistency the same notations and conventions will be followed from [43]. This has resulted in much of the same background and

presentation of [43], which resulted in a modified portions being reproduced with permission¹. This begins in section 2.4.

2.1 Device Schematic

The device consists of a waveguide, formed by a guiding layer on a substrate with an above cladding layer. A plane array of gold nanoparticles is suspended above the surface of the guiding layer. The analyte to be sensed can either be dispersed within the cladding layer, as is the case for bulk sensing, or attached to the surface of the nanoparticles, as is the case for adsorption/bioconjugation based sensing. This work will focus on the former. An additional layer of finite thickness can be placed between the waveguide and nanoparticle array. The general structure of the device to be studied is shown in figure 2.1. The device is assumed to be invariant in the x-y Cartesian plane. The variables a, b , and z' , as shown in figure 2.1 will be used to respectively denote the centre-to-centre interparticle spacing, particle radius, and height of the centre of the particles above the surface ($z = 0$). The variables D_2 and D_3 refer to the thicknesses of the additional tethering layer and the wave guiding layer respectively, while the substrate layer is assumed to be infinitely thick. The subscripts of ε_j , where $j = 1, 2, 3, 4$ refer to the relative dielectric constants the cladding layer, the finite layer, the guiding wave guiding layer and the substrate respectively. The dielectric constant of the gold nanoparticles will be denoted by ε . It should also be noted that

$$\begin{aligned}\varepsilon, \varepsilon_1 &\in \mathbb{C}, \\ \varepsilon_2, \varepsilon_3, \varepsilon_4 &\in \mathbb{R},\end{aligned}$$

and

$$\varepsilon_3 > \Re(\varepsilon_1), \varepsilon_2, \varepsilon_4. \tag{2.1}$$

¹Permission obtained from the Optical Society of America to reproduce a modified version of [43]. Written permission is included in Appendix D.

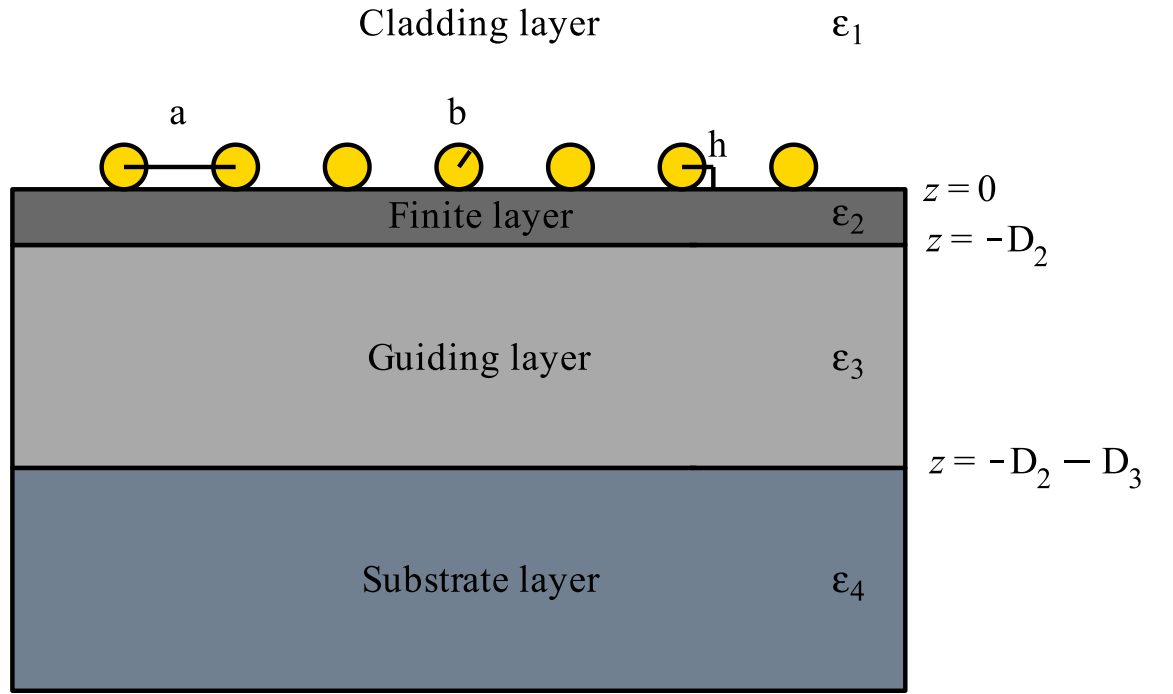


Figure 2.1: Diagram of the hybrid plasmonic waveguide sensing structure. Here $h = b$ to treat spherical particles, however the method applies to more general geometries for which this may not be true.

2.2 Conventions and Notation

Throughout this work, all fields will be assumed to exhibit harmonic time dependence such that

$$\mathbf{F}(\mathbf{r}, t) = \mathbf{F}(\mathbf{r})e^{i\omega t}.$$

Accordingly, all expressions used and derived are considered at a particular instant t and not evaluated with respect to time.

In later sections, separate expressions will be derived for s- and p-polarized waves. The polarization conventions used are made with respect to the plane containing the wave vectors of the incident, reflected and transmitted fields, henceforth referred to as the plane of incidence. This is consistent with many standard texts on the subject of electromagnetism [77, 78]. Diagrams outlining the various vectors associated with the scattering plane and the two polarizations considered are shown in figure 2.2. Fields that are s-polarized will be considered to stick out perpendicularly to the plane of incidence, while those that are p-polarized will lie within it.

To immediately characterize fields as either s- or p-polarized waves, a coordinate transformation will be made using the approach of [79]. The projection of the incident wavevector onto the xy cartesian plane will be defined by κ , while the z-component of the wave will be denoted by w_l . The subscript l is used as a placeholder, referring to medium l . It is expressed as

$$w_l = \sqrt{\tilde{\omega}^2 \varepsilon_l - \kappa^2}, \quad (2.2)$$

where

$$\begin{aligned} \tilde{\omega} &= \frac{\omega}{c} \\ &= \frac{2\pi}{\lambda}, \end{aligned} \quad (2.3)$$

is the wave vector of the incident wave in free space. The variables c and λ respectively refer to the speed of the wave and the wavelength in free space. The orientation of these vectors in Cartesian three dimensional space is shown in figure 2.3.

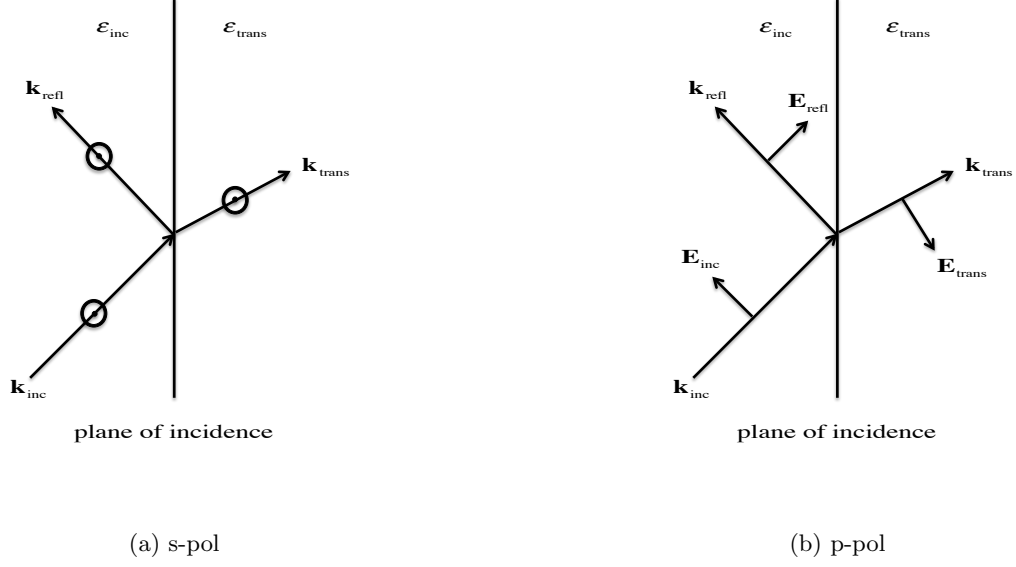


Figure 2.2: Scattering plane shown for s and p-polarized electric fields. Both cases are drawn such that the incident wavevectors of the fields begin in an initial medium characterized by ε_{inc} before impinging upon an interface, the plane of incidence and partially transmitting into a second medium $\varepsilon_{\text{trans}}$.

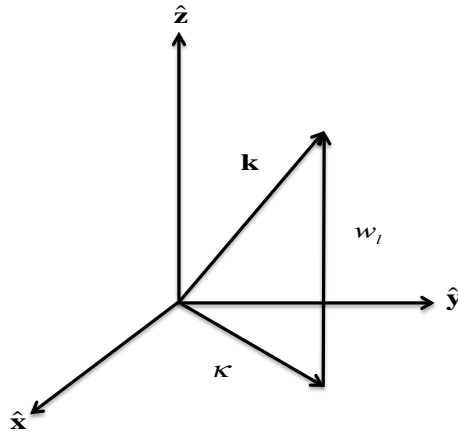


Figure 2.3: Breakdown of wavevector components in the Cartesian grid system.

With κ and w_l now defined, the unit vector for s- and p-polarized waves can be expressed as [79]

$$\hat{\mathbf{s}} \equiv \hat{\boldsymbol{\kappa}} \times \hat{\mathbf{z}}, \quad (2.4)$$

$$\hat{\mathbf{p}} \equiv \frac{\kappa \hat{\mathbf{z}} \mp w_l \hat{\boldsymbol{\kappa}}}{\tilde{\omega} n_l}, \quad (2.5)$$

where $n_l = \sqrt{\varepsilon_l}$ is the refractive index of the medium. The subscripts $+$ and $-$, respectively refer to waves travelling upwards and downwards through the system.

2.3 Assumptions

In this section three fundamental assumptions will be made. These assumptions will be the underlying foundation to the rest of this thesis. They are as follows:

1. The height of the selvedge region, d , is significantly less than the wavelength of incident light *in vacuo*,

$$d \ll \lambda. \quad (2.6)$$

2. A length scale, Δ , exists such that

$$a \ll \Delta \ll \lambda. \quad (2.7)$$

3. $\kappa^i \Delta \ll 1$, where κ^i is the component of the wavevector of the incident light along the selvedge plane.

Under these assumptions, inhomogeneities in the selvedge region can be discarded and the expressions are significantly simplified. The net result is the valid use of coarse-grained fields to treat the electric fields outside of the selvedge region. A detailed breakdown of this process is available in [43].

2.4 Method Development

The approach hinges on solving,

$$\mathbf{P}(\mathbf{R}; z) = \varepsilon_o \chi(\mathbf{R}; z) \mathbf{E}(\mathbf{R}; z), \quad (2.8)$$

$$\mathbf{E}(\mathbf{R}; z) = \mathbf{E}_h(\mathbf{R}; z) + \int \mathbf{G}(\mathbf{R} - \mathbf{R}'; z, z') \cdot \mathbf{P}(\mathbf{R}'; z) d\mathbf{R}' dz', \quad (2.9)$$

self-consistently. The Green function $\mathbf{G}(\mathbf{R} - \mathbf{R}'; z, z')$ determines the electric field from the polarization of the selvedge. This can be divided between two general contributions to the field: the field produced due to the presence of the selvedge alone, in the absence of the multilayer structure and corrections due to the multilayer structure. The former is contained within $\mathbf{G}^o(\mathbf{R} - \mathbf{R}'; z, z')$, while the latter $\mathbf{G}^R(\mathbf{R} - \mathbf{R}'; z, z')$, such that

$$\mathbf{G}(\mathbf{R} - \mathbf{R}'; z, z') = \mathbf{G}^o(\mathbf{R} - \mathbf{R}'; z, z') + \mathbf{G}^R(\mathbf{R} - \mathbf{R}'; z, z'). \quad (2.10)$$

Within each of these functions are further subdivisions,

$$\mathbf{G}^o(\mathbf{R} - \mathbf{R}'; z, z') = \mathbf{G}_L^o(\mathbf{R} - \mathbf{R}'; z, z') + \mathbf{G}_T^o(\mathbf{R} - \mathbf{R}'; z, z'), \text{ and} \quad (2.11)$$

$$\mathbf{G}^R(\mathbf{R} - \mathbf{R}'; z, z') = \mathbf{G}_I^R(\mathbf{R} - \mathbf{R}'; z, z') + \mathbf{G}_C^R(\mathbf{R} - \mathbf{R}'; z, z'); \quad (2.12)$$

where \mathbf{G}_L^o and \mathbf{G}_T^o respectively extract the longitudinal and transverse components of the field in the absence of the multilayer structure. The function \mathbf{G}_I^R is defined in the electrostatic limit $\kappa/\tilde{\omega} \rightarrow \infty$ and $\kappa D_3 \rightarrow \infty$, while $\mathbf{G}_C^R = \mathbf{G}^R - \mathbf{G}_I^R$ contains additional corrections to account for image terms in lower layers [43]. Expressions for all the Green functions mentioned above can be found in Appendix B.

As for the system considered, we will assume $\chi(\mathbf{R}, z) \neq 0$ only within the selvedge region, such that the polarization of the selvedge will affect the total electric field experienced by the system. Writing the homogeneous contribution of the total field, E_h as

$$\mathbf{E}_h(\mathbf{R}; \mathbf{z}) = \mathbf{e}^{i\kappa^i \cdot \mathbf{R}} \mathcal{F}_h(\mathbf{z}),$$

one can express the field above the selvedge layer as,

$$\mathbf{F}(\mathbf{R}; \mathbf{z}) = \mathcal{F} + \int \mathbf{G}_L^o(\mathbf{R} - \mathbf{R}'; z, z') \cdot (\mathbf{p}(\mathbf{R}'; z') + \mathbf{p}^I(\mathbf{R}'; z')) d\mathbf{R}' dz', \quad (2.13)$$

$$\mathbf{Q} \equiv 4\pi\varepsilon_o \Lambda \cdot \mathcal{F}, \text{ and} \quad (2.14)$$

$$\mathcal{F} \equiv \mathcal{F}'_{h+} + \mathcal{F}'_{h-} + \mathbf{G}_S(\kappa) \cdot \mathbf{Q}, \quad (2.15)$$

where,

$$\begin{aligned}\mathcal{F}'_{h+}(\kappa) &= \mathcal{F}_{h+} + \frac{i\tilde{\omega}^2}{2\varepsilon_o w_1} (\hat{\mathbf{s}} R_{1N}^s(\kappa) \hat{\mathbf{s}} + \hat{\mathbf{p}}_{1+} R_{1N}^s(\kappa) \hat{\mathbf{p}}_{1-}) \cdot \mathbf{Q}, \\ \mathcal{F}'_{h-}(\kappa) &= \mathcal{F}_{h-}, \\ G_S(\kappa) &= G_T^o + \frac{\kappa}{2\varepsilon_o \varepsilon_1} (\hat{\mathbf{z}} \hat{\mathbf{z}} - \hat{\kappa} \hat{\kappa}) \\ &= \frac{1}{2\varepsilon_o} \left[\frac{i\tilde{\omega}^2}{w_1} \hat{\mathbf{s}} \hat{\mathbf{s}} + \frac{i\kappa^2}{\varepsilon_1 w_1} \hat{\mathbf{z}} \hat{\mathbf{z}} + \frac{i w_1}{\varepsilon_1} \hat{\kappa} \hat{\kappa} \right].\end{aligned}$$

2.5 Determining the Selvedge Fresnel Coefficients

To determine the Fresnel coefficients across the selvedge region ($0 < z < d$) we first look at the coarse-grained electric fields just above ($z = d^+$) and below ($z = 0^-$) the selvedge layer.

$$\bar{\mathbf{E}}(\mathbf{R}; d^+) = \bar{\mathbf{E}}^+(d^+) e^{i\kappa \cdot \mathbf{R}} + \bar{\mathbf{E}}^-(d^+) e^{i\kappa \cdot \mathbf{R}}, \quad (2.16)$$

$$\bar{\mathbf{E}}(\mathbf{R}; 0^-) = \bar{\mathbf{E}}^+(0^-) e^{i\kappa \cdot \mathbf{R}} + \bar{\mathbf{E}}^-(0^-) e^{i\kappa \cdot \mathbf{R}}, \quad (2.17)$$

where,

$$\bar{\mathbf{E}}^+(d^+) = \mathcal{F}'_{h+}(\kappa) + \frac{i\tilde{\omega}^2}{2\varepsilon_o w_1} (\hat{\mathbf{s}} \hat{\mathbf{s}} + \hat{\mathbf{p}}_{1+} \hat{\mathbf{p}}_{1+}) \cdot \mathbf{Q}, \quad (2.18)$$

$$\bar{\mathbf{E}}^-(d^+) = \mathcal{F}'_{h-}(\kappa),$$

$$\bar{\mathbf{E}}^+(0^l) = \mathcal{F}'_{h+}(\kappa),$$

$$\bar{\mathbf{E}}^-(0^l) = \mathcal{F}'_{h-}(\kappa) + \frac{i\tilde{\omega}^2}{2\varepsilon_o w_1} (\hat{\mathbf{s}} \hat{\mathbf{s}} + \hat{\mathbf{p}}_{1-} \hat{\mathbf{p}}_{1-}) \cdot \mathbf{Q}.$$

Upon making the appropriate substitutions, one gets

$$\bar{\mathbf{E}}^+(d^+) = \bar{\mathbf{E}}^+(0^l) + \frac{i\tilde{\omega}^2}{2\varepsilon_o w_1} (\hat{\mathbf{s}} \hat{\mathbf{s}} + \hat{\mathbf{p}}_{1+} \hat{\mathbf{p}}_{1+}) \cdot \mathbf{Q}, \quad (2.19)$$

$$\bar{\mathbf{E}}^-(d^+) = \bar{\mathbf{E}}^-(0^l) - \frac{i\tilde{\omega}^2}{2\varepsilon_o w_1} (\hat{\mathbf{s}} \hat{\mathbf{s}} + \hat{\mathbf{p}}_{1-} \hat{\mathbf{p}}_{1-}) \cdot \mathbf{Q}.$$

Transfer matrices connecting the coarse-grained fields at the two positions can then be constructed after writing \mathbf{Q} in terms of $\bar{\mathbf{E}}^+(0^l)$ and $\bar{\mathbf{E}}^-(0^l)$, using Eqs. 2.14, and 2.16, thus

$$\mathbf{Q} = 4\pi\varepsilon_o \Lambda \cdot \left(\bar{\mathbf{E}}^+(0^l) + \bar{\mathbf{E}}^-(0^l) - \frac{i\kappa}{2\varepsilon_o \varepsilon_1} (\hat{\mathbf{z}} \hat{\kappa} + \hat{\kappa} \hat{\mathbf{z}}) \cdot \mathbf{Q} \right), \quad (2.20)$$

where

$$\Lambda = \Lambda_s \hat{s}\hat{s} + \Lambda_\kappa \hat{\kappa}\hat{\kappa} + \Lambda_z \hat{z}\hat{z}. \quad (2.21)$$

Substituting the s, κ , and z components of Eq. 2.20 into Eq. 2.19 allows one to relate the fields at $z = 0^-$ and $z = d^+$ via a transfer matrix of the form

$$\begin{bmatrix} \bar{E}^+(d^+) \\ \bar{E}^-(d^+) \end{bmatrix} = m_s \begin{bmatrix} \bar{E}^+(0^l) \\ \bar{E}^-(0^l) \end{bmatrix},$$

where the transfer matrix for the selvedge region is

$$m_s = \begin{bmatrix} 1 + n_{os} & n_{os} \\ -n_{os} & 1 - n_{os} \end{bmatrix}. \quad (2.22)$$

and

$$n_{os} \equiv \frac{2\pi i \tilde{\omega}^2}{w_1} \Lambda_s, \quad (2.23)$$

for s-polarized fields. For p-polarized fields, the contributions from both the z and κ components must be taken into consideration resulting in more complicated expressions

$$\begin{aligned} \bar{E}^+(d^+) &= \bar{E}^+(0^l) + \frac{(n_{oz} - n_{o\kappa}) \bar{E}^-(0^l) + (n_{oz} + n_{o\kappa} + 2n_{oz}n_{o\kappa}) \bar{E}^+(0^l)}{1 - n_{oz}n_{o\kappa}}, \\ \bar{E}^-(d^+) &= \bar{E}^-(0^l) - \frac{(n_{oz} + n_{o\kappa} - 2n_{oz}n_{o\kappa}) \bar{E}^-(0^l) + (n_{oz} - n_{o\kappa}) \bar{E}^+(0^l)}{1 - n_{oz}n_{o\kappa}}, \end{aligned} \quad (2.24)$$

where

$$\begin{aligned} n_{oz} &\equiv \frac{2\pi i \kappa^2}{\varepsilon_1 w_1} \Lambda_z, \\ n_{o\kappa} &\equiv \frac{2\pi i w_1}{\varepsilon_1} \Lambda_\kappa. \end{aligned} \quad (2.25)$$

Terms involving the product $n_{o\kappa}n_{oz}$ are neglected. This is due to a lack of the term w_1 in their denominator, preventing them from possibly diverging. Additionally, their quadratic dependence on the thickness of the selvedge layer which is by definition, $d \ll \lambda$, further reduces their significance.

With the cross terms dropped, expressions for p-polarized fields take on a similar form to 2.22. Defining the term

$$n_\pm \equiv n_{oz} \pm n_{o\kappa}, \quad (2.26)$$

such that

$$\begin{bmatrix} \bar{E}^+(d^+) \\ \bar{E}^-(d^+) \end{bmatrix} = m_p \begin{bmatrix} \bar{E}^+(0^l) \\ \bar{E}^-(0^l) \end{bmatrix},$$

we see that the transfer matrix is

$$m'_p = \begin{bmatrix} 1 + n_+ & n_- \\ -n_- & 1 - n_+ \end{bmatrix}. \quad (2.27)$$

From [79], we utilize the general form of the transfer matrix across a multilayer structure

$$m = \begin{bmatrix} \frac{T_{+-}T_{-+}-R_{+-}R_{-+}}{T_{+-}} & \frac{R_{+-}}{T_{+-}} \\ -\frac{R_{-+}}{T_{+-}} & \frac{1}{T_{+-}} \end{bmatrix}, \quad (2.28)$$

where T_{+-} is the transmission coefficient for light incident from above, R_{-+} is the reflection coefficient for light incident from below, etc. For s -polarized light we use Eq. 2.22 to identify

$$T_{+-} = T_{-+} = \frac{1}{1 - n_{os}} \equiv t_s, \quad (2.29)$$

and

$$R_{+-} = R_{-+} = \frac{n_{os}}{1 - n_{os}} \equiv r_s. \quad (2.30)$$

Similarly, for p -polarized light we use Eqs. 2.27 and 2.28 to identify

$$\begin{aligned} T_{+-} &= T_{-+} = \frac{1}{1 - n_+} \equiv t_p, \text{ and} \\ R_{+-} &= R_{-+} = \frac{n_-}{1 - n_+} \equiv r_p. \end{aligned}$$

With this notation, the matrices

$$m_k \equiv \begin{bmatrix} \frac{t_k^2 - r_k^2}{t_k} & \frac{r_k}{t_k} \\ -\frac{r_k}{t_k} & \frac{1}{t_k} \end{bmatrix},$$

where $k = s, p$ denote the desired polarization, can be constructed to connect the course-grained fields.

The Fresnel coefficients, across the entire structure can then be connected via

$$\begin{bmatrix} \frac{T'_{1N}T'_{N1}-R'_{1N}R'_{N1}}{T'_{1N}} & \frac{R'_{1N}}{T'_{1N}} \\ -\frac{R'_{N1}}{T'_{1N}} & \frac{1}{T'_{1N}} \end{bmatrix} = \begin{bmatrix} \frac{t_k^2 - r_k^2}{t_k} & \frac{r_k}{t_k} \\ -\frac{r_k}{t_k} & \frac{1}{t_k} \end{bmatrix} \begin{bmatrix} \frac{T_{1N}T_{N1}-R_{1N}R_{N1}}{T_{1N}} & \frac{R_{1N}}{T_{1N}} \\ -\frac{R_{N1}}{T_{1N}} & \frac{1}{T_{1N}} \end{bmatrix}, \quad (2.31)$$

from which it can be determined that

$$\begin{aligned}
 T'_{1N} &= \frac{tT_{1N}}{1 - rR_{1N}}, \\
 R'_{1N} &= r + \frac{tR_{1N}t}{1 - rR_{1N}}, \\
 R'_{N1} &= R_{N1} + \frac{T_{N1}rT_{1N}}{1 - rR_{1N}}, \\
 T'_{N1} &= \frac{T_{N1}t}{1 - rR_{1N}}.
 \end{aligned} \tag{2.32}$$

To determine how the system behaves at resonance with $\kappa = \kappa_o$, the expressions of 2.32 are expanded about their poles,

$$\begin{aligned}
 T_{1N} &\approx \frac{\tau_{1N}}{\kappa - \kappa_o}, \\
 T_{N1} &\approx \frac{\tau_{N1}}{\kappa - \kappa_o}, \\
 R_{1N} &\approx \frac{\rho_{1N}}{\kappa - \kappa_o}, \\
 R_{N1} &\approx \frac{\rho_{N1}}{\kappa - \kappa_o},
 \end{aligned} \tag{2.33}$$

where τ_{1N} , τ_{N1} , ρ_{1N} and ρ_{N1} are constants that depend on the structure. They will be looked at in greater detail in chapters 3 and 4.

Using Eq. 2.33 in the expressions for 2.32, we have

$$\begin{aligned}
 T'_{1N} &= \frac{t\tau_{1N}}{\kappa - \kappa_o - r\rho_{1N}}, \\
 R'_{1N} &= r + \frac{t\rho_{1N}t}{\kappa - \kappa_o - r\rho_{1N}}, \\
 R'_{N1} &= \frac{\rho_{N1} + r\tau_{1N}\tau_{1N}}{\kappa - \kappa_o - r\rho_{1N}}, \\
 T'_{N1} &= \frac{\tau_{N1}t}{\kappa - \kappa_o - r\rho_{1N}},
 \end{aligned} \tag{2.34}$$

The new resonance is then $\kappa = \kappa'_o$, where

$$\kappa'_o = \kappa_o + r\rho_{1N}. \tag{2.35}$$

2.6 Determining the Dipole Polarizabilities of the Nanoparticle Array

The results of the chapter up until this point apply equally well to any selvedge region that does not violate the assumptions of 2.3. In this section, however, we will determine expressions that are specific to an array of spherical nanoparticles. For instance, due to the discrete, periodic nature of the proposed selvedge, it is assumed that its susceptibility, $\chi(\mathbf{R}, z)$ takes the form

$$\chi(\mathbf{R}, z) = \sum_{\alpha} \chi^{(\alpha)}(\mathbf{R}, z),$$

where

$$\chi^{(\alpha)}(\mathbf{R}, z) = (\varepsilon - \varepsilon_1) \theta(b - |\mathbf{r} - \mathbf{r}^{(\alpha)}|),$$

and $\mathbf{r}^{(\alpha)} = \mathbf{R}^{(\alpha)} + \hat{\mathbf{z}}h$ labels the position of the α^{th} sphere and $\theta(\mathbf{r})$ is the step function.

Similarly writing

$$\mathbf{p}(\mathbf{R}, z) = \sum_{\alpha} \mathbf{p}^{(\alpha)}(\mathbf{R}, z), \quad (2.36)$$

and assuming that the particles interact and are polarized uniformly, and that they can be treated as point dipoles, one may write

$$\mathbf{p}^{(\alpha)}(\mathbf{R}, z) \simeq \frac{3\mu}{4\pi b^3} \theta(b - |\mathbf{r} - \mathbf{r}^{(\alpha)}|), \quad (2.37)$$

where μ is a dipole moment to be determined, which by *ansatz* will be the same for each α . Following from the discrete nature of the selvedge, it is assumed for points \mathbf{r}' near sites $\alpha' \neq \alpha$ that

$$\mathbf{p}^{(\alpha)}(\mathbf{R}', z') \simeq \mu \delta(\mathbf{r}' - \mathbf{r}^{(\alpha)}). \quad (2.38)$$

Using Eq. 2.37, one then finds that

$$\begin{aligned} \int \mathbf{G}_L^o(\mathbf{R} - \mathbf{R}'; z, z') \cdot \mathbf{p}^{(\alpha)}(\mathbf{R}', z') d\mathbf{R}' dz' &= -\frac{\mu}{4\pi\epsilon_0\varepsilon_1 b^3} \\ \text{for } |\mathbf{r} - \mathbf{r}^{(\alpha)}| &< b, \end{aligned}$$

while using (2.38) for the other sites when we are at such \mathbf{r} , results in

$$\int G_L^o(\mathbf{R} - \mathbf{R}'; z, z') \cdot \mathbf{p}^{(\alpha')}(\mathbf{R}', z') d\mathbf{R}' dz' = G_L^o(\mathbf{R} - \mathbf{R}^{(\alpha')}; z, h) \cdot \mu,$$

$$\text{for } |\mathbf{r} - \mathbf{r}^{(\alpha)}| < b \text{ and } \alpha' \neq \alpha.$$

Thus using Eq. 2.36, we have

$$\int G_L^o(\mathbf{R} - \mathbf{R}'; z, z') \cdot \mathbf{p}(\mathbf{R}', z') d\mathbf{R}' dz' = -\frac{\mu}{4\pi\epsilon_0\epsilon_1 b^3} + \sum_{\alpha' \neq \alpha} G_L^o(\mathbf{R} - \mathbf{R}^{(\alpha')}; z, h) \cdot \mu, \quad (2.39)$$

$$\text{for } |\mathbf{r} - \mathbf{r}^{(\alpha)}| < b.$$

This is the second term needed on the right-hand side of Eq. 2.13. The remaining term involves the image polarization, defined by

$$\mathbf{p}^I(\mathbf{R}, z) = \mathbf{M} \cdot \mathbf{p}(\mathbf{R}, -z),$$

where, the dyadic

$$\mathbf{M} \equiv \frac{\epsilon_2 - \epsilon_1}{\epsilon_2 + \epsilon_1} (\hat{\mathbf{z}}\hat{\mathbf{z}} - \hat{\mathbf{x}}\hat{\mathbf{x}} - \hat{\mathbf{y}}\hat{\mathbf{y}}). \quad (2.40)$$

It should be noted that the expression shown above is simply being used as a placeholder so that the remaining portions of the method may be developed. The presence of an additional finite layer between the selvedge and the lower structure, will directly affect the image polarization as will be seen in chapter 3.

Since the field at the location of the image dipoles is not needed, a first approximation is to use (2.38) and find that

$$\mathbf{p}^I(\mathbf{R}, z) = \mathbf{M} \cdot \sum_{\alpha'} \mu \delta(\mathbf{R} - \mathbf{R}^{(\alpha')}) \delta(z + h). \quad (2.41)$$

Using this in Eq. 2.13, together with Eq. 2.39, yields

$$\mathbf{F}(\mathbf{R}; z) = \mathcal{F} - \frac{\mu}{4\pi\epsilon_0\epsilon_1 b^3} + \sum_{\alpha' \neq \alpha} G_L^o(\mathbf{R} - \mathbf{R}^{(\alpha')}; z, h) \cdot \mu \quad (2.42)$$

$$+ \sum_{\alpha'} G_L^o(\mathbf{R} - \mathbf{R}^{(\alpha')}; z, -h) \cdot \mathbf{M} \cdot \mu,$$

$$\text{for } |\mathbf{r} - \mathbf{r}^{(\alpha)}| < b.$$

This expression can be used in determining $\mathbf{p}^{(\alpha)}(\mathbf{R}, z)$, since for $|\mathbf{r} - \mathbf{r}^{(\alpha)}| < b$ we have,

$$\mathbf{p}^{(\alpha)}(\mathbf{R}, z) = \epsilon_0 \chi^{(\alpha)}(\mathbf{R}, z) \mathbf{F}(\mathbf{R}; z).$$

For such points we make the point dipole approximation by putting $\mathbf{F}(\mathbf{R}; z) \simeq \mathbf{F}(\mathbf{R}^{(\alpha)}; h)$. Integrating over the sphere we find (see Eq. 2.37)

$$\begin{aligned} \frac{\mu}{\frac{4\pi}{3} b^3 \epsilon_0 (\epsilon - \epsilon_1)} &= \mathcal{F} - \frac{\mu}{4\pi \epsilon_0 \epsilon_1 b^3} + \sum_{\alpha' \neq \alpha} G_L^o(\mathbf{R}^{(\alpha)} - \mathbf{R}^{(\alpha')}; h, h) \cdot \mu \\ &+ \sum_{\alpha'} G_L^o(\mathbf{R}^{(\alpha)} - \mathbf{R}^{(\alpha')}; h, -h) \cdot \mathbf{M} \cdot \mu. \end{aligned} \quad (2.43)$$

Bringing the second term on the right-hand side of Eq. 2.43 over to the left-hand side and rewriting the result, we have

$$\begin{aligned} \frac{\mu}{\frac{4\pi}{3} b^3 \epsilon_0 \left(\frac{3\epsilon_1(\epsilon - \epsilon_1)}{\epsilon + 2\epsilon_1} \right)} &= \mathcal{F} + \sum_{\alpha' \neq \alpha} G_L^o(\mathbf{R}^{(\alpha)} - \mathbf{R}^{(\alpha')}; h, h) \cdot \mu \\ &+ \sum_{\alpha'} G_L^o(\mathbf{R}^{(\alpha)} - \mathbf{R}^{(\alpha')}; h, -h) \cdot \mathbf{M} \cdot \mu. \end{aligned} \quad (2.44)$$

The result is displayed in terms of the polarizability of a sphere of relative permittivity ϵ embedded in a background medium of relative permittivity ϵ_1 . Defining a dimensionless tensor \mathbf{S} according to

$$\begin{aligned} \mathbf{S} &\equiv 4\pi \epsilon_0 \mathcal{A}^{3/2} \sum_{\alpha' \neq \alpha} G_L^o(\mathbf{R}^{(\alpha)} - \mathbf{R}^{(\alpha')}; h, h) \\ &+ 4\pi \epsilon_0 \mathcal{A}^{3/2} \sum_{\alpha'} G_L^o(\mathbf{R}^{(\alpha)} - \mathbf{R}^{(\alpha')}; h, -h) \cdot \mathbf{M}, \end{aligned} \quad (2.45)$$

we can write Eq. 2.44 as

$$\mathbf{Q} = \left[\frac{\epsilon_1(\epsilon - \epsilon_1)}{\epsilon + 2\epsilon_1} \frac{b^3}{\mathcal{A}} \right] \left[4\pi \epsilon_0 \mathcal{F} + \frac{1}{\mathcal{A}^{1/2}} \mathbf{S} \cdot \mathbf{Q} \right]. \quad (2.46)$$

After some algebra one can isolate Λ , such that

$$\Lambda \equiv \left[\frac{\epsilon_1(\epsilon - \epsilon_1)}{\epsilon + 2\epsilon_1} \frac{b^3}{\mathcal{A}} \right] \left(\mathbf{U} - \frac{\epsilon_1(\epsilon - \epsilon_1)}{\epsilon + 2\epsilon_1} \frac{b^3}{\mathcal{A}^{3/2}} \mathbf{S} \right)^{-1}, \quad (2.47)$$

which is independent of κ . The response of the selvedge along each coordinate axes n_{os} , $n_{o\kappa}$, and n_{oz} then follow immediately from Eqs. 2.23, and 2.25. With this development, we can proceed with the first extension of [43] in the next chapter.

Chapter 3

Effects of the Finite Layer

Here the extension of the model used in [43] will begin with the inclusion of a finite dielectric layer between the guiding multilayer structure and the selvedge. The inclusion of a finite layer to tether the nanoparticles to the waveguide allows us to assess the performance of sensors produced using deposition techniques requiring such a layer [80–82] in comparison to those that do not, such as electroless deposition. If deposition techniques requiring a tethering layer are comparable in performance, it could make the industrial production of the hybrid sensor more attractive [83–85].

The layer, of thickness D_2 and dielectric constant ε_2 , is placed between the waveguide layer and cladding layer of the structure. It is shown in figure 2.1. To accomplish this, we will begin by determining the changes to the Green function G_I^R , responsible for the electrostatic corrections to the selvedge, due to the presence of the multilayer structure. This will be done using the formalism of [43] in 3.1 and confirmed through the use of the method of images technique in 3.2. With the new form of G_I^R known, the response of the selvedge will be determined in 3.3.

In addition to the effects of the finite layer on the response of the selvedge, the changes to the reflection across the multilayer structure must also be taken into account. This will lead to new expressions for the solution condition of the waveguide modes, as shown in

3.4, as well as the expansion parameter in 3.5. To confirm the newly derived expression, limiting cases will be examined in 3.6. Once it has been confirmed that the expressions of this chapter agree with the original work of [43], the effects of the finite layer on the absorption, and changes to the waveguide mode will be examined and discussed at the end of the chapter.

3.1 Image Electric Field via Green Function Approach

To begin, we will determine the electric field due to image dipoles of the selvedge in the multilayer structure. This is determined via

$$\mathbf{E}_I(\mathbf{R}, z) = \frac{1}{(2\pi)^2} \int e^{i\boldsymbol{\kappa} \cdot \mathbf{R}} \mathbf{G}_I^R(\boldsymbol{\kappa}; z, z') \cdot \boldsymbol{\mu} d\boldsymbol{\kappa}, \quad (3.1)$$

where

$$\boldsymbol{\kappa} \cdot \mathbf{R} = \kappa R \cos \phi,$$

$$d\boldsymbol{\kappa} = d\kappa_x d\kappa_y = \kappa d\kappa d\phi,$$

and

$$\boldsymbol{\mu} = \mu_x \hat{x} + \mu_y \hat{y} + \mu_z \hat{z}.$$

The relationship between the vectors $\boldsymbol{\kappa}$ and \mathbf{R} in the x-y Cartesian plane is shown in figure 3.1. Using Eq. B.8 in Eq. 3.1, the expression for the electric field of the image dipoles becomes

$$\mathbf{E}_I(\mathbf{R}, z) = \frac{1}{8\pi^2 \varepsilon_0 \varepsilon_1} \int e^{i\kappa R \cos \phi} \kappa^2 R_{13} (\hat{z}\hat{z} + \hat{\kappa}\hat{\kappa} + i\hat{z}\hat{\kappa} - i\hat{\kappa}\hat{z}) e^{-\kappa(z+z')} \cdot \boldsymbol{\mu} d\kappa d\phi, \quad (3.2)$$

where $R_{13} = r_{12} + \frac{t_{12}r_{23}t_{21}d^{-2\kappa D_2}}{1-r_{23}r_{21}e^{-2\kappa D_2}}$ is the reflection coefficient across the first three layers of the system, as given in [43]. To facilitate a comparison with the method of images, and the eventual implementation of Eq. 2.41, we will re-express the variables in Cartesian

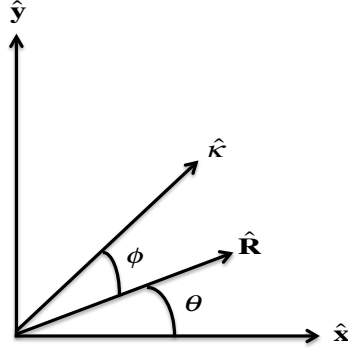


Figure 3.1: Orientation of κ and R in the xy plane.

coordinates. This is done according to angular relations depicted in figure 3.1, which shows

$$\begin{aligned}
 \hat{\kappa} &= \hat{x} \cos(\phi + \theta) + \hat{y} \sin(\phi + \theta), \\
 \hat{\kappa}\hat{\kappa} &= \hat{x}\hat{x} \cos^2(\phi + \theta) + \hat{y}\hat{y} \sin^2(\phi + \theta) + (\hat{x}\hat{y} + \hat{y}\hat{x}) \cos(\phi + \theta) \sin(\phi + \theta), \\
 \hat{z}\hat{\kappa} &= \hat{z}\hat{x} \cos(\phi + \theta) + \hat{z}\hat{y} \sin(\phi + \theta), \\
 \hat{\kappa}\hat{z} &= \hat{x}\hat{z} \cos(\phi + \theta) + \hat{y}\hat{z} \sin(\phi + \theta),
 \end{aligned} \tag{3.3}$$

For brevity in some later expressions we will define a dyadic \mathbf{O} for the terms of Eq. 3.2 to treat the unit vectors. This is defined as,

$$\begin{aligned}
 \mathbf{O} &\equiv \hat{z}\hat{z} + \hat{\kappa}\hat{\kappa} + i\hat{z}\hat{\kappa} - i\hat{\kappa}\hat{z} \\
 &= \hat{z}\hat{z} + \hat{x}\hat{x} \cos^2(\phi + \theta) + \hat{y}\hat{y} \sin^2(\phi + \theta) + (\hat{x}\hat{y} + \hat{y}\hat{x}) \cos(\phi + \theta) \sin(\phi + \theta) \\
 &\quad + i(\hat{z}\hat{x} \cos(\phi + \theta) + \hat{z}\hat{y} \sin(\phi + \theta)) - i(\hat{x}\hat{z} \cos(\phi + \theta) + \hat{y}\hat{z} \sin(\phi + \theta)).
 \end{aligned} \tag{3.4}$$

Then it remains valid to integrate the angular dependence solely over ϕ and,

$$\mathbf{E}_I(\mathbf{R}, z) = \frac{1}{8\pi^2 \varepsilon_0 \varepsilon_1} \int_0^\infty \kappa^2 R_{13} e^{-\kappa(z+z')} \int_0^{2\pi} e^{i\kappa R \cos \phi} \mathbf{O} \cdot \boldsymbol{\mu} d\phi d\kappa. \tag{3.5}$$

The various integrals of Eq. 3.5 are evaluated in detail in Appendix A. Substituting

Eqs. A.4 - A.9, the angular dependence of Eq. 3.5 becomes

$$\begin{aligned} \int_0^{2\pi} e^{i\kappa R \cos \phi} O \cdot \boldsymbol{\mu} d\phi &= \pi (\mu_x \hat{x} + \mu_y \hat{y} + 2\mu_z \hat{z}) J_0(\kappa R) \\ &+ \frac{2\pi}{\sqrt{x^2 + y^2}} (\mu_z x \hat{x} + \mu_z y \hat{y} - [\mu_x x + \mu_y y] \hat{z}) J_1(\kappa R) \\ &+ \frac{\pi}{x^2 + y^2} (-[\mu_x(x^2 - y^2) + 2\mu_y xy] \hat{x} + [\mu_y(x^2 - y^2) - 2\mu_x xy] \hat{y}) J_2(\kappa R). \end{aligned}$$

The electric field is then given by

$$\begin{aligned} \mathbf{E}_I(\mathbf{R}, z) &= \frac{1}{8\pi^2 \varepsilon_0 \varepsilon_1} \int_0^\infty d\kappa \kappa^2 R_{13} e^{-\kappa(z+z')} [\pi (\mu_x \hat{x} + \mu_y \hat{y} + 2\mu_z \hat{z}) J_0(\kappa R) \\ &+ \frac{2\pi}{\sqrt{x^2 + y^2}} (\mu_z x \hat{x} + \mu_z y \hat{y} - [\mu_x x + \mu_y y] \hat{z}) J_1(\kappa R) \\ &+ \frac{\pi}{x^2 + y^2} (-[\mu_x(x^2 - y^2) + 2\mu_y xy] \hat{x} + [\mu_y(x^2 - y^2) - 2\mu_x xy] \hat{y}) J_2(\kappa R)] , \\ &= \frac{1}{8\pi \varepsilon_0 \varepsilon_1} \int_0^\infty d\kappa \kappa^2 \left(r_{12} + \frac{t_{12} r_{23} t_{21} e^{-2\kappa D_2}}{1 - r_{23} r_{21} e^{-2\kappa D_2}} \right) e^{-\kappa(z+z')} [(\mu_x \hat{x} + \mu_y \hat{y} + 2\mu_z \hat{z}) J_0(\kappa R) \\ &+ \frac{2}{\sqrt{x^2 + y^2}} (\mu_z x \hat{x} + \mu_z y \hat{y} - [\mu_x x + \mu_y y] \hat{z}) J_1(\kappa R) \\ &+ \frac{1}{x^2 + y^2} (-[\mu_x(x^2 - y^2) + 2\mu_y xy] \hat{x} + [\mu_y(x^2 - y^2) - 2\mu_x xy] \hat{y}) J_2(\kappa R)] . \end{aligned} \quad (3.6)$$

Before proceeding we must simplify R_{13} to facilitate the integration. As $r_{23} r_{21} e^{-2\kappa D_2} < 1$ for $\kappa \geq 0$, we may use the power series expansion

$$\frac{1}{1 - r_{23} r_{21} e^{-2\kappa D_2}} = \sum_{n=0}^{\infty} (r_{23} r_{21} e^{-2\kappa D_2})^n , \quad (3.7)$$

and write

$$R_{13} = \sum_{n=0}^{\infty} (r_{23} r_{21})^n \left(r_{12} e^{-2\kappa n D_2} + r_{23} e^{-2\kappa(n+1) D_2} \right) . \quad (3.8)$$

The expression for the electric field is then reduced to

$$\begin{aligned} \mathbf{E}_I(\mathbf{R}, z) &= \frac{1}{8\pi \varepsilon_0 \varepsilon_1} \int_0^\infty d\kappa \kappa^2 \sum_{n=0}^{\infty} (r_{23} r_{21})^n \left(r_{12} e^{-\kappa(z+z'+2nD_2)} + r_{23} e^{-\kappa(z+z'+2(n+1)D_2)} \right) \times \\ & \quad [(\mu_x \hat{x} + \mu_y \hat{y} + 2\mu_z \hat{z}) J_0(\kappa R) \\ & \quad + \frac{2}{\sqrt{x^2 + y^2}} (\mu_z x \hat{x} + \mu_z y \hat{y} - [\mu_x x + \mu_y y] \hat{z}) J_1(\kappa R) \\ & \quad + \frac{1}{x^2 + y^2} (-[\mu_x(x^2 - y^2) + 2\mu_y xy] \hat{x} + [\mu_y(x^2 - y^2) - 2\mu_x xy] \hat{y}) J_2(\kappa R)] . \end{aligned} \quad (3.9)$$

Making the appropriate substitutions using Eqs. A.11 - A.16 in Eq. 3.9, we obtain the electric field due to image dipoles in the layers below the seldge,

$$\begin{aligned}
 \mathbf{E}_I(\mathbf{R}, z, z') = & \frac{1}{4\pi\epsilon_0\epsilon_1} \sum_{n=0}^{\infty} (r_{12}r_{32})^n \times \\
 & \left\{ (\mu_x\hat{x} + \mu_y\hat{y} + 2\mu_z\hat{z}) \left(\frac{r_{12}(z+z'+2nD_2)^2}{[R^2 + (z+z'+2nD_2)^2]^{5/2}} + \frac{r_{23}(z+z'+2(n+1)D_2)^2}{[R^2 + (z+z'+2(n+1)D_2)^2]^{5/2}} \right) \right. \\
 & + 3(\mu_zx\hat{x} + \mu_zy\hat{y} - [\mu_xx + \mu_yy]\hat{z}) \\
 & \times \left(\frac{r_{12}(z+z'+2nD_2)}{[R^2 + (z+z'+2nD_2)^2]^{5/2}} + \frac{r_{23}(z+z'+2(n+1)D_2)}{[R^2 + (z+z'+2(n+1)D_2)^2]^{5/2}} \right) \\
 & - [(\mu_x(2x^2 - y^2) + 3\mu_yxy)\hat{x} - (\mu_y(x^2 - 2y^2) - 3\mu_xxy)\hat{y} + \mu_zR^2\hat{z}] \\
 & \left. \times \left(\frac{r_{12}}{[R^2 + (z+z'+2nD_2)^2]^{5/2}} + \frac{r_{23}}{[R^2 + (z+z'+2(n+1)D_2)^2]^{5/2}} \right) \right\}.
 \end{aligned}
 \tag{3.10}$$

3.2 Verification of Image Dipole Contributions Through The Method of Images

To verify that the results of Eq. 3.10 are correct, this section will attempt to replicate the same result through the method of images. The technique serves as a standard approach in any system where symmetry can be exploited. It is executed by replacing the physical system, containing a dipole above two distinct interfaces, with an equivalent one in which the interfaces are replaced with images of the original dipole to mimic the electrostatic potential at each interface. The total potential at a specified point can then be found through a superposition of the contributions of each image term [77]. In our system, the dipole will be located at some arbitrary position, $\mathbf{r}' = (0, 0, z')$ in the region $z' > 0$. The solution for a single charge can be found through a Fourier-Bessel expansion of the system in cylindrical coordinates as is done in [86].

The results from [86] determine the potential for a single charge to be

$$V = \frac{q}{4\pi\epsilon_o\epsilon_1} f,
 \tag{3.11}$$

where

$$f = \frac{1}{(R^2 + z^2)^{1/2}} + \sum_{n=0}^{\infty} (r_{12}r_{32})^n \left(\frac{-r_{12}}{[R^2 + (z + z' + 2nD_2)^2]^{1/2}} + \frac{r_{32}}{[R^2 + (z + z' + 2(n+1)D_2)^2]^{1/2}} \right).$$

To apply this result to our system, a generalization of the single charge to a point dipole source is required. This can be accomplished through an expansion of Eq. 3.11 in the double limit $q \rightarrow \infty$ and $d \rightarrow 0$. The result is

$$\begin{aligned} V &= \frac{q}{4\pi\epsilon_o\epsilon_1} \left[f\left(\left|\mathbf{r} - \mathbf{r}' - \frac{\mathbf{d}}{2}\right|\right) - f\left(\left|\mathbf{r} - \mathbf{r}' + \frac{\mathbf{d}}{2}\right|\right) \right], \\ &= \frac{q}{4\pi\epsilon_o\epsilon_1} \left[f(|\mathbf{r} - \mathbf{r}'|) - \frac{\mathbf{d}}{2} \cdot \nabla f(|\mathbf{r} - \mathbf{r}'|) + \dots \right] - \frac{q}{4\pi\epsilon_1} \left[f(|\mathbf{r} - \mathbf{r}'|) + \frac{\mathbf{d}}{2} \cdot \nabla f(|\mathbf{r} - \mathbf{r}'|) + \dots \right], \\ &= \frac{-1}{4\pi\epsilon_o\epsilon_1} [q\mathbf{d} \cdot \nabla f(|\mathbf{r} - \mathbf{r}'|)], \\ &= \frac{-1}{4\pi\epsilon_o\epsilon_1} [\mu \cdot \nabla f(|\mathbf{r} - \mathbf{r}'|)], \\ &= \frac{-1}{4\pi\epsilon_o\epsilon_1} \cdot \left[-\frac{\mu_x x + \mu_y y + \mu_z z}{(x^2 + y^2 + z^2)^{3/2}} + (\mu_x x + \mu_y y) \right. \\ &\quad \times \sum_{n=0}^{\infty} (r_{12}r_{32})^n \left(\frac{r_{12}}{[x^2 + y^2 + (z + z' + 2nD_2)^2]^{3/2}} - \frac{r_{32}}{[x^2 + y^2 + (z + z' - 2(n+1)D_2)^2]^{3/2}} \right) \\ &\quad \left. - \mu_z \sum_{n=0}^{\infty} (r_{12}r_{32})^n \left(\frac{r_{12}(z + z' + 2nD_2)}{[x^2 + y^2 + (z + z' + 2nD_2)^2]^{3/2}} - \frac{r_{32}(z + z' + 2(n+1)D_2)}{[x^2 + y^2 + (z + z' + 2(n+1)D_2)^2]^{3/2}} \right) \right]. \end{aligned} \tag{3.12}$$

The electric field can then be determined as the negative gradient of Eq. 3.12.

$$\begin{aligned}
 \mathbf{E} &= -\nabla V, \\
 &= \frac{1}{4\pi\epsilon_o\epsilon_1} \cdot \left[\frac{3(\mu_x x + \mu_y y + \mu_z z)(x\hat{x} + y\hat{y} + z\hat{z})}{(x^2 + y^2 + z^2)^{5/2}} - \frac{\mu_x \hat{x} + \mu_y \hat{y} + \mu_z \hat{z}}{(x^2 + y^2 + z^2)^{3/2}} + \right. \\
 &\quad \sum_{n=0}^{\infty} (r_{12}r_{32})^n \times \\
 &\quad \left\{ (\mu_x \hat{x} + \mu_y \hat{y} + 2\mu_z \hat{z}) \left(\frac{r_{12}(z + z' + 2nD_2)^2}{[R^2 + (z + z' + 2nD_2)^2]^{5/2}} + \frac{r_{23}(z + z' + 2(n+1)D_2)^2}{[R^2 + (z + z' + 2(n+1)D_2)^2]^{5/2}} \right) \right. \\
 &\quad + 3(\mu_z x \hat{x} + \mu_z y \hat{y} - [\mu_x x + \mu_y y] \hat{z}) \\
 &\quad \times \left(\frac{r_{12}(z + z' + 2nD_2)}{[R^2 + (z + z' + 2nD_2)^2]^{5/2}} + \frac{r_{23}(z + z' + 2(n+1)D_2)}{[R^2 + (z + z' + 2(n+1)D_2)^2]^{5/2}} \right) \\
 &\quad - ([\mu_x (2x^2 - y^2) + 3\mu_y xy] \hat{x} - [\mu_y (x^2 - 2y^2) - 3\mu_x xy] \hat{y} + \mu_z R^2 \hat{z}) \\
 &\quad \left. \times \left(\frac{r_{12}}{[R^2 + (z + z' + 2nD_2)^2]^{5/2}} + \frac{r_{23}}{[R^2 + (z + z' + 2(n+1)D_2)^2]^{5/2}} \right) \right\}.
 \end{aligned} \tag{3.13}$$

From an inspection of Eq. 3.13, one will recognize the first two terms as the static field of an electric dipole in the absence of any interfaces. As these terms will be accounted for by G_L^o of chapter 2, they are not expected to appear in Eq. 3.10 and will be neglected in this treatment. Rewriting Eq. 3.13 as

$$\mathbf{E} = \mathbf{E}_o + \mathbf{E}_I, \tag{3.14}$$

where

$$\begin{aligned}
 \mathbf{E}_I(\mathbf{R}, z, z') &= \frac{1}{4\pi\epsilon_0\epsilon_1} \sum_{n=0}^{\infty} (r_{12}r_{32})^n \times \\
 &\left\{ (\mu_x\hat{x} + \mu_y\hat{y} + 2\mu_z\hat{z}) \left(\frac{r_{12}(z + z' + 2nD_2)^2}{[R^2 + (z + z' + 2nD_2)^2]^{5/2}} + \frac{r_{23}(z + z' + 2(n+1)D_2)^2}{[R^2 + (z + z' + 2(n+1)D_2)^2]^{5/2}} \right) \right. \\
 &+ 3(\mu_zx\hat{x} + \mu_zy\hat{y} - [\mu_xx + \mu_yy]\hat{z}) \left(\frac{r_{12}(z + z' + 2nD_2)}{[R^2 + (z + z' + 2nD_2)^2]^{5/2}} + \frac{r_{23}(z + z' + 2(n+1)D_2)}{[R^2 + (z + z' + 2(n+1)D_2)^2]^{5/2}} \right) \\
 &- ([\mu_x(2x^2 - y^2) + 3\mu_yxy]\hat{x} - [\mu_y(x^2 - 2y^2) - 3\mu_xxy]\hat{y} + \mu_zR^2\hat{z}) \times \\
 &\quad \left. \left(\frac{r_{12}}{[R^2 + (z + z' + 2nD_2)^2]^{5/2}} + \frac{r_{23}}{[R^2 + (z + z' + 2(n+1)D_2)^2]^{5/2}} \right) \right\}.
 \end{aligned} \tag{3.15}$$

As Eq. 3.10 and Eq. 3.15 agree, we will proceed with the Green function method in the next section.

3.3 Response of the Selvedge to the Additional Image Terms

From Eq. 3.10, one can see that for a point dipole at $z' = h$, the electric field can be written as

$$\mathbf{E}_I(\mathbf{R}, z, h) = \int G_I^R(\mathbf{R} - \mathbf{R}', z, z') \cdot \mathbf{P}(\mathbf{R}', z') dR' dz', \tag{3.16}$$

where

$$\mathbf{P}(\mathbf{R}', \mathbf{z}') = \mu \delta(R') \delta(z' - h), \text{ and} \quad (3.17)$$

$$\begin{aligned} G_I^R(\mathbf{R}, z, z') &= \frac{1}{4\pi\epsilon_0\epsilon_1} \sum_{n=0}^{\infty} (r_{12}r_{32})^n \times \\ &\left\{ (\hat{x}\hat{x} + \hat{y}\hat{y} + 2\hat{z}\hat{z}) \left(\frac{r_{12}(z + z' + 2nD_2)^2}{[R^2 + (z + z' + 2nD_2)^2]^{5/2}} + \frac{r_{23}(z + z' + 2(n+1)D_2)^2}{[R^2 + (z + z' + 2(n+1)D_2)^2]^{5/2}} \right) \right. \\ &+ 3[(\hat{x}\hat{z} - \hat{z}\hat{x})x + (\hat{y}\hat{z} - \hat{z}\hat{y})y] \\ &\times \left(\frac{r_{12}(z + z' + 2nD_2)}{[R^2 + (z + z' + 2nD_2)^2]^{5/2}} + \frac{r_{23}(z + z' + 2(n+1)D_2)}{[R^2 + (z + z' + 2(n+1)D_2)^2]^{5/2}} \right) \\ &- [(2x^2 - y^2)\hat{x}\hat{x} - (x^2 - 2y^2)\hat{y}\hat{y} + 3(\hat{x}\hat{y} - \hat{y}\hat{x})xy + \mu_z R^2 \hat{z}] \times \\ &\left. \left(\frac{r_{12}}{[R^2 + (z + z' + 2nD_2)^2]^{5/2}} + \frac{r_{23}}{[R^2 + (z + z' + 2(n+1)D_2)^2]^{5/2}} \right) \right\}. \end{aligned} \quad (3.18)$$

To further simplify the remaining mathematics we note that through the use of Eq. B.5, G_I^R can be expressed in terms of G_L^o as

$$G_I^R(\mathbf{R}, z, z') = \sum_{n=0}^{\infty} (r_{21}r_{23})^n \{ G_L^o(\mathbf{R}, z, -z'_1(n)) \cdot M_1 + G_L^o(\mathbf{R}, z, -z'_2(n)) \cdot M_2 \}, \quad (3.19)$$

where

$$M_1 = r_{12}(-\hat{x}\hat{x} - \hat{y}\hat{y} + \hat{z}\hat{z}), \quad M_2 = r_{23}(-\hat{x}\hat{x} - \hat{y}\hat{y} + \hat{z}\hat{z}), \quad (3.20)$$

$$z'_1(n) = z' + 2nD_2, \quad z'_2(n) = z' + 2(n+1)D_2. \quad (3.21)$$

With Eq. 3.19 it is now possible to use 2.45 and determine how the measurement sensitivity of the system will change due to the presence and thickness of the finite layer. Recall that

$$\begin{aligned} S &= 4\pi\epsilon_0 \mathcal{A}^{3/2} \sum_{\alpha' \neq 0} G_L^o(-\mathbf{R}^{(\alpha')}, h, h) \\ &+ 4\pi\epsilon_0 \mathcal{A}^{3/2} \sum_{\alpha'} G_L^o(-\mathbf{R}^{(\alpha')}, h, -h) \cdot M. \end{aligned}$$

As we are treating a square lattice of nanoparticles, we replace $\mathbf{R}^{(\alpha')}$ in the summation by $a\sqrt{m^2 + n^2}$. The factors m and n are integers denoting the position of the α' th particle.

Using Eq. B.5, we find the first term of Eq. 2.45 to be

$$\begin{aligned}
 4\pi\epsilon_0\mathcal{A}^{3/2}\sum_{\alpha'\neq 0}G_L^o(-\mathbf{R}^{(\alpha')},h,h) &= \frac{1}{a^3\epsilon_1}\sum_{m,n}'\frac{1}{(m^2+n^2)^{5/2}} \\
 &\quad \times [(2m^2-n^2)\hat{x}\hat{x} + (2n^2-m^2)\hat{y}\hat{y} - (m^2+n^2)\hat{z}\hat{z}], \\
 &= \frac{\mathcal{A}^{3/2}}{a^3\epsilon_1}\sum_{m,n}'\frac{1}{(m^2+n^2)^{3/2}}\left(\frac{1}{2}\hat{x}\hat{x} + \frac{1}{2}\hat{y}\hat{y} - \hat{z}\hat{z}\right) \\
 &\quad + \sum_{m,n}'\frac{3}{2a^3\epsilon_1}\frac{(m^2-n^2)(\hat{x}\hat{x} - \hat{y}\hat{y})}{(m^2+n^2)^{5/2}}, \\
 &= \frac{1}{\epsilon_1}\sum_{m,n}'\frac{1}{(m^2+n^2)^{3/2}}\left(\frac{1}{2}\hat{x}\hat{x} + \frac{1}{2}\hat{y}\hat{y} - \hat{z}\hat{z}\right), \\
 &= \frac{1}{\epsilon_1}A\left(\frac{1}{2}\hat{x}\hat{x} + \frac{1}{2}\hat{y}\hat{y} - \hat{z}\hat{z}\right). \tag{3.22}
 \end{aligned}$$

In going to Eq. 3.23, we note that the second summation in Eq. 3.22 converges to zero due to the symmetry in the m and n indices, and

$$A \equiv \sum_{m,n}'\frac{1}{(m^2+n^2)^{3/2}} = 9.03362\dots \tag{3.24}$$

To properly treat the finite layer system, the second term in Eq. 2.45 must be modified such that

$$G_L^o(-\mathbf{R}^{(\alpha')},h,-h)\cdot M \rightarrow \sum_{k=0}^{\infty}(r_{21}r_{23})^k\{G_L^o(\mathbf{R},h,-h'(k))\cdot M_1 + G_L^o(\mathbf{R},h,-h'(k+1))\cdot M_2\}. \tag{3.25}$$

Denoting $h(k)$ as h_k we determine the summations to be

$$\begin{aligned}
 & 4\pi\epsilon_0 \sum_{\alpha'} \sum_{k=0}^{\infty} (r_{21}r_{23})^k \{G_L^o(\mathbf{R}, h, -h'_k) \cdot M_1 + G_L^o(\mathbf{R}, h, -h'_{k+1}) \cdot M_2\} \\
 &= \frac{1}{a^3\epsilon_1} \sum_{k=0}^{\infty} (r_{21}r_{23})^k \times \\
 & \sum_{m,n} \left\{ \frac{r_{12}}{(m^2 + n^2 + \bar{h}_k^2)^{5/2}} [(\bar{h}_k^2 - 2m^2 + n^2)\hat{x}\hat{x} + (\bar{h}_k^2 + m^2 - 2n^2)\hat{y}\hat{y} + (2\bar{h}_k^2 - m^2 - n^2)\hat{z}\hat{z}] \right. \\
 & \left. + \frac{r_{12}}{(m^2 + n^2 + \bar{h}_{k+1}^2)^{5/2}} [(\bar{h}_{k+1}^2 - 2m^2 + n^2)\hat{x}\hat{x} + (\bar{h}_{k+1}^2 + m^2 - 2n^2)\hat{y}\hat{y} + (2\bar{h}_{k+1}^2 - m^2 - n^2)\hat{z}\hat{z}] \right\}, \\
 &= \frac{1}{a^3\epsilon_1} \left(\frac{1}{2}\hat{x}\hat{x} + \frac{1}{2}\hat{y}\hat{y} + \hat{z}\hat{z} \right) \tag{3.26}
 \end{aligned}$$

$$\begin{aligned}
 & \times \sum_{k=0}^{\infty} (r_{21}r_{23})^k \sum_{m,n} \left\{ r_{12} \frac{3\bar{h}_k^2 - (m^2 + n^2 + \bar{h}_k^2)}{(m^2 + n^2 + \bar{h}_k^2)^{5/2}} + r_{23} \frac{3\bar{h}_{k+1}^2 - (m^2 + n^2 + \bar{h}_{k+1}^2)}{(m^2 + n^2 + \bar{h}_{k+1}^2)^{5/2}} \right\} \\
 & + \frac{3}{2\epsilon_1 a^3} \sum_{k=0}^{\infty} (r_{21}r_{23})^k \sum_{m,n} (m^2 - n^2) (\hat{x}\hat{x} - \hat{y}\hat{y}) \left(\frac{1}{(m^2 + n^2 + \bar{h}_k^2)^{5/2}} + \frac{1}{(m^2 + n^2 + \bar{h}_{k+1}^2)^{5/2}} \right), \\
 &= \frac{1}{a^3\epsilon_1} B(\bar{h}) \left(\frac{1}{2}\hat{x}\hat{x} + \frac{1}{2}\hat{y}\hat{y} + \hat{z}\hat{z} \right). \tag{3.27}
 \end{aligned}$$

As with Eq. 3.23, the second summation in Eq. 3.26 converges to zero due to symmetry and

$$B(\bar{h}) \equiv \sum_{k=0}^{\infty} (r_{21}r_{23})^k \sum_{m,n} \left\{ r_{12} \frac{3\bar{h}_k^2 - (m^2 + n^2 + \bar{h}_k^2)}{(m^2 + n^2 + \bar{h}_k^2)^{5/2}} + r_{23} \frac{3\bar{h}_{k+1}^2 - (m^2 + n^2 + \bar{h}_{k+1}^2)}{(m^2 + n^2 + \bar{h}_{k+1}^2)^{5/2}} \right\}. \tag{3.28}$$

In the present form of the summations, the summation must be continued over many values of m and n to achieve convergence. To improve the rate of this convergence, we use the trick of summing Eq. 3.28 over reciprocal space. Each of the two terms in the summation are then rewritten according to the equivalent summations as used in [43, 87],

$$\sum_{i,j=-\infty}^{\infty} \frac{3x^2 - [i^2 + j^2 + x^2]}{[i^2 + j^2 + x^2]^{5/2}} = 16\pi^2 \sum_{i=0}^{\infty} \sum_{j=1}^{\infty} \sqrt{i^2 + j^2} e^{-2\pi x \sqrt{i^2 + j^2}}.$$

Recasting Eq. 3.28 using this equivalence yields

$$\begin{aligned}
 B(\bar{h}) &= \sum_{k=0}^{\infty} (r_{21}r_{23})^k \sum_{m,n} \left\{ r_{12}(2\pi)^2 \sqrt{m^2 + n^2} e^{-2\pi\bar{h}_k \sqrt{m^2 + n^2}} + r_{23}(2\pi)^2 \sqrt{m^2 + n^2} e^{-2\pi\bar{h}_{k+1} \sqrt{m^2 + n^2}} \right\}, \\
 &= 4\pi^2 \sum_{k=0}^{\infty} (r_{21}r_{23})^k \sum_{m,n} \sqrt{m^2 + n^2} e^{-2\pi\bar{h} \sqrt{m^2 + n^2}} \left(r_{12} e^{-4\pi k \bar{D}_2 \sqrt{m^2 + n^2}} + r_{23} e^{-4\pi(k+1) \bar{D}_2 \sqrt{m^2 + n^2}} \right), \\
 &= \sum_{m,n} (2\pi)^2 \sqrt{m^2 + n^2} e^{-2\pi\bar{h} \sqrt{m^2 + n^2}} \left(\frac{r_{12}}{1 - r_{21}r_{23} e^{-4\pi \bar{D}_2 \sqrt{m^2 + n^2}}} + \frac{r_{23} e^{-4\pi \bar{D}_2 \sqrt{m^2 + n^2}}}{1 - r_{21}r_{23} e^{-4\pi \bar{D}_2 \sqrt{m^2 + n^2}}} \right), \\
 &= \sum_{m,n} (2\pi)^2 \sqrt{m^2 + n^2} e^{-2\pi\bar{h} \sqrt{m^2 + n^2}} \left(\frac{r_{12} - r_{23} e^{-4\pi \bar{D}_2 \sqrt{m^2 + n^2}}}{1 - r_{21}r_{23} e^{-4\pi \bar{D}_2 \sqrt{m^2 + n^2}}} \right), \\
 &= \frac{2\pi}{a} \mathcal{A} \sum_{m,n} \kappa_{m,n} R_{13}(\kappa_{m,n}) e^{-2h\kappa_{m,n}}, \tag{3.29}
 \end{aligned}$$

where $\bar{h} = 2h/a$ as before and in a similar fashion $\bar{D}_2 = 2D_2/a$. In Eq. 3.29, κ is recognized as the reciprocal lattice vector, given by $\frac{2\pi}{a} \sqrt{m^2 + n^2}$, as expected given that the form of the summation $B(\bar{h})$ is in reciprocal space.

With all the terms of Eq. 2.45 adapted for the presence of the finite layer, Eq. 2.47 can now be resolved into explicit expressions for its components. This results in the necessary expressions for Eqs. 2.23 and 2.25 to determine the response of the selvedge in the \hat{s} , $\hat{\kappa}$, and \hat{z} directions, respectively

$$n_{os} = \frac{4\pi i \tilde{\omega}^2 a}{w_1} \left(\frac{\alpha}{8\pi \varepsilon_0 \varepsilon_1 a^3 - \alpha(A + B(\bar{h}))} \right), \tag{3.30}$$

$$n_{o\kappa} = 4\pi i w_1 a \left(\frac{\alpha}{8\pi \varepsilon_0 \varepsilon_1 a^3 - \alpha(A + B(\bar{h}))} \right), \text{ and} \tag{3.31}$$

$$n_{oz} = \frac{2\pi i \kappa^2 a}{w_1} \left(\frac{\alpha}{4\pi \varepsilon_0 \varepsilon_1 a^3 + \alpha(A - B(\bar{h}))} \right). \tag{3.32}$$

The variable α is the polarizability of a spherical particle in the dipole approximation and is given by,

$$\alpha = 4\pi \varepsilon_0 \varepsilon_1 \left(\frac{\varepsilon - \varepsilon_1}{\varepsilon + 2\varepsilon_1} \right) b^3. \tag{3.33}$$

3.4 The Solution Condition for the Waveguide Modes

With the response of the selvedge layer determined, the effect of the finite layer on the modes of the waveguide system will now be determined. This treatment determines the

modes in the absence of the selvedge layer in accordance with the procedure outlined in chapter 2. The solution condition is determined in a similar fashion as [43] with the addition of a parameter U to treat the finite layer. In keeping with the notation of [43], we see that

$$\begin{aligned} w_1 &= iQ, \\ w_2 &= iU, \\ w_3 &= h, \\ w_4 &= iP, \end{aligned} \tag{3.34}$$

where

$$\begin{aligned} h &= \sqrt{\tilde{\omega}^2 n_3^2 - \kappa^2}, \\ Q &= a_Q \sqrt{\kappa^2 - \tilde{\omega}^2 n_1^2} = a_Q \sqrt{\tilde{\omega}^2 (n_3^2 - n_1^2) - h^2}, \\ U &= a_U \sqrt{\kappa^2 - \tilde{\omega}^2 n_2^2} = a_U \sqrt{\tilde{\omega}^2 (n_3^2 - n_2^2) - h^2}, \\ P &= a_P \sqrt{\kappa^2 - \tilde{\omega}^2 n_4^2} = a_P \sqrt{\tilde{\omega}^2 (n_3^2 - n_4^2) - h^2}, \end{aligned} \tag{3.35}$$

and

$$\begin{aligned} a_Q &= 1 \text{ (s-pol)} = \frac{n_3^2}{n_1^2} \text{ (p-pol)}, \\ a_U &= 1 \text{ (s-pol)} = \frac{n_3^2}{n_2^2} \text{ (p-pol)}, \\ a_P &= 1 \text{ (s-pol)} = \frac{n_3^2}{n_4^2} \text{ (p-pol)}. \end{aligned} \tag{3.36}$$

Unlike previous sections, here we do not use an electrostatic approximation. The Fresnel reflection coefficients are given by [78, 79]

$$\begin{aligned} r_{12} &= \frac{w_1 - w_2}{w_1 + w_2} = \frac{Q - U}{Q + U}, \\ r_{32} &= \frac{w_3 - w_2}{w_3 + w_2} = \frac{h - iU}{h + iU}, \\ r_{34} &= \frac{w_3 - w_4}{w_3 + w_4} = \frac{h - iP}{h + iP}. \end{aligned} \tag{3.37}$$

To determine the reflection coefficient of the entire multilayer structure, we use the transfer

matrix approach of [79], in which

$$\begin{aligned}
 M_{14} &= \frac{1}{t_{12}} \begin{bmatrix} 1 & r_{12} \\ r_{12} & 1 \end{bmatrix} \begin{bmatrix} e^{iw_2 D_2} & 0 \\ 0 & e^{-iw_2 D_2} \end{bmatrix} \frac{1}{t_{23}} \begin{bmatrix} 1 & r_{23} \\ r_{23} & 1 \end{bmatrix} \begin{bmatrix} e^{iw_3 D_3} & 0 \\ 0 & e^{-iw_3 D_3} \end{bmatrix} \frac{1}{t_{34}} \begin{bmatrix} 1 & r_{34} \\ r_{34} & 1 \end{bmatrix}, \\
 &= \frac{1}{t_{12} t_{23} t_{34}} \begin{bmatrix} m_{11} & m_{12} \\ m_{21} & m_{22} \end{bmatrix},
 \end{aligned} \tag{3.38}$$

where

$$\begin{aligned}
 m_{11} &= (e^{2iw_2 D_2} + r_{12} r_{23}) e^{2iw_3 D_3} + r_{34} (r_{12} + r_{23} e^{2iw_2 D_2}), \\
 m_{12} &= r_{34} (e^{2iw_2 D_2} + r_{12} r_{23}) e^{2iw_3 D_3} + r_{12} + r_{23} e^{2iw_2 D_2}, \\
 m_{21} &= (r_{23} + r_{12} e^{2iw_2 D_2}) e^{2iw_3 D_3} + r_{34} (1 + r_{12} r_{23} e^{2iw_2 D_2}), \\
 m_{22} &= r_{34} (r_{23} + r_{12} e^{2iw_2 D_2}) e^{2iw_3 D_3} + 1 + r_{12} r_{23} e^{2iw_2 D_2}.
 \end{aligned}$$

A comparison with the generalized form of a transfer matrix across a multilayer system [43]

$$M_{14} = \begin{bmatrix} \frac{T_{14} T_{41} - R_{14} R_{41}}{T_{14}} & \frac{R_{14}}{T_{14}} \\ -\frac{R_{41}}{T_{14}} & \frac{1}{T_{14}} \end{bmatrix}, \tag{3.39}$$

in which R_{ij} and T_{ij} are the reflection and transmission coefficients from medium i to medium j respectively, allows one to determine the reflection coefficient to be

$$\begin{aligned}
 R_{14} &= \frac{m_{12}}{m_{22}} \\
 &= \frac{r_{12} (1 - r_{32} r_{34} e^{2iw_3 D_3}) - (r_{32} - r_{34} e^{2iw_3 D_3}) e^{2iw_2 D_2}}{1 - r_{32} r_{34} e^{2iw_3 D_3} - r_{12} (r_{32} - r_{34} e^{2iw_3 D_3}) e^{2iw_2 D_2}}.
 \end{aligned} \tag{3.40}$$

Setting the denominator of Eq. 3.40 to zero allows one to determine the poles of the multilayer structure. As the poles represent a divergence in the reflection coefficient and signals the mode at which resonance will occur [79, 88–91]. Thus,

$$\begin{aligned}
 0 &= 1 - r_{32} r_{34} e^{2iw_3 D_3} - r_{12} r_{32} e^{2iw_2 D_2} + r_{12} r_{34} e^{2iw_3 D_3 + 2iw_2 D_2}, \text{ and} \\
 e^{2iw_3 D_3} &= \frac{1 - r_{12} r_{32} e^{2iw_2 D_2}}{r_{32} r_{34} - r_{12} r_{34} e^{2iw_2 D_2}}.
 \end{aligned} \tag{3.41}$$

After making the appropriate substitutions and adding 1 to both sides this becomes

$$e^{2ih D_3} + 1 = \frac{2[(h^2 - UP)(Q + U)] - 2[(h^2 + UP)(Q - U)] e^{-2UD_2}}{(Q + U)(h - iP)(h - iU) - (Q - U)(h - iP)(h + iU) e^{-2UD_2}}, \tag{3.42}$$

the real and imaginary components of which are given by

$$\begin{aligned}\Re(e^{2ihD_3} + 1) &= 1 + \cos(2hD_3) \\ &= \frac{2}{\Omega} [(h^2 - UP)(Q + U) - (h^2 + UP)(Q - U)e^{-2UD_2}]^2,\end{aligned}$$

and

$$\begin{aligned}\Im(e^{2ihD_3} + 1) &= \sin(2hD_3) \\ &= \frac{2h}{\Omega} [(h^2 - UP)(Q + U) - (h^2 + UP)(Q - U)e^{-2UD_2}] \\ &\quad \times [(Q + U)(U + P) + (Q - U)(U - P)e^{-2UD_2}].\end{aligned}$$

The term denoted by Ω is the rationalized denominator of Eq. 3.42,

$$\begin{aligned}\Omega &= [(h^2 - UP)(Q + U) - (h^2 + UP)(Q - U)e^{-2UD_2}]^2 \\ &\quad + h^2 [(Q + U)(U + P) + (Q - U)(U - P)e^{-2UD_2}]^2.\end{aligned}$$

Using the trigonometric identity

$$\begin{aligned}\cot(hD_3) &= \frac{1 + \cos(2hD_3)}{\sin(2hD_3)} \\ &= \frac{\Re(e^{2ihD_3} + 1)}{\Im(e^{2ihD_3} + 1)},\end{aligned}\tag{3.43}$$

after some simplifications, the solution condition is then found to be

$$\cot(hD_3) = \frac{(h^2 - UP)(Q + U) - (h^2 + UP)(Q - U)e^{-2UD_2}}{h[(Q + U)(U + P) + (Q - U)(U - P)e^{-2UD_2}]}.\tag{3.44}$$

3.5 The Expansion Parameter: ρ_{14}

To fully characterize the effects of the finite layer, the expansion parameter, ρ_{14} , of Eq. 2.35, must be derived from a pole expansion of the reflection coefficient given by Eq. 3.40.

The parameter is defined such that

$$R_{14} = \frac{\rho_{14}}{\kappa - \kappa_o} = \frac{N}{A(\kappa - \kappa_o)},\tag{3.45}$$

$$\rho_{14} = \frac{N}{A}.\tag{3.46}$$

To determine the denominator, A , of ρ_{14} , we take the derivative of the denominator of Eq. 3.40,

$$\begin{aligned} A &= \frac{\partial}{\partial \kappa} \left(1 + r_{23}r_{34}e^{2ihD_3} + r_{12}r_{23}e^{-2UD_2} + r_{12}r_{34}e^{2ihD_3-2UD_2} \right) \\ &= \left(\frac{1}{r_{12}} \frac{\partial r_{12}}{\partial \kappa} + \frac{1}{r_{23}} \frac{\partial r_{23}}{\partial \kappa} - 2UD_2 \frac{\partial U}{\partial \kappa} \right) r_{12}r_{23}e^{-2UD_2} \\ &\quad + \left(\frac{1}{r_{23}} \frac{\partial r_{23}}{\partial \kappa} + \frac{1}{r_{34}} \frac{\partial r_{34}}{\partial \kappa} + 2iD_3 \frac{\partial h}{\partial \kappa} \right) r_{23}r_{34}e^{2ihD_3} \\ &\quad + \left(\frac{1}{r_{12}} \frac{\partial r_{12}}{\partial \kappa} + \frac{1}{r_{34}} \frac{\partial r_{34}}{\partial \kappa} + 2 \frac{\partial}{\partial \kappa} (ihD_3 - UD_2) \right) r_{12}r_{34}e^{2(ihD_3-UD_2)}. \end{aligned}$$

Using

$$\begin{aligned} D_2^{eff} &= \frac{ih}{2\kappa} \left[\frac{1}{r_{12}} \frac{\partial r_{12}}{\partial \kappa} + \frac{1}{r_{23}} \frac{\partial r_{23}}{\partial \kappa} - 2D_2 \frac{\partial U}{\partial \kappa} \right], \\ D_3^{eff} &= \frac{ih}{2\kappa} \left[\frac{1}{r_{23}} \frac{\partial r_{23}}{\partial \kappa} + \frac{1}{r_{34}} \frac{\partial r_{34}}{\partial \kappa} + 2iD_3 \frac{\partial h}{\partial \kappa} \right], \text{ and} \\ D_{23}^{eff} &= \frac{ih}{2\kappa} \left[\frac{1}{r_{12}} \frac{\partial r_{12}}{\partial \kappa} + \frac{1}{r_{34}} \frac{\partial r_{34}}{\partial \kappa} + 2 \frac{\partial}{\partial \kappa} (ihD_3 - UD_2) \right], \end{aligned} \quad (3.47)$$

we write A as

$$A = \frac{-2i\kappa}{h} \left[r_{12}r_{23}D_2^{eff}e^{-2UD_2} + r_{23}r_{34}D_3^{eff}e^{2ihD_3} + r_{12}r_{34}D_{23}^{eff}e^{2(ihD_3-UD_2)} \right]. \quad (3.48)$$

Performing the differentiations of 3.48 yields,

$$A = \frac{2i\kappa_o}{h} \left(r_{12}^o r_{32}^o D_2^{eff} e^{-2U_o D_2} + r_{32}^o r_{34}^o D_3^{eff} e^{2ih_o D_3} - r_{12}^o r_{34}^o D_{23}^{eff} e^{2(ih_o D_3 - U_o D_2)} \right), \quad (3.49)$$

where

$$\begin{aligned} D_2^{eff} &= \frac{ih}{2\kappa_o} \left[\frac{1}{r_{12}} \frac{\partial r_{12}}{\partial \kappa} + \frac{1}{r_{23}} \frac{\partial r_{23}}{\partial \kappa} - 2D_2 \frac{\partial U}{\partial \kappa} \right] \\ &= \frac{-ih_o a_U^2}{U_o} D_2 + \frac{1}{U_o} \left(\frac{a_U^2 h_o^2 + U_o^2}{h_o^2 + U_o^2} \right) - \frac{ih_o}{Q_o U_o} \left(\frac{a_U^2 Q_o^2 - a_Q^2 U_o^2}{Q_o^2 - U_o^2} \right), \end{aligned} \quad (3.50)$$

$$\begin{aligned} D_3^{eff} &= \frac{ih}{2\kappa_o} \left[\frac{1}{r_{23}} \frac{\partial r_{23}}{\partial \kappa} + \frac{1}{r_{34}} \frac{\partial r_{34}}{\partial \kappa} + 2iD_3 \frac{\partial h}{\partial \kappa} \right] \\ &= D_3 + \frac{1}{U_o} \left(\frac{a_U^2 h_o^2 + U_o^2}{h_o^2 + U_o^2} \right) + \frac{1}{P_o} \left(\frac{a_P^2 h_o^2 + P_o^2}{h_o^2 + P_o^2} \right), \end{aligned} \quad (3.51)$$

$$\begin{aligned} D_{23}^{eff} &= \frac{ih}{2\kappa_o} \left[\frac{1}{r_{12}} \frac{\partial r_{12}}{\partial \kappa} + \frac{1}{r_{34}} \frac{\partial r_{34}}{\partial \kappa} + 2 \frac{\partial}{\partial \kappa} (ihD_3 - UD_2) \right] \\ &= D_3 - \frac{ih_o a_U^2}{U_o} D_2 - \frac{ih_o}{Q_o U_o} \left(\frac{a_U^2 Q_o^2 - a_Q^2 U_o^2}{Q_o^2 - U_o^2} \right) + \frac{1}{P_o} \left(\frac{a_P^2 h_o^2 + P_o^2}{h_o^2 + P_o^2} \right). \end{aligned} \quad (3.52)$$

The variable modifier o is used to denote that the differentiation is performed at $\kappa = \kappa_o$, the waveguide mode at which R_{14} diverges. Additionally, one can see that

$$\begin{aligned} (1 - r_{34}^o r_{32}^o e^{2iw_3 D_3}) - r_{12}^o (r_{32}^o - r_{34}^o e^{2iw_3 D_3}) e^{2iw_2 D_2} &= 0. \\ (1 - r_{34}^o r_{32}^o e^{2iw_3 D_3}) &= r_{12}^o (r_{32}^o - r_{34}^o e^{2iw_3 D_3}) e^{2iw_2 D_2}. \end{aligned}$$

Eq. 3.53 will now allow the numerator of R_{14} to be simplified.

$$\begin{aligned} \mathcal{N} = num|_{\kappa=\kappa_o} &= r_{12}^o \left(1 - r_{34}^o r_{32}^o e^{2ih_o D_3} \right) - \left(r_{32}^o - r_{34}^o e^{2ih_o D_3} \right) e^{-2U_o D_2}, \\ &= (r_{12}^o)^2 \left(r_{32}^o - r_{34}^o e^{2ih_o D_3} \right) e^{-2U_o D_2} - \left(r_{32}^o - r_{34}^o e^{2ih_o D_3} \right) e^{-2U_o D_2}, \\ &= [(r_{12}^o)^2 - 1] \left(r_{32}^o - r_{34}^o e^{2ih_o D_3} \right) e^{-2U_o D_2}. \end{aligned} \quad (3.53)$$

After the appropriate substitutions,

$$\mathcal{N} = \frac{-4Q_o U_o e^{-2U D_2} [(h_o - iU_o)(h_o + iP_o) - (h_o - iP_o)(h_o + iU_o) e^{2ih_o D_3}]}{(Q_o + U_o)^2 (h_o + iU_o)(h_o + iP_o)}. \quad (3.54)$$

Thus, the expansion parameter is given by

$$\begin{aligned} \rho_{14} &= \frac{\mathcal{N}}{A} \\ &= \frac{h_o [(r_{12}^o)^2 - 1] (r_{32}^o - r_{34}^o e^{2ih_o D_3})}{2i\kappa_o \left(r_{12}^o r_{32}^o D_2^{eff} + r_{32}^o r_{34}^o D_3^{eff} e^{2(ih_o D_3 + U_o D_2)} - r_{12}^o r_{34}^o D_{23}^{eff} e^{2ih_o D_3} \right)}. \end{aligned} \quad (3.55)$$

After some algebraic manipulation, this can also be expressed as,

$$\rho_{14} = \frac{2ih_o Q_o U_o}{\kappa_o(Q_o^2 - U_o^2)} \left(\frac{L_2 - L_{23}e^{2ih_o D_3}}{L_2 D_2^{eff} + L_3 D_3^{eff} e^{2(ih_o D_3 + U_o D_2)} - L_{23} D_{23}^{eff} e^{2ih_o D_3}} \right), \quad (3.56)$$

where

$$L_2 = (Q_o^2 - U^2)(h_o - iP_o)(h_o + iU_o),$$

$$L_3 = (Q_o + U_o)^2(h_o - iP_o)(h_o - iU_o),$$

$$L_{23} = (Q_o^2 - U^2)(h_o + iP_o)(h_o - iU_o).$$

It should be noted that Eq. 3.56 has been included to express ρ_{14} in a similar form to Eq. E7 of [43], which will facilitate a comparison in the limiting cases of the next section.

3.6 Limiting Cases

If the expressions characterizing the effects of the finite layer are to be considered correct, they must agree with their original counterparts from [43] in the limit $D_2 \rightarrow 0$. In taking this limit, one must note that

$$\begin{aligned} \varepsilon_2 &\rightarrow \varepsilon_3, \\ w_2 &\rightarrow w_3, \end{aligned} \quad (3.57)$$

leading to

$$U \rightarrow \pm ih. \quad (3.58)$$

In order to satisfy the boundary conditions at the first and second interfaces we will choose

$$U \rightarrow -ih. \quad (3.59)$$

This results in

$$\begin{aligned}
 a_U &\rightarrow 1, \\
 r_{12} &\rightarrow r_{13}, \\
 r_{32} &\rightarrow 0, \\
 L_3 &\rightarrow 0, \\
 L_{23} &\rightarrow 0,
 \end{aligned} \tag{3.60}$$

as expected. Using the relations of 3.60, all expressions involving contributions from the finite layer quickly reduce to their original counterparts from [43].

$$\begin{aligned}
 R_{14} &= \frac{r_{12} (1 - r_{34} r_{32} e^{2w_3 D_3}) - (r_{32} - r_{34} e^{2iw_3 D}) e^{2iw_2 D_2}}{(1 - r_{34} r_{32} e^{2iw_3 D_3}) - r_{12} (r_{32} - r_{34} e^{2iw_3 D_3}) e^{2iw_2 D_2}} \\
 &\rightarrow \frac{r_{13} + r_{34} e^{2iw_3 D_3}}{1 - r_{13} r_{34} e^{2iw_3 D_3}},
 \end{aligned}$$

$$\begin{aligned}
 B(\bar{h}) &= 4\pi^2 \sum_{m,n} \sqrt{m^2 + n^2} e^{-2\pi\bar{h}\sqrt{m^2+n^2}} \left(\frac{r_{12} + r_{23} e^{-4\pi\bar{D}_2\sqrt{m^2+n^2}}}{1 - r_{21} r_{23} e^{-4\pi\bar{D}_2\sqrt{m^2+n^2}}} \right) \\
 &\rightarrow 4\pi^2 r_{13} \sum_{m,n} \sqrt{m^2 + n^2} e^{-2\pi\bar{h}\sqrt{m^2+n^2}}, \\
 &= 4\pi^2 \frac{\epsilon_3 - \epsilon_1}{\epsilon_3 + \epsilon_1} \sum_{m,n} \sqrt{m^2 + n^2} e^{-2\pi\bar{h}\sqrt{m^2+n^2}},
 \end{aligned}$$

$$\begin{aligned}
 \cot(hD_3) &= \frac{(h^2 - UP)(Q + U) - (h^2 + UP)(Q - U)e^{-2UD_2}}{h[(Q + U)(U + P) + (Q - U)(U - P)e^{-2UD_2}]}, \\
 &\rightarrow \frac{h^2 - PQ}{h(Q + P)} \\
 &= \frac{h - \frac{PQ}{h}}{Q + P},
 \end{aligned}$$

$$\begin{aligned}\rho_{14} &= \frac{2ih_o Q_o U_o}{\kappa_o(Q_o^2 - U_o^2)} \left(\frac{L_2 - L_{23}e^{2ih_o D_3}}{L_2 D_2^{eff} + L_3 D_3^{eff} e^{2(ih_o D_3 + U_o D_2)} - L_{23} D_{23}^{eff} e^{2ih_o D_3}} \right) \\ &\rightarrow \frac{2h_o^2 Q_o}{\kappa(Q_o^2 + h_o^2) D_{23}^{eff}},\end{aligned}$$

where

$$\begin{aligned}D_{23}^{eff} &= D_3 - \frac{ih_o a_U^2}{U_o} D_2 - \frac{ih_o}{Q_o U_o} \left(\frac{a_U^2 Q_o^2 - a_Q^2 U_o^2}{Q_o^2 - U_o^2} \right) + \frac{1}{P_o} \left(\frac{a_P^2 h_o^2 + P_o^2}{h_o^2 + P_o^2} \right) \\ &\rightarrow D_3 + \frac{1}{Q_o} \left(\frac{a_Q^2 h_o^2 + Q_o^2}{h_o^2 + Q_o^2} \right) + \frac{1}{P_o} \left(\frac{a_P^2 h_o^2 + P_o^2}{h_o^2 + P_o^2} \right).\end{aligned}$$

As all the derived expressions have been shown to agree with [43] as $D_2 \rightarrow 0$, the effects of D_2 on the parameters of the hybrid sensor can now be determined. These will be shown in the following section.

3.7 Effects of D_2 on the Hybrid Sensor

Numerical results over the domain $D_2 \geq 0$ can be found in figures 3.2 and 3.3. From figure 3.2, it is seen that both absorption and changes to the waveguide mode are inversely proportional to D_2 . An initial increase for $D_2 = 1$ nm can be seen and is attributed to the additional reflections across the multilayer structure due to the presence of the additional layer. By inspection of figure 3.3, one can see the exponential decay of the imaginary component of the resonant waveguide mode, κ'_o . This corresponds to a loss of all sensing information concerning the analyte relayed from the nanoparticle array. As this occurs for $D_2 \approx 200$ nm, the results indicate the performance of sensor in which the nanoparticles are deposited using some variant of a tethering layer would not be significantly affected for thin layers. This concludes the discussion of the tethering layer; in all proceeding computations, $D_2 = 2$ nm as it commonly used in many experiments [92–95].

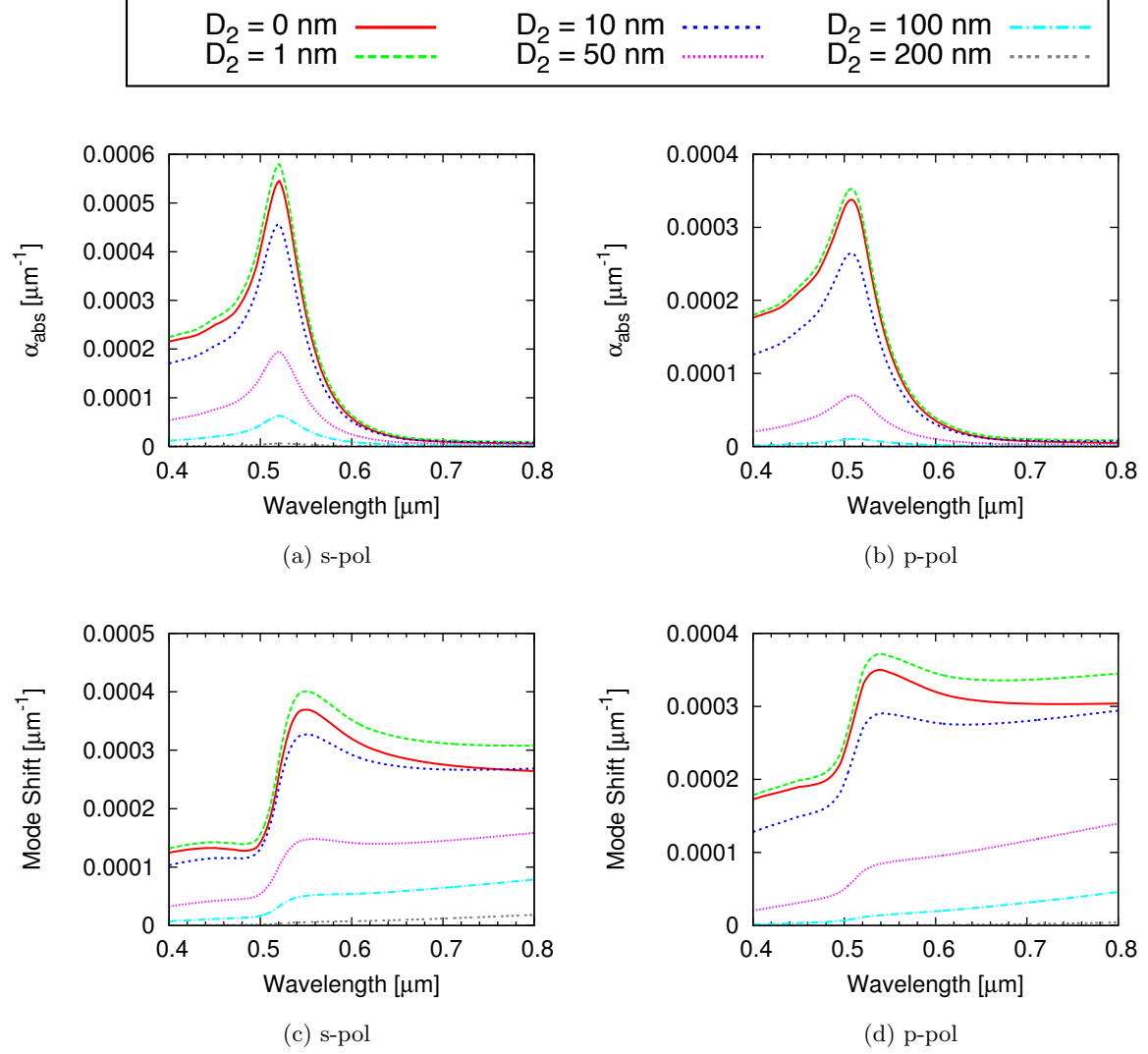


Figure 3.2: Effects of various finite layer thicknesses, D_2 on the changes in absorption spectra and waveguide mode results. Particle size and spacing are $b=5$ nm and $a=25$ nm, respectively.

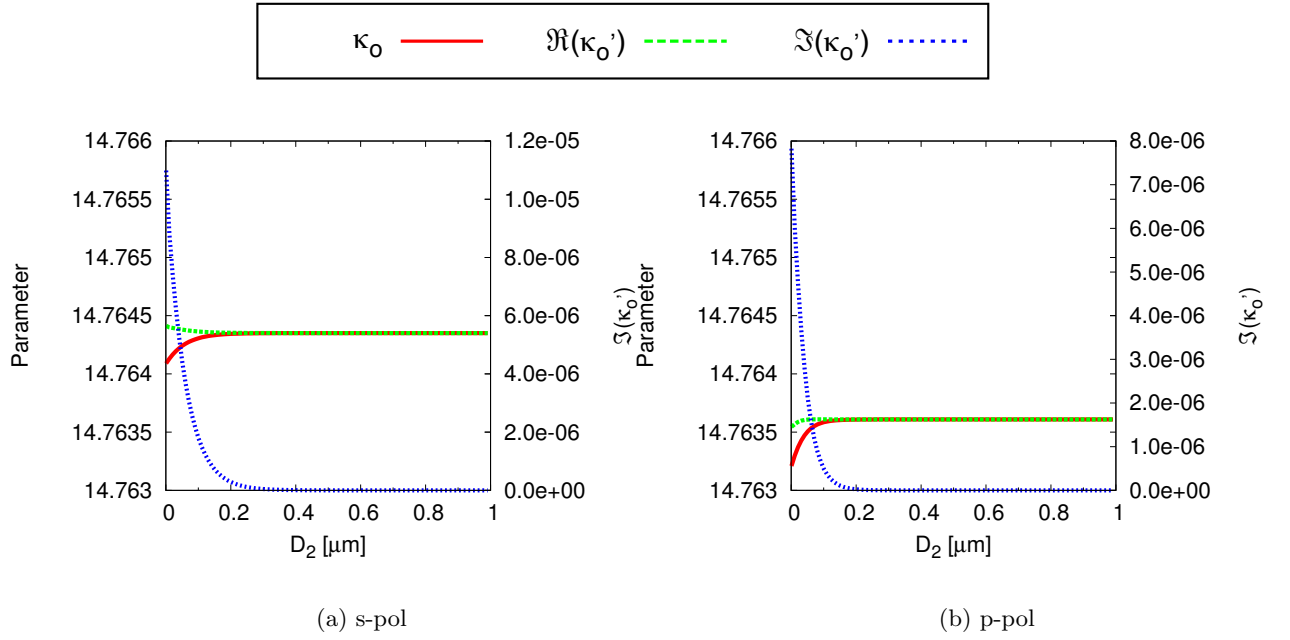


Figure 3.3: Plots showing the relationship between κ_o and κ'_o as a function of the thickness of the tethering layer for the GNP sensor.

Chapter 4

Characterization of Turbid Media

In this chapter, we will determine the effects of an absorbing cladding medium on the hybrid sensor. This models the case for bulk sensing of turbid media, which as discussed in chapter 1 are characterized by a complex refractive index. The approach used will be the same as that discussed in chapters 2 and 3. The effects of a complex refractive index, are better modelled through a complex dielectric constant ε . As such, unlike in previous chapters where $\varepsilon_1 \in \mathbb{R}$, for the remainder of this work

$$\varepsilon_1 \in \mathbb{C}.$$

The relationship between the dielectric constant of the medium and its refractive index, $\varepsilon_1 = n_1^2$ is still valid; however it is important to note the real and imaginary components of $\varepsilon_1 = \varepsilon_{1r} + i\varepsilon_{1i}$ are related to both components of the refractive index. This is given by

$$\varepsilon_{1r} = n_{1r}^2 - n_{1i}^2,$$

$$\varepsilon_{1i} = 2n_{1r}n_{1i}.$$

The effects of the complex ε_1 will be propagated through Eq. 3.37 for the Fresnel coefficient r_{12} . However, only parameters in which the real and imaginary components must be separated and those including differentiated terms, will be need to be explicitly modified. All

other terms involving ε_1 can remain as previously used, so long as their newfound complex nature is taken into consideration when performing the calculations.

4.1 Solution Condition

To determine the solution condition of the waveguide mode of the bare multilayer structure, the same procedure employed in chapter 3 will be used again. The only exception is the complex nature of ε_1 will result in the following additional considerations:

$$w_1 = \beta + iQ, \quad (4.1)$$

$$r_{12} = \frac{w_1 - w_2}{w_1 + w_2} = \frac{\beta + i(Q - U)}{\beta + i(Q + iU)}. \quad (4.2)$$

Furthermore, the coefficient a_Q , previously associated with the parameter Q , will now become complex valued for p-polarized incident light. It will be separated into its real and imaginary components such that

$$a_Q = a_r + ia_i, \quad (4.3)$$

and also be applied to the new parameter β .

Substituting Eqs. 4.1 and 4.2 into Eq. 3.41 results in

$$e^{2ihD_3} + 1 = \frac{1 - \left(\frac{\beta + i(Q - U)}{\beta + i(Q + iU)} \right) \left(\frac{h - iU}{h + iU} \right) e^{-2UD_2}}{\left(\frac{h - iU}{h + iU} \right) \left(\frac{h - iP}{h + iP} \right) - \left(\frac{\beta + i(Q - U)}{\beta + i(Q + iU)} \right) \left(\frac{h - iP}{h + iP} \right) e^{-2UD_2}} + 1,$$

the real and imaginary components of which yield

$$\begin{aligned} \Re \left\{ e^{2ihD_3} + 1 \right\} &= \frac{2}{\Omega} \left[\beta^2 (h^2 - UP - (h^2 + UP) e^{-2UD_2})^2 + ((h^2 - UP)(Q + U) \right. \\ &\quad \left. - (h^2 + UP)(Q - U) e^{-2UD_2})^2 - 4h\beta U^2 (h^2 + P^2) e^{-2UD_2} \right], \text{ and} \\ \Im \left\{ e^{2ihD_3} + 1 \right\} &= \frac{2}{\Omega} \left[h\beta^2 (h^2 - UP - (h + UP) e^{-2UD_2}) (U + P + (U - P) e^{-2UD_2}) \right. \\ &\quad \left. + h [(h^2 - UP)(Q + U) - (h^2 + UP)(Q - U) e^{-2UD_2}] [(h^2 - UP)(Q + U) \right. \\ &\quad \left. - (h^2 + UP)(Q - U) e^{-2UD_2}] \right]. \end{aligned}$$

The rationalized denominator of the above components are denoted by Ω , in keeping with the formalism of chapter 3. Here it is given by

$$\Omega = (\beta [h^2 - UP - (h^2 + UP) e^{-2UD_2}] + h [(Q + U)(U + P) + (Q - U)(U - P) e^{-2UD_2}])^2 + ((h^2 - UP)(Q + U) - (h^2 + UP)(Q - U) e^{2UD_2} - h\beta [U + P + (U - P) e^{-2UD_2}])^2.$$

Once again using Eq. 3.43, determines the solution condition as

$$\cot(hD_3) = \frac{X}{Y}, \quad (4.4)$$

where

$$\begin{aligned} X &= \beta^2 [h^2 - UP - (h^2 + UP) e^{-2UD_2}]^2 + [(h^2 - UP)(Q + U) \\ &\quad - (h^2 + UP)(Q - U) e^{-2UD_2}]^2 - 4h\beta U^2 (h^2 + P^2) e^{-2UD_2}, \text{ and} \\ Y &= h (\beta^2 [h^2 - UP - (h^2 + UP) e^{-2UD_2}] [U + P + (U - P) e^{-2UD_2}] \\ &\quad + [(Q + U)(h^2 - UP) - (Q - U)(h^2 + UP) e^{-2UD_2}] [(Q + U)(U + P) \\ &\quad + (Q - U)(U - P) e^{-2UD_2}]). \end{aligned}$$

4.2 Expansion Parameter

For the most part, the expansion parameter determined in chapter 3 by Eq. 3.55 is valid and will not need to be derived again. However, as the effective lengths D_2, D_3 and D_{23} involve explicit equations for the derivative of r_{12} , new expressions must be determined. Before proceeding, one notes that

$$\begin{aligned} \frac{1}{r_{23}} \frac{\partial r_{23}}{\partial \kappa} &= \frac{-2i\kappa}{hU} \left(\frac{a_u^2 h^2 + U^2}{h^2 + U^2} \right), \\ \frac{1}{r_{34}} \frac{\partial r_{34}}{\partial \kappa} &= \frac{-2i\kappa}{hP} \left(\frac{a_p^2 h^2 + P^2}{h^2 + P^2} \right), \\ \frac{\partial h}{\partial \kappa} &= \frac{-\kappa}{h}, \text{ and} \\ \frac{\partial U}{\partial \kappa} &= \frac{a_u^2 \kappa}{U}. \end{aligned} \quad (4.5)$$

However, before an expression similar to Eqs. 4.5 can be determined for r_{12} , the real and imaginary components of w_1 must be determined and differentiated independently. This

will allow the formalism of chapter 3 to be maintained and facilitate a comparison with [43] in the next section.

Expanding ε_1 as $\varepsilon_1 = \varepsilon_{1r} + i\varepsilon_{1i}$, we see that

$$\begin{aligned} w_1 &= \sqrt{\tilde{\omega}^2 \varepsilon_1 - \kappa^2} \\ &= \sqrt{\tilde{\omega}^2 \varepsilon_{1r} - \kappa^2 + i\tilde{\omega}^2 \varepsilon_{1i}}. \end{aligned} \quad (4.6)$$

From [96], the real and imaginary components of 4.6 can then be determined according to

$$\sqrt{x + iy} = \frac{1}{\sqrt{2}} \left[\sqrt{\sqrt{x^2 + y^2} + x} + i \operatorname{sgn}(y) \sqrt{\sqrt{x^2 + y^2} - x} \right], \quad (4.7)$$

for which

$$\begin{aligned} x &= \tilde{\omega}^2 \varepsilon_{1r} - \kappa^2, \\ y &= \tilde{\omega}^2 \varepsilon_{1i}. \end{aligned}$$

The real and imaginary components of w_1 are thusly found to be

$$\Re(w_1) = \frac{1}{\sqrt{2}} \sqrt{\sqrt{(\tilde{\omega}^2 \varepsilon_{1r} - \kappa^2)^2 + (\tilde{\omega}^2 \varepsilon_{1i})^2} + \tilde{\omega}^2 \varepsilon_{1r} - \kappa^2}, \quad (4.8)$$

and

$$\Im(w_1) = \frac{\operatorname{sgn}(\tilde{\omega}^2 \varepsilon_{1i})}{\sqrt{2}} \sqrt{\sqrt{(\tilde{\omega}^2 \varepsilon_{1r} - \kappa^2)^2 + (\tilde{\omega}^2 \varepsilon_{1i})^2} - \tilde{\omega}^2 \varepsilon_{1r} + \kappa^2}. \quad (4.9)$$

While it is possible to carry out the remaining calculations from this point, as electric fields in medium 1 will be evanescent, by the definitions associated with figure 2.1. This is due to $\kappa < \tilde{\omega}^2 \varepsilon_1$. Thus Eqs. 4.8 and 4.9 are rewritten such that $\sqrt{-1}$ is factored out of each expression. This will also facilitate comparisons with chapter 3 when looking at limiting cases. This leads to

$$\begin{aligned} \Re(w_1) &= \frac{i}{\sqrt{2}} \sqrt{\kappa^2 - \tilde{\omega}^2 \varepsilon_{1r} - \sqrt{(\tilde{\omega}^2 \varepsilon_{1r} - \kappa^2)^2 + (\tilde{\omega}^2 \varepsilon_{1i})^2}} \\ &= if_1, \text{ and} \\ \Im(w_1) &= \frac{i \operatorname{sgn}(\tilde{\omega}^2 \varepsilon_{1i})}{\sqrt{2}} \sqrt{\tilde{\omega}^2 \varepsilon_{1r} - \kappa^2 - \sqrt{(\tilde{\omega}^2 \varepsilon_{1r} - \kappa^2)^2 + (\tilde{\omega}^2 \varepsilon_{1i})^2}} \\ &= if_2. \end{aligned}$$

The terms of Eq. 4.1 are then found to be

$$\beta = -(a_i f_1 + a_r f_2), \quad (4.10)$$

$$Q = a_r f_1 - a_i f_2, \quad (4.11)$$

such that $w_1 = \beta + iQ$ under evanescent conditions. Differentiating with respect to κ yields

$$\frac{\partial Q}{\partial \kappa} = \frac{\kappa}{2} \left[\frac{a_r}{f_1} (1 + \gamma) + \frac{a_i}{f_2} (1 - \gamma) \right], \text{ and} \quad (4.12)$$

$$\frac{\partial \beta}{\partial \kappa} = \frac{\kappa}{2} \left[\frac{a_r}{f_2} (1 - \gamma) - \frac{a_i}{f_1} (1 + \gamma) \right], \quad (4.13)$$

where

$$\begin{aligned} a_r &= \frac{\varepsilon_3 \varepsilon_{1r}}{\varepsilon_{1r}^2 + \varepsilon_{1i}^2}, \\ a_i &= \frac{\varepsilon_3 \varepsilon_{1i}}{\varepsilon_{1r}^2 + \varepsilon_{1i}^2}, \\ \gamma &= \frac{\tilde{\omega}^2 \varepsilon_{1r} - \kappa^2}{\sqrt{(\tilde{\omega}^2 \varepsilon_{1r} - \kappa^2)^2 + (\tilde{\omega}^2 \varepsilon_{1i})^2}}. \end{aligned} \quad (4.14)$$

With of Eqs. 4.13 and 4.12, the derivative of r_{12} can now be determined in a similar fashion to Eqs. 4.5. This results in

$$\begin{aligned} \frac{1}{r_{12}} \frac{\partial r_{12}}{\partial \kappa} &= \left(\frac{\beta + i(Q + U)}{\beta + i(Q - U)} \right) \\ &\quad \times \left[\frac{(\beta + i(Q + U)) \left(\frac{\partial \beta}{\partial \kappa} + i \frac{\partial Q}{\partial \kappa} - i \frac{\partial U}{\partial \kappa} \right) - (\beta + i(Q - U)) \left(\frac{\partial \beta}{\partial \kappa} + i \frac{\partial Q}{\partial \kappa} + i \frac{\partial U}{\partial \kappa} \right)}{(\beta + i(Q + U))^2} \right] \\ &= \frac{2}{(\beta + iQ)^2 + U^2} \left[(Q - i\beta) \frac{\partial U}{\partial \kappa} + U \left(i \frac{\partial \beta}{\partial \kappa} - \frac{\partial Q}{\partial \kappa} \right) \right] \\ &= \frac{2\kappa}{(\beta + iQ)^2 + U^2} \Phi, \end{aligned} \quad (4.15)$$

where

$$\Phi = \frac{a_U^2}{U} (Q - i\beta) - \frac{U}{2} \left[\frac{(a_r + ia_i)}{f_1} (1 + \gamma) + \frac{(a_i - ia_r)}{f_2} (1 - \gamma) \right]. \quad (4.16)$$

Using Eqs. 3.47, the effective distances through each segment of the multilayer structure are then found to be

$$D_2^{eff} = -\frac{ih a_U^2}{U} D_2 + \frac{ih}{(\beta + iQ)^2 + U^2} \Phi + \frac{1}{U} \left(\frac{a_U^2 h^2 + U^2}{h^2 + U^2} \right),$$

$$D_3^{eff} = D_3 + \frac{1}{U_o} \left(\frac{a_U^2 h_o^2 + U_o^2}{h_o^2 + U_o^2} \right) + \frac{1}{P_o} \left(\frac{a_P^2 h_o^2 + P_o^2}{h_o^2 + P_o^2} \right), \quad (4.17)$$

$$D_{23}^{eff} = D_3 + \frac{ih a_U^2}{U} D_2 + \frac{ih}{(\beta + iQ)^2 + U^2} \Phi + \frac{1}{P} \left(\frac{a_P^2 h^2 + P^2}{h^2 + P^2} \right).$$

Finally, with the modified effective distances of Eqs. 4.17, the expansion parameter is written as

$$\rho_{14} = \frac{h \left((r_{12}^o)^2 - 1 \right) (r_{23}^o + r_{34}^o e^{2ihD_3}) e^{-2UD_2}}{2i\kappa_o \left[r_{12}^o r_{23}^o D_2^{eff} e^{-2UD_2} + r_{23}^o r_{34}^o D_3^{eff} e^{2ihD_3} + r_{12}^o r_{34}^o D_{23}^{eff} e^{2(ihD_3 - UD_2)} \right]}, \quad (4.18)$$

just as in chapter 3.

4.3 Limiting Cases

In the limiting case of negligible turbidity,

$$\Im(\varepsilon_1) \rightarrow 0, \text{ and}$$

$$w_1 \rightarrow iQ.$$

Beginning with the expansion parameter, the general form of Eq. 4.18 will not change, as previously discussed. However Eq. 4.16, will change such that

$$\Phi \rightarrow \frac{a_U^2 Q}{U} - \frac{a_Q^2 U}{Q}.$$

The changes to Φ , then in turn affect the effective distances D_2^{eff} and D_{23}^{eff} ,

$$\begin{aligned} D_2^{eff} &\rightarrow \frac{-ih a_U^2}{U} D_2 + \frac{ih}{U^2 - Q^2} \left(\frac{a_U^2 Q}{U} - \frac{a_Q^2 U}{Q} \right) + \frac{1}{U} \left(\frac{a_U^2 h^2 + U^2}{h^2 + U^2} \right) \\ &= \frac{-ih a_U^2}{U} D_2 - \frac{ih}{QU} \left(\frac{a_U^2 Q^2 - a_Q^2 U^2}{Q^2 - U^2} \right) + \frac{1}{U} \left(\frac{a_U^2 h^2 + U^2}{h^2 + U^2} \right), \end{aligned}$$

and

$$\begin{aligned} D_{23}^{eff} &\rightarrow D_3 + \frac{ih a_U^2}{U} D_2 + \frac{ih}{U^2 - Q^2} \left(\frac{a_U^2 Q}{U} - \frac{a_Q^2 U}{Q} \right) + \frac{1}{P} \left(\frac{a_P^2 h^2 + P^2}{h^2 + P^2} \right) \\ &= \frac{-ih a_U^2}{U} D_2 - \frac{ih}{QU} \left(\frac{a_U^2 Q^2 - a_Q^2 U^2}{Q^2 - U^2} \right) + \frac{1}{P} \left(\frac{a_P^2 h^2 + P^2}{h^2 + P^2} \right). \end{aligned}$$

To ensure that

$$\frac{\tilde{\omega}^2 \varepsilon_{1r} - \kappa^2}{\sqrt{(\tilde{\omega}^2 \varepsilon_{1r} - \kappa^2)^2 + (\tilde{\omega}^2 \varepsilon_{1i})^2}} \rightarrow 1,$$

the square root was taken as $\sqrt{(\tilde{\omega}^2 \varepsilon_{1r} - \kappa^2)^2} = \text{sgn}(\tilde{\omega}^2 \varepsilon_{1r} - \kappa^2) |\tilde{\omega}^2 \varepsilon_{1r} - \kappa^2|$.

With the agreement of the terms of the expansion parameters of this chapter and chapter 3, we now turning to the solution condition, Eq. 4.4. One finds that

$$\begin{aligned} X &\rightarrow [(h^2 - UP)(Q + U) - (h^2 + UP)(Q - U)e^{-2UD_2}]^2, \\ Y &\rightarrow h[(Q + U)(h^2 - UP) - (Q - U)(h^2 + UP)e^{-2UD_2}] \\ &\quad \times [(Q + U)(U + P) + (Q - U)(U - P)e^{-2UD_2}], \end{aligned}$$

and

$$\begin{aligned} \cot(hD_3) &= \frac{X}{Y} \\ &= \frac{(h^2 - UP)(Q + U) - (h^2 + UP)(Q - U)e^{-2UD_2}}{h[(Q + U)(U + P) + (Q - U)(U - P)e^{-2UD_2}]} \end{aligned}$$

which is in agreement with the expression derived in chapter 3.

4.4 Effects of $\Im(\varepsilon_I)$ on the Hybrid Sensor

Confident in the derived expressions to model a complex cladding medium, ε_1 , this section will examine the effects of various values of $\Im(\varepsilon_1) = \varepsilon_{1i}$ on the waveguide mode shift and the absorption spectrum of the hybrid sensor. From figure 4.1, one can see that increasing ε_{1i} does not adversely effect the parameters of the hybrid sensor. This is encouraging and suggests the performance of the sensor will not be adversely affected due to the presence of a turbid medium. Additional calculations assessing and comparing the performance of the sensor to that of an SPR sensor will be presented in chapter 5.

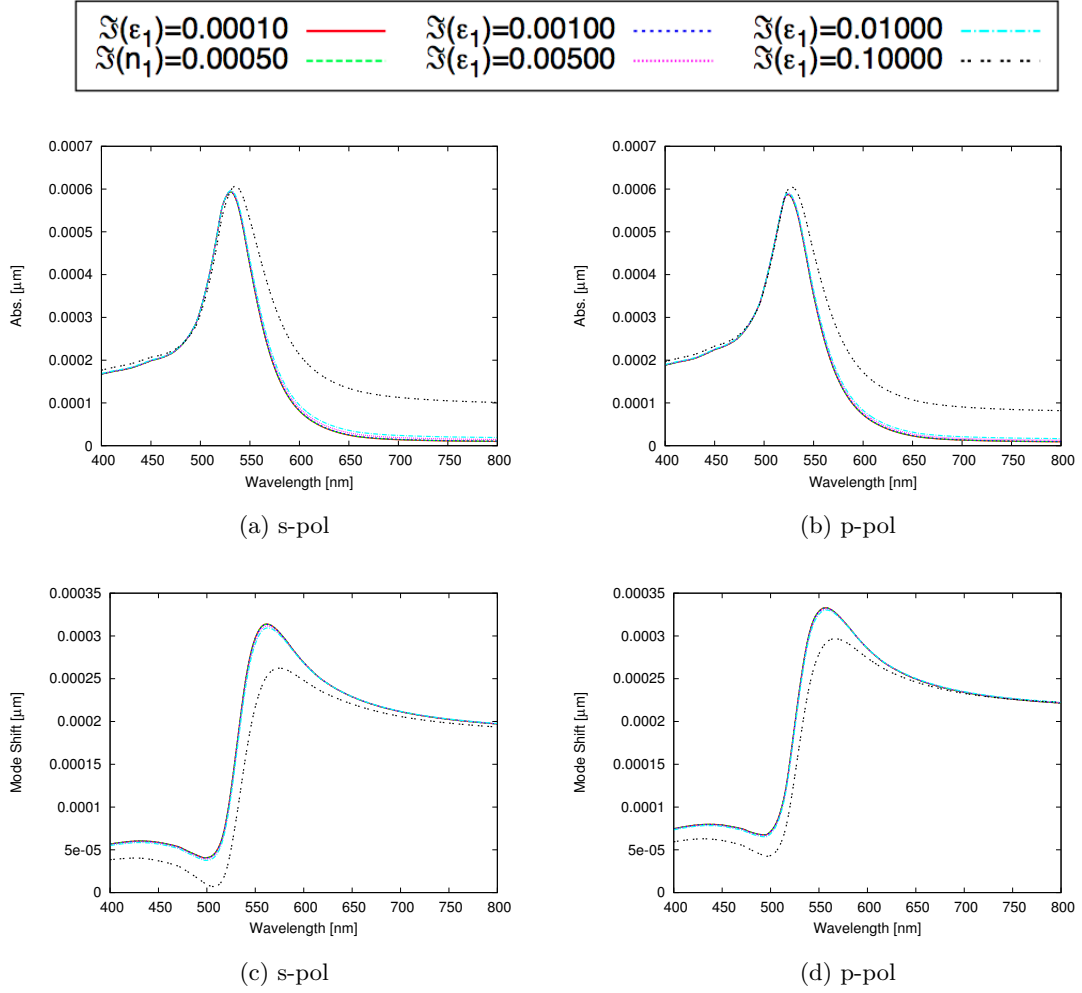


Figure 4.1: Effects of various imaginary dielectric constants, $\Im(\epsilon_1)$ on the changes in absorption spectra and waveguide mode results.

Chapter 5

Results

In this chapter, the performance of the hybrid sensor is calculated using a bulk sensitivity parameter, as defined in 5.1. A similar calculation is made for an SPR sensor, to facilitate a comparison in their performance. These results will initially be presented for transparent media before the turbid case. In the turbid case, results will be separated based on changes to the real and complex components. This is done to highlight the relative contributions of each component to the attenuation experienced in a turbid system.

The results presented in this chapter were computed using the codes found in Appendix C. All calculations were done using Mathworks Matlab version 7.9.0 (R2009b). In all calculations, the refractive index and thickness of the finite layer were held constant at $n_2 = 1.42$ and $D_2 = 2$ nm. The refractive index of the guiding layer was assumed to remain slightly greater than the substrate, $n_3 = n_4 + 0.1$. The refractive index of the substrate, n_4 , was taken as that of BK-7 glass, $n_4 \approx 1.5$. The dielectric data for gold was taken from the data tables of Johnson and Christy [97].

5.1 Figure of Merit

For the purposes of assessing the performance of the hybrid sensor to function with respect to changes in various parameters, a measure describing a benefit-to-cost ratio is needed [98].

In the propagation of an electromagnetic signal, absorption of the signal by the surrounding environment is detrimental to the quality of said signal. Thus, the absorption experienced by the propagating mode, defined as $\alpha = 2\Im(\kappa')$, will be used as the cost in our sensitivity calculation. To function as a sensor, a device must respond to changes with respect to the target analyte. For both the hybrid and SPR sensor, this can be defined as the changes to its propagating mode. Thus the derivative of the changes to the propagating mode will serve as the measure of the benefit of the system. It should be noted that for the hybrid sensor, this mode will be κ' propagating within the guiding layer, however for the SPR sensor, this will be the surface plasmon mode, κ_{SP} , defined by Eq. 1.2. The parameter used to describe the bulk sensitivity of the sensor will thus be given by,

$$H_1 = \frac{1}{\Im(\kappa')} \frac{\partial}{\partial \varepsilon_{1j}} \Re(\kappa'). \quad (5.1)$$

The subscript $1j$ denotes differentiation with respect to either the real ($j=r$) or imaginary ($j=i$) components of the bulk cladding medium.

5.2 Optimal Nanoparticle Configurations and Effects of Particle Size and Spacing

With our figure of merit defined in the previous section, we will now address the fact that the spectral response of the nanoparticle array is dependent upon the particle size and interparticle spacing, before looking at the ability of the hybrid sensor in different dielectric environments. The dependence of the sensing potential on the array parameters is shown in figure 5.1 for changes in (a) the real component and (b) the imaginary component of the dielectric constant of the data. For the remaining figures in this chapter p-polarized incident light, $n_{1r} = 1.36$ and $n_{1i} = 0.00618$ were used in the calculations; however similar results were obtained for the other particle radii, interparticle spacings, values of n_{1r} , n_{1i} , and s-polarized light.

From the changes in sensitivity due to the changes in the nanoparticle array observed in figure 5.1, the question arises whether an optimal configuration exists to maximize the response of the system. To determine if such a configuration exists, H_1 is approximated by

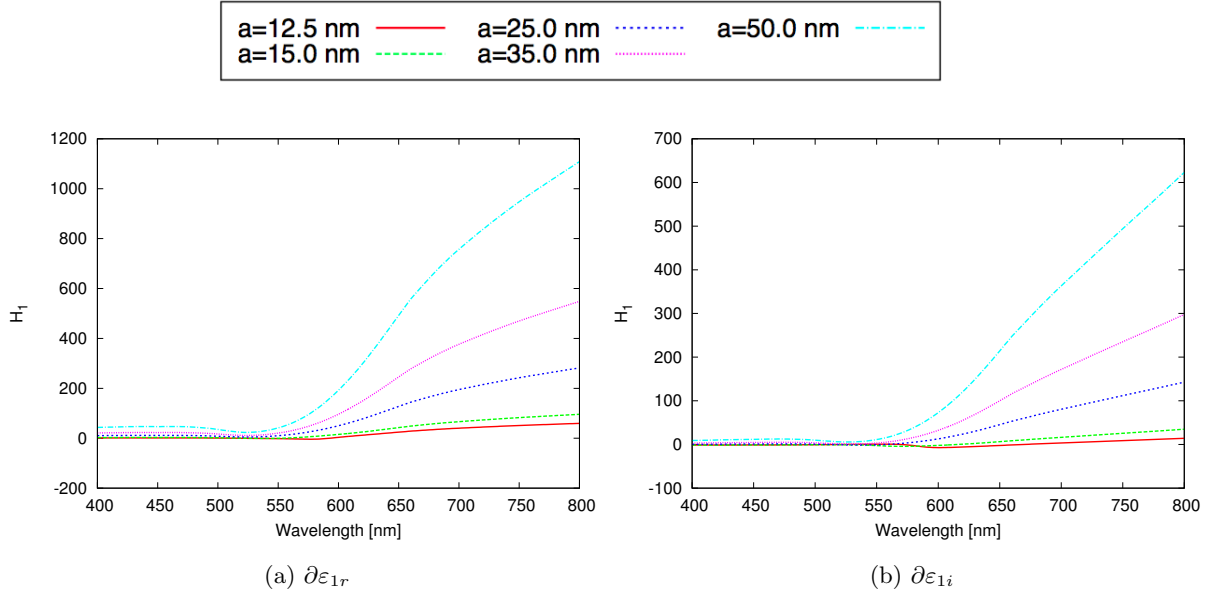


Figure 5.1: Plots of H_1 for nanoparticle arrays with a constant radius of 5 nm and varying interparticle spacings a for (a) a changing real component of the cladding dielectric constant $\partial\epsilon_{1r}$ and (b) a changing imaginary component $\partial\epsilon_{1i}$.

a second order multivariable taylor series expansion to be used in an inequality constrained quadratic programming problem. The result of this expansion is

$$f_1(x) = f_1(x') + c^T(x - x') + \frac{1}{2}(x - x')^T H (x - x'), \quad (5.2)$$

where f_1 denotes the bulk sensitivity parameter H_1 , x is a two variable column vector of the spacing a , and radius b , c is the column vector of first derivatives of H_1 and H is the Hessian matrix of second order partial derivatives of a and b . The expansion is performed at a radius and spacing 1 nm smaller than the size and spacing in question. A comparison between the calculated values of H_1 and the series expansion shows perfect agreement and is shown in figure 5.2.

A mathematical requirement for an optimal solution to exist is for the expression to be either convex or concave, either locally or globally. This occurs when the eigenvalues of the Hessian matrix of the quadratic function are either ≥ 0 or ≤ 0 . From figure 5.3 it can be seen that while the eigenvalues for the particles' size are positive, those of the spacing are negative. Additionally, the spacing eigenvalues are negligible in magnitude compared

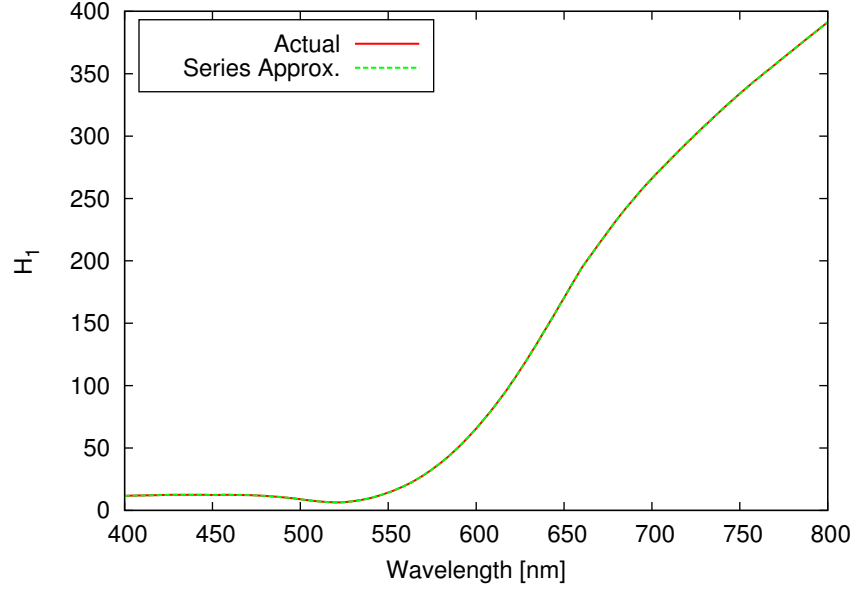


Figure 5.2: Comparison of the Taylor series approximation for H_1 .

to those of the particle size. As the eigenvalues are related to the principle curvature of the function topology, from figure 5.3, one can infer the dominant parameter affecting the sensitivity H_1 to be the particle size. To determine the optimal solution the following problem was solved,

$$\min -f_1(x)$$

subject to

$$A_2x \leq b_2$$

where

$$A_2 = \begin{bmatrix} -1 & 2 \\ 1 & 0 \\ 0 & 1 \\ 0 & -1 \end{bmatrix} \quad x = \begin{bmatrix} a \\ b \end{bmatrix} \quad b_2 = \begin{bmatrix} -0.001 \\ 0.05 \\ 0.01 \\ -0.005 \end{bmatrix}.$$

The inequality constraints used were chosen to restrict the nanoparticle array from particle sizes and spacings outside the valid range of our approximations. In addition to this, they ensure a minimum spacing of 1 nm between the particle surfaces, and the final constraint restricts particle radii below 5 nm, below which the validity of the classical

treatment of the electric fields used in this work breaks down [44]. The solution to the optimization problem determined the maximum sensitivity to occur for $b = 5$ nm and $a = 50$ nm. It is important to remember this result is not guaranteed outside the restrictions imposed in this work, due to the presence of additional interference effects currently not taken into consideration. The constraints for the particle size and spacing also lie on the border of the valid range of particle configurations and were included solely to test the effects of extreme cases. From the eigenvalue plot of figure 5.3, the size of the particles is found to be the dominant factor affecting the sensitivity of the system. For the results presented in the following sections in this chapter, a particle radius of 5 nm will be used with an interparticle spacing of 25 nm. The optimal configuration was purposely not used so that the results presented still retain the potential to be improved with experimental parameters.

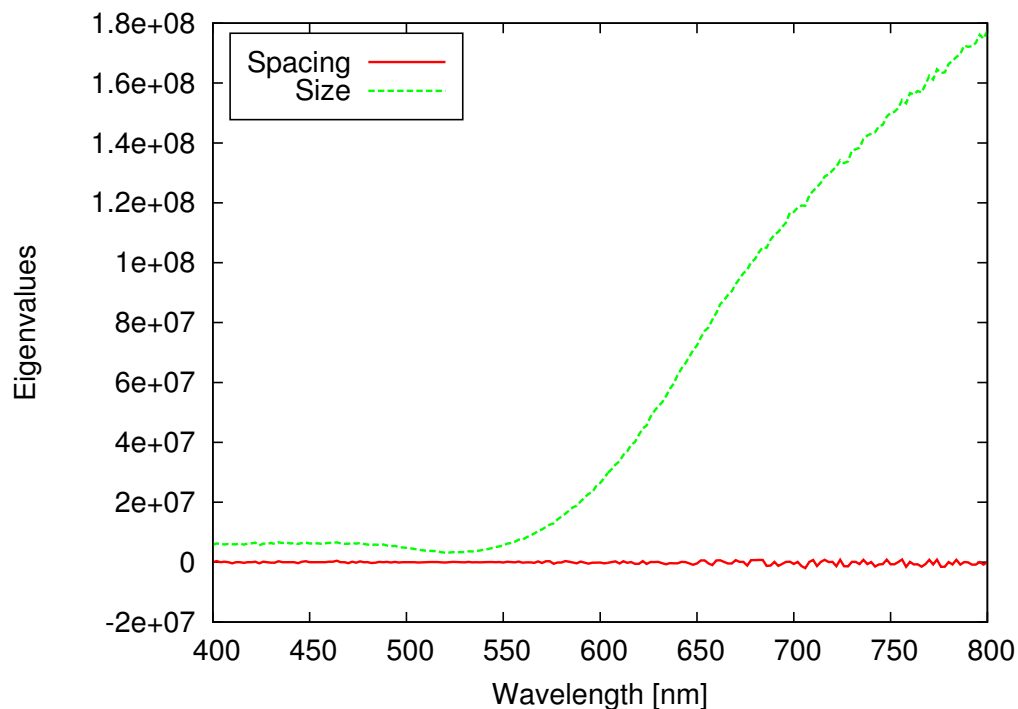


Figure 5.3: H_1 spacing and size eigenvalues over visible spectrum.

5.3 Results for Transparent Media

Before examining how the sensitivity of the sensors are affected by the turbid medium, it is necessary to benchmark their performance in transparent media. From figure 5.4 it can be seen that the sensitivity of the hybrid sensor remains approximately one order of magnitude greater than the SPR sensor.

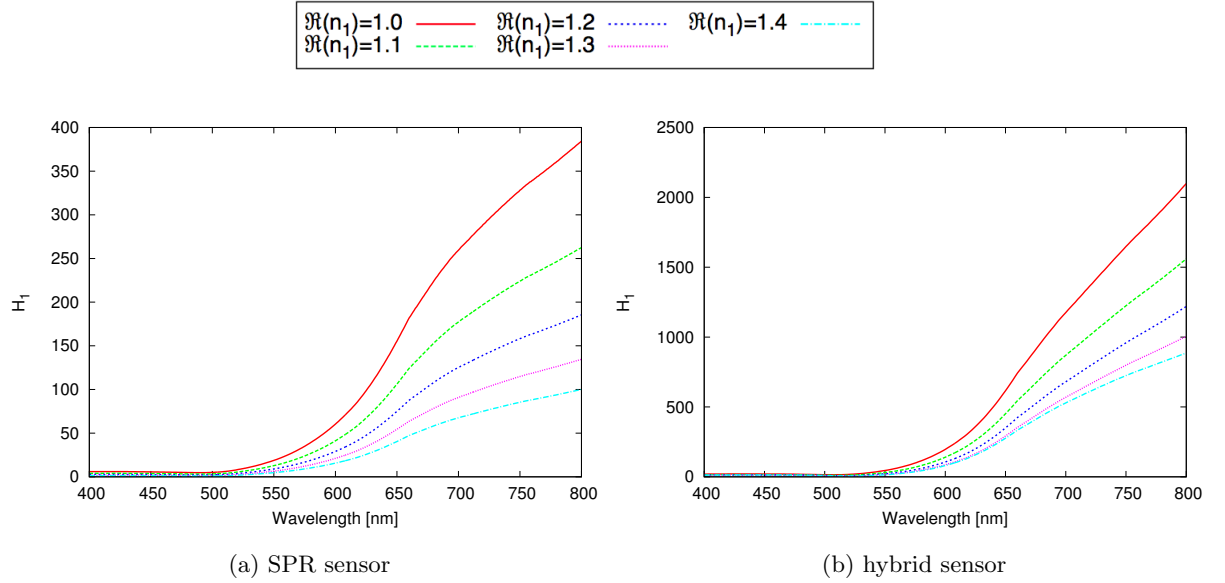


Figure 5.4: H_1 results for a varying $\Re(n_1)$ with the imaginary component held fixed at $\Im(n_1) = 0$ for (a) the SPR sensor and (b) the hybrid sensor. For the hybrid sensor, particles have a radius of 5 nm and are separated by an interparticle spacing of 25 nm.

5.4 Results for Turbid Media

The results shown in figures 5.5 and 5.6 are the bulk sensing sensitivities of (a) the SPR and (b) the hybrid plasmonic-waveguide sensors over the visible spectrum of light. The values of the imaginary components used for all calculations are the measured values of [6]. Excluding $n_{1i} = 0.00011$, included to extrapolate the trend to even smaller levels of turbidity, the values used correspond to 1% skim milk to 33% heavy cream.

From figures 5.5 and 5.6, one can see that the sensitivity H_1 decreases with increasing turbidity. This is intuitive and can be explained due to the additional attenuation of the evanescent field in the medium as it interacts with the nanoparticle array. This results in less information concerning the changes in the bulk medium affecting the propagating, measured mode. When compared to the results of figure 5.4, it is evident the performance of the SPR sensor to detect changes in the imaginary component is significantly more reduced than that of the hybrid sensor, while the detection of changes in the real component is approximately reduced by an order of magnitude equally for both sensors.

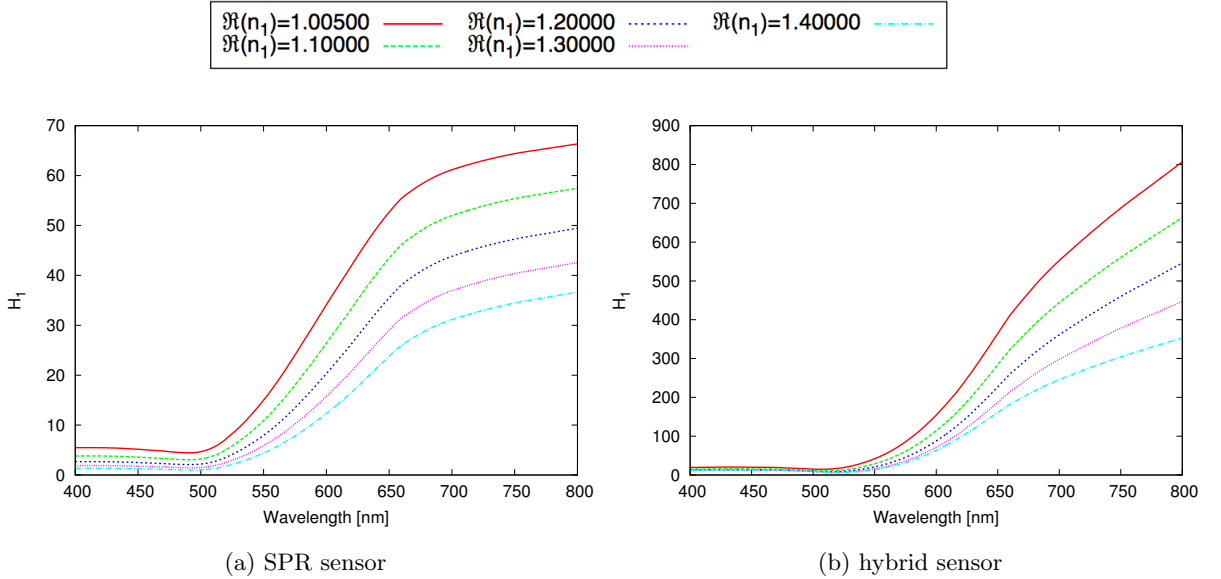


Figure 5.5: H_1 results for a varying $\Re(n_1)$ with the imaginary component held fixed at $\Im(n_1) = 0.00618$ for (a) the SPR sensor and (b) the hybrid sensor. For the hybrid sensor, particles have a radius of 5 nm and are separated by an interparticle spacing of 25 nm.

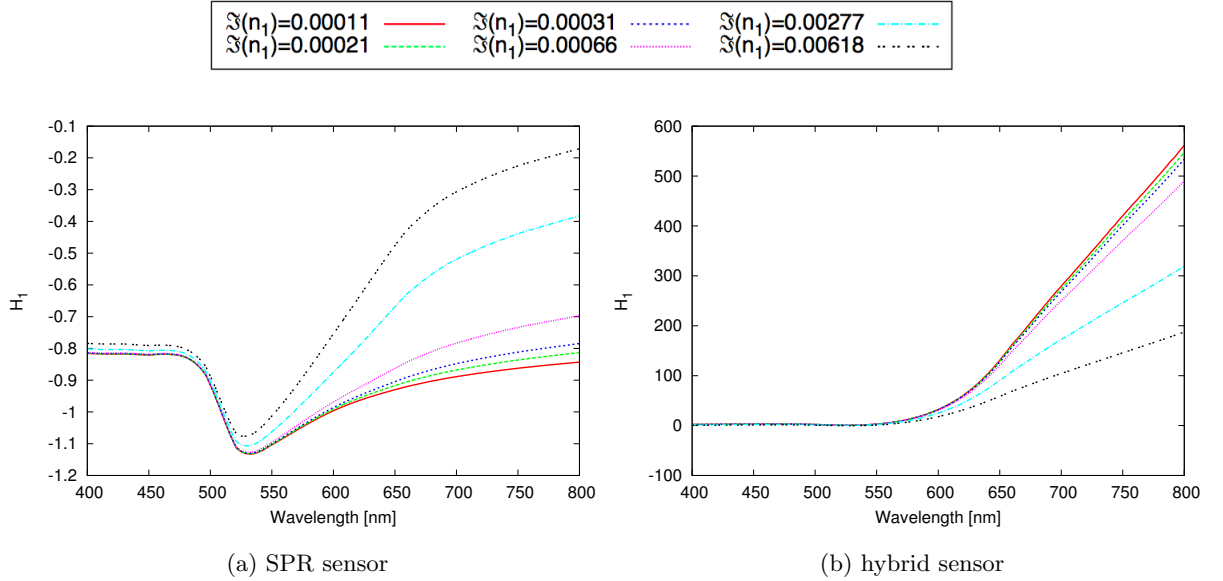


Figure 5.6: H_1 results for a varying $\Im(n_1)$ with the real component held fixed at $\Re(n_1) = 1.36$ for (a) the SPR sensor and (b) the hybrid sensor. For the hybrid sensor, particles have a radius of 5 nm and are separated by an interparticle spacing of 25 nm.

Comparing the subplots of figures 5.5 and 5.6 it is seen that the hybrid sensor improves over the SPR sensor by approximately three orders of magnitude for changes to the imaginary component of the refractive index, and one order of magnitude with regards to the real component. The negative values associated with figure 5.6(a) indicate changes in the real part of the propagation constant of the surface plasmon, κ_{SP} , decrease with changes in the bulk medium in the presence of turbidity. While the negative values associated with H_1 , provide additional information concerning the performance of the SPR system, in assessing the potential of the sensor, one should use the magnitude when comparing the various plots within figure 5.6(a). Thus, despite the appearance of the curves, it is important to note that the sensitivity of the SPR sensor decreases with increasing turbidity. It should be noted that the results of figure 5.5 are for p-polarized light. Similar results were obtained for s-polarized light, but have been omitted for the sake of brevity.

Chapter 6

Discussion and Conclusions

In this chapter, the results of the last three chapters will be discussed along with their implication regarding the potential performance of the hybrid sensor. The original contributions of the author will be also be highlighted. Finally, conclusions will be drawn and the limitations of this work will then be discussed in the context of future work at the end of the chapter.

6.1 Discussion of the Results

From the results of figure 3.3, the imaginary component of the propagating waveguide mode κ' is seen to decay exponentially to zero. This is in perfect conceptual agreement with the expressions involving the thickness of the finite layer, denoted D_2 , found in chapters 3 and 4. With regards to sensor performance, it is again observed from figure 3.3 that accompanying the loss of the imaginary component is the transition of $\kappa' \rightarrow \kappa$. This result shows all information acquired from interactions of the selvedge and the analyte are lost for large thickness of the finite layer. However, as the purpose of such a layer is to tether the nanoparticles to the waveguide structure, typical thicknesses range from 1 nm — 3 nm [92–95]. The decay experienced by the waveguide mode over this range of values is negligible. It is therefore concluded that there would be no appreciable difference in the

performance of the hybrid sensor due to the technique used to deposit the nanoparticle array.

The results of Calhoun *et. al.* [6] reported a consistent discrepancy between their reflectometry measurements and the SPR measurements of [35] of approximately 10%. This was likened to measurement limitation due to the limited ability of the apparatus used in [35] to measure the angle associated with SPR. Interestingly, reflectometric measurements between the two papers increasingly diverged with increasing turbidity. This suggests the hybrid sensor could compete with the reflectometry measurements for a turbid medium. Given the increased sensitivity of the hybrid sensor, it is conceivable that it would improve upon the 10% discrepancy and compete with or surpass the measurements of [6]. An additional promising result is how little the performance of the hybrid sensor is reduced with respect to the SPR sensor. In going from the transparent results of figure 5.4 to the results for turbid media in 5.5 or 5.6, one can see that the SPR sensor's performance is reduced by approximately 99.7%. However, the performance of the hybrid sensor is only reduced by approximately 72%.

The remaining discussion concerns the optimal configuration of the nanoparticle array. This is due to presence of noise in the calculations, as can be seen to some extent in figure 5.3. All derivatives were performed using a central difference numerical approach with a perturbation of $h=0.0001$, which resulted in a round-off error of approximately ± 0.01 for the second derivatives. The resultant noise consequently created certain patches in which the size and spacing eigenvalues are of opposite sign and the optimal solution is, in reality, a minimum. As a result of this, the optimal solutions presented in this work should be taken to be qualitative. A more accurate differentiation should be considered for future work.

6.2 Summary of Original Contributions

Within this work, original contributions of the author include:

- a comparison with the Green function approach of [43, 79] and the method of images was made

- an extension of the formalism of [43] for the presence of a finite layer between the nanoparticle system and the guiding layer
- an extension of [43] to include the imaginary component of the cladding medium, and by association the study of the effects of turbidity
- an eigenvalue analysis of the hybrid sensor to determine the optimal configuration
- a study of response of both sensing platforms to changes in the real and imaginary components of n_1 with both components held constant and carried separately.

Additionally, the following conference presentations focusing on portions of this work were presented, by the author:

- Travo D. A., Rangan C., Sipe J. E., (January 19, 2013) *Effects of a Tethering Layer on a Hybrid Gold Nanoparticle-Waveguide Biosensor* NSERC Strategic Network on Bioplasmonic Systems, All Network Meeting 9.
- Travo D. A., Rangan C., Sipe J. E., Cheng T. (November 17, 2012) *A Hybrid Biosensor Design For The Sensitive Detection Of Leukemia Biomarkers* 1st Annual Windsor Cancer Research Group Conference.
- Coughlan C., Travo D. A., Rangan C., Ertorer E., Mittler S. (November 17, 2012) *2D Gold Nanoparticle Biosensors For Leukemia Detection* Windsor Cancer Research Group Conference.
- Travo D. A., Rangan C. (October 11, 2012) *Green Function Analysis of Gold-Nanoparticles-on-a-Planar-Waveguide Biosensor Platform* 3rd Annual Nano Ontario Conference.

In addition to the contributions made within this work and to its presentation, the author was the lead author of [92], on an topic related to this thesis, focusing on the use of nanoplasmonics in biomedical applications. A manuscript summarizing these results is also in preparation.

6.3 Conclusions

In this work it has been shown that a hybrid plasmonic-waveguide biosensor, composed of a periodic array of nanoparticles is more sensitive than SPR based sensors to changes in the surrounding dielectric environment for both transparent and turbid media. In addition to this, it was shown that the bulk sensitivity of the hybrid sensor is dependent on the nanoparticle configuration, and that the size of the particles is the dominant factor in affecting the sensitivity of the system.

6.4 Future Work

The results of this work point to many possible directions for future work. The first is the inclusion of Eq. 1.1, which incorporates the angular dependence of the imaginary component of the refractive index. The explicit nature of this dependence was ignored in the current work presented. This was justified through our use of experimentally measured values and the sensitivity analysis conducted to assess the performance of the sensor in detecting changes in them. However, the angular dependence of our propagation constant κ can be seen through its definition as the projection of the propagating wave vector into the x-y cartesian plane, and is calculated in the guiding layer of the system. In this context, one can express κ as $\kappa = \tilde{\omega}n_3 \sin \theta$. The angle θ is defined as the angle of incidence with respect to the normal of interface between adjacent interfaces, and $\tilde{\omega}$ and n_3 are the magnitude of the wave vector in vacuum and the refractive index of the guiding layer as previously defined. The changes in the system due to changes in κ can thus be attributed to either changes in the wavelength of incident light or the angle of incidence. This essentially creates two domains within which the device can be operated. The first is the spectral domain, corresponding to changes in wavelength, and the second is the angular domain, corresponding to changes in the angle of incident light. The results presented in this work can be considered valid in the spectral domain.

However, if there is any angular dependence present, additional terms will appear in the derivatives of r_{12} with respect to κ . These terms will be associated with the effective

distances derived in chapters 3 and 4.

$$\frac{\partial n_{1i}}{\partial \kappa} \neq 0.$$

Thus, to completely assess the performance of the hybrid sensor, its sensitivity in the angular domain should be examined.

In addition to a modification of n_{1i} , a more robust treatment of the nanoparticle array is required to study the effects of the shape of the nanoparticles on the performance of the sensor. As these configurations cannot be studied analytically, more rigorous numerical treatments, such as discrete dipole algorithms are needed [74, 75, 92, 99–102].

Additionally, as the results of this work suggest increased sensitivities with smaller particles and increased spacings, an extension of the model to reach beyond the limitations of this work should be considered. This would include larger interparticle spacings should be made and smaller particle sizes. In its current implementation, if the spacing between particles increases such that the approximations made are invalid, our model will not reproduce interference effects, such as sharp resonances and Wood’s anomaly that will have to be taken into consideration [101, 103–105].

Appendix A

Integrals Involving Angular Dependence and Bessel Functions

This appendix is devoted to solving the integrals of Eq. 3.5,

$$\mathbf{E}(\mathbf{R}, z) = \frac{1}{8\pi^2 \varepsilon_0 \varepsilon_1} \int_0^\infty \kappa^2 R_{13} e^{-\kappa(z+z')} \int_0^{2\pi} e^{i\kappa R \cos \phi} \mathbf{O} \cdot \boldsymbol{\mu} d\phi d\kappa. \quad (\text{A.1})$$

The angular dependence of the integrals will be evaluated in the first half and the integral of κ will be determined at the end of this appendix. Expanding Eq. A.1 using Eq. 3.4, the ϕ -dependence is explicitly seen as

$$\begin{aligned} \int_0^{2\pi} e^{i\kappa R \cos \phi} \mathbf{O} \cdot \boldsymbol{\mu} d\phi &= \int_0^{2\pi} e^{i\kappa R \cos \phi} [\hat{z}\hat{z} + \hat{x}\hat{x} \cos^2(\phi + \theta) + \hat{y}\hat{y} \sin^2(\phi + \theta) \\ &\quad + (\hat{x}\hat{y} + \hat{y}\hat{x}) \cos(\phi + \theta) \sin(\phi + \theta) + i(\hat{z}\hat{x} \cos(\phi + \theta) + \hat{z}\hat{y} \sin(\phi + \theta)) \\ &\quad - i(\hat{x}\hat{z} \cos(\phi + \theta) + \hat{y}\hat{z} \sin(\phi + \theta)) \cdot \boldsymbol{\mu}] d\phi. \end{aligned} \quad (\text{A.2})$$

To isolate the dependence on ϕ of Eq. A.2, we will recast the trigonometric functions in terms of complex exponentials using Euler's formula, $e^{i\psi} = \cos \psi + i \sin \psi$. This results in the well known expressions

$$\begin{aligned} \cos(\psi) &= \frac{e^{i\psi} + e^{-i\psi}}{2}, \text{ and} \\ \sin(\psi) &= \frac{e^{i\psi} - e^{-i\psi}}{2i}. \end{aligned}$$

In addition to this, from figure 3.1, one can see that the angle θ can be expressed in Cartesian coordinates. Using Euler's formula, this results in a relation to eliminate $e^{i\theta}$ from the derived expressions. Accordingly, we see that

$$\theta = \tan^{-1}(y/x),$$

such that

$$\begin{aligned} e^{i\theta} &= \cos(\tan^{-1}(y/x)) + i \sin(\tan^{-1}(y/x)) \\ &= \frac{x + iy}{\sqrt{x^2 + y^2}}, \end{aligned}$$

and

$$\begin{aligned} e^{i2\theta} &= e^{i\theta} e^{i\theta} \\ &= \left(\frac{x + iy}{\sqrt{x^2 + y^2}} \right) \left(\frac{x + iy}{\sqrt{x^2 + y^2}} \right) \\ &= \frac{x^2 - y^2 + 2ixy}{x^2 + y^2}. \end{aligned}$$

Evaluating at a given value of $\mathbf{R} = (x, y)$, the angular dependence of Eq. A.2 will then result in integrals of the form

$$\int_0^{2\pi} e^{iz \cos \phi} e^{in\phi} d\phi = 2\pi i^n J_n(z), \quad (\text{A.3})$$

where $J_n(z)$ is the n th order Bessel function of the first kind (Eq. 71 from [106]).

Using the above relations, the integrals of Eq. A.2 can now be determined. The individual terms are then evaluated as follows:

$$\int_0^{2\pi} e^{i\kappa R \cos \phi} d\phi = 2\pi J_0(\kappa R), \quad (\text{A.4})$$

$$\begin{aligned}
 \int_0^{2\pi} e^{i\kappa R \cos \phi} \cos(\phi + \theta) d\phi &= \int_0^{2\pi} e^{i\kappa R \cos \phi} \left(\frac{1}{2} \right) \left(e^{i(\phi+\theta)} + e^{-i(\phi+\theta)} \right) d\phi \\
 &= \frac{1}{2} \int_0^{2\pi} e^{i\kappa R \cos \phi} \left(e^{i\phi} e^{i\theta} + e^{-i\phi} e^{-i\theta} \right) d\phi \\
 &= \frac{1}{2} \left[2\pi i J_1(\kappa R) e^{i\theta} + 2\pi i^{-1} J_{-1}(\kappa R) e^{-i\theta} \right] \\
 &= i\pi J_1(\kappa R) \left[e^{i\theta} + e^{-i\theta} \right] \\
 &= i\pi J_1(\kappa R) \left[\frac{x + iy}{\sqrt{x^2 + y^2}} + \frac{x - iy}{\sqrt{x^2 - y^2}} \right] \\
 &= 2\pi i J_1(\kappa R) \frac{x}{\sqrt{x^2 + y^2}}, \tag{A.5}
 \end{aligned}$$

$$\begin{aligned}
 \int_0^{2\pi} e^{i\kappa R \cos \phi} \sin(\phi + \theta) d\phi &= \int_0^{2\pi} e^{i\kappa R \cos \phi} \left(\frac{1}{2i} \right) \left(e^{i(\phi+\theta)} - e^{-i(\phi+\theta)} \right) d\phi \\
 &= \frac{1}{2i} \int_0^{2\pi} e^{i\kappa R \cos \phi} \left(e^{i\phi} e^{i\theta} - e^{-i\phi} e^{-i\theta} \right) d\phi \\
 &= \frac{1}{2i} \left[2\pi i J_1(\kappa R) e^{i\theta} - 2\pi i^{-1} J_{-1}(\kappa R) e^{-i\theta} \right] \\
 &= \pi J_1(\kappa R) \left[e^{i\theta} - e^{-i\theta} \right] \\
 &= \pi J_1(\kappa R) \left[\frac{x + iy}{\sqrt{x^2 + y^2}} - \frac{x - iy}{\sqrt{x^2 - y^2}} \right] \\
 &= 2\pi i J_1(\kappa R) \frac{y}{\sqrt{x^2 + y^2}}, \tag{A.6}
 \end{aligned}$$

$$\begin{aligned}
 \int_0^{2\pi} e^{i\kappa R \cos \phi} \cos(\phi + \theta) \sin(\phi + \theta) d\phi &= \frac{1}{2} \int_0^{2\pi} e^{i\kappa R \cos \phi} \sin 2(\phi + \theta) d\phi \\
 &= \frac{1}{2} \int_0^{2\pi} e^{i\kappa R \cos \phi} \left(\frac{1}{2i} \right) \left(e^{i2(\phi+\theta)} - e^{-i2(\phi+\theta)} \right) d\phi \\
 &= \frac{1}{4i} \int_0^{2\pi} e^{i\kappa R \cos \phi} \left(e^{i2\phi} e^{i2\theta} - e^{-i2\phi} e^{-i2\theta} \right) d\phi \\
 &= \frac{1}{4i} \left[2\pi i^2 J_2(\kappa R) e^{i2\theta} - 2\pi i^{-2} J_{-2}(\kappa R) e^{-i2\theta} \right] \\
 &= \frac{\pi J_2(\kappa R)}{2i} \left[-e^{i2\theta} + e^{-i2\theta} \right] \\
 &= \frac{\pi J_2(\kappa R)}{2i} \left[-\frac{x^2 - y^2 + 2ixy}{x^2 + y^2} + \frac{x^2 - y^2 - 2ixy}{x^2 + y^2} \right] \\
 &= -2\pi J_2(\kappa R) \frac{xy}{x^2 + y^2}, \tag{A.7}
 \end{aligned}$$

$$\begin{aligned}
 \int_0^{2\pi} e^{i\kappa R \cos \phi} \cos^2(\phi + \theta) d\phi &= \int_0^{2\pi} e^{i\kappa R \cos \phi} \left(\frac{1}{2} \right)^2 \left(e^{i(\phi+\theta)} + e^{-i(\phi+\theta)} \right)^2 d\phi \\
 &= \frac{1}{4} \int_0^{2\pi} e^{i\kappa R \cos \phi} \left(e^{i2(\phi+\theta)} + e^{-i2(\phi+\theta)} + 2 \right) d\phi \\
 &= \frac{1}{4} \left[2\pi i^2 J_2(\kappa R) e^{i2\theta} + 2\pi i^{-2} J_{-2}(\kappa R) e^{-i2\theta} + 2(2\pi i^0 J_0(\kappa R)) \right] \\
 &= \frac{\pi}{2} \left[-J_2(\kappa R) \left(e^{i2\theta} + e^{-i2\theta} \right) + 2J_0(\kappa R) \right] \\
 &= \frac{\pi}{2} \left[-J_2(\kappa R) \left(\frac{x^2 - y^2 + 2ixy}{x^2 + y^2} + \frac{x^2 - y^2 - 2ixy}{x^2 + y^2} \right) + 2J_0(\kappa R) \right] \\
 &= \frac{\pi}{2} \left[-2J_2(\kappa R) \frac{x^2 - y^2}{x^2 + y^2} + 2J_0(\kappa R) \right] \\
 &= \pi \left[J_0(\kappa R) - J_2(\kappa R) \frac{x^2 - y^2}{x^2 + y^2} \right], \tag{A.8}
 \end{aligned}$$

$$\begin{aligned}
 \int_0^{2\pi} e^{i\kappa R \cos \phi} \sin^2(\phi + \theta) d\phi &= \int_0^{2\pi} e^{i\kappa R \cos \phi} \left(\frac{1}{2i} \right)^2 \left(e^{i(\phi+\theta)} - e^{-i(\phi+\theta)} \right)^2 d\phi \\
 &= \frac{-1}{4} \int_0^{2\pi} e^{i\kappa R \cos \phi} \left(e^{i2(\phi+\theta)} + e^{-i2(\phi+\theta)} - 2 \right) d\phi \\
 &= \frac{-1}{4} \left[2\pi i^2 J_2(\kappa R) e^{i2\theta} + 2\pi i^{-2} J_{-2}(\kappa R) e^{-i2\theta} - 2(2\pi i^0 J_0(\kappa R)) \right] \\
 &= \frac{-\pi}{2} \left[-J_2(\kappa R) \left(e^{i2\theta} + e^{-i2\theta} \right) - 2J_0(\kappa R) \right] \\
 &= \frac{-\pi}{2} \left[-J_2(\kappa R) \left(\frac{x^2 - y^2 + 2ixy}{x^2 + y^2} + \frac{x^2 - y^2 - 2ixy}{x^2 + y^2} \right) - 2J_0(\kappa R) \right] \\
 &= \frac{-\pi}{2} \left[-2J_2(\kappa R) \frac{x^2 - y^2}{x^2 + y^2} - 2J_0(\kappa R) \right] \\
 &= \pi \left[J_0(\kappa R) + J_2(\kappa R) \frac{x^2 - y^2}{x^2 + y^2} \right]. \tag{A.9}
 \end{aligned}$$

With the integration over ϕ complete, we can now turn to the integration over κ . This will be performed using Eq. 6.621 of [107],

$$\int_0^\infty x^{m+1} e^{-\alpha x} J_\nu(\beta x) dx = (-1)^{m+1} \beta^{-\nu} \frac{\partial^{m+1}}{\partial \alpha^{m+1}} \left(\frac{\left(\sqrt{\alpha^2 + \beta^2} - \alpha \right)^\nu}{\sqrt{\alpha^2 + \beta^2}} \right). \tag{A.10}$$

(valid for $\beta > 0$, $\Re(\nu) > -m - 2$). This leads to the following results:

$$\begin{aligned}
 \int_0^\infty \kappa^2 e^{-\kappa(z+z'+2nD_2)} J_0(\kappa R) d\kappa &= \frac{3(z+z'+2nD_2)^2}{(R^2 + (z+z'+2nD_2)^2)^{5/2}} - \frac{1}{(R^2 + (z+z'+2nD_2)^2)^{3/2}} \\
 &= \frac{2(z+z'+2nD_2)^2 - R^2}{[R^2 + (z+z'+2nD_2)^2]^{5/2}}, \tag{A.11}
 \end{aligned}$$

$$\begin{aligned}
 \int_0^\infty \kappa^2 e^{-\kappa(z+z'+2nD_2)} J_1(\kappa R) d\kappa &= R^{-1} \frac{3(z+z'+2nD_2)R^2}{[R^2 + (z+z'+2nD_2)^2]^{5/2}} \\
 &= \frac{3(z+z'+2nD_2)R}{[R^2 + (z+z'+2nD_2)^2]^{5/2}}, \tag{A.12}
 \end{aligned}$$

$$\begin{aligned}
 \int_0^\infty \kappa^2 e^{-\kappa(z+z'+2nD_2)} J_2(\kappa R) d\kappa &= R^{-2} \frac{3R^4}{[R^2 + (z+z'+2nD_2)^2]^{5/2}} \\
 &= \frac{3R^2}{[R^2 + (z+z'+2nD_2)^2]^{5/2}}, \tag{A.13}
 \end{aligned}$$

and similarly,

$$\int_0^\infty \kappa^2 e^{-\kappa(z+z'+2(n+1)D_2)} J_0(\kappa R) d\kappa = \frac{2(z+z'+2(n+1)D_2)^2 - R^2}{[R^2 + (z+z'+2(n+1)D_2)^2]^{5/2}}, \quad (\text{A.14})$$

$$\int_0^\infty \kappa^2 e^{-\kappa(z+z'+2(n+1)D_2)} J_1(\kappa R) d\kappa = \frac{3(z+z'+2(n+1)D_2)R}{[R^2 + (z+z'+2(n+1)D_2)^2]^{5/2}}, \quad (\text{A.15})$$

$$\int_0^\infty \kappa^2 e^{-\kappa(z+z'+2(n+1)D_2)} J_2(\kappa R) d\kappa = \frac{3R^2}{[R^2 + (z+z'+2(n+1)D_2)^2]^{5/2}}. \quad (\text{A.16})$$

Appendix B

List Green Functions

This appendix will contain the various Green functions used in the initial formalism of chapter 2 and [43]. All notation used is as defined in the preceding chapters. In summary, \mathbf{U} is the unit dyadic, $\mathbf{r} = (\mathbf{R} - \mathbf{R}', z, z')$, and $\mathbf{R} = (x, y)$ are Cartesian components. Additionally, $\tilde{\omega} = \omega/c$ and is the wave vector of an incident wave in free space, κ is the projection of the wave vector within a medium onto the Cartesian x-y plane and ε_1 is the dielectric constant of the cladding medium. With all the necessary variables defined, the functions are:

- G^o , the full Green function in the absence of a multilayer structure, (real space)

$$4\pi\epsilon_0 G^o(\mathbf{r}) = \frac{3\hat{\mathbf{r}}\hat{\mathbf{r}} - \mathbf{U}}{\varepsilon_1} \left(\frac{e^{i\tilde{\omega}n_1 r}}{r^3} - \frac{i\tilde{\omega}n_1 e^{i\tilde{\omega}n_1 r}}{r^2} \right) + \frac{\tilde{\omega}^2 (\mathbf{U} - \hat{\mathbf{r}}\hat{\mathbf{r}}) e^{i\tilde{\omega}n_1 r}}{r} - \frac{4\pi}{3\varepsilon_1} \delta(\mathbf{r}) \mathbf{U}, \quad (\text{B.1})$$

- G^o , the full Green function in the absence of a multilayer structure, (reciprocal space)

$$G^o(\kappa; z, z') = \frac{i\tilde{\omega}^2}{2\epsilon_0 w_1} (\hat{\mathbf{s}}\hat{\mathbf{s}} + \hat{\mathbf{p}}_{1+}\hat{\mathbf{p}}_{1+}) \theta(z - z') e^{i w_1(z - z')} + \frac{i\tilde{\omega}^2}{2\epsilon_0 w_1} (\hat{\mathbf{s}}\hat{\mathbf{s}} + \hat{\mathbf{p}}_{1-}\hat{\mathbf{p}}_{1-}) \theta(z' - z) e^{i w_1(z' - z)} - \frac{\hat{\mathbf{z}}\hat{\mathbf{z}}}{\epsilon_0 \varepsilon_1} \delta(z - z'), \quad (\text{B.2})$$

- G_T^o identifies the transverse component of the field

$$G_T^o(\kappa; z, z') \equiv G^o(\kappa; z, z') - G_L^o(\kappa; z, z') \quad (\text{B.3})$$

- G_L^o extracts the longitudinal component (real space)

$$G_L^o(\mathbf{r}) = \frac{1}{4\pi\epsilon_0\epsilon_1} \left(\frac{3\hat{r}\hat{r} - \mathbf{U}}{r^3} \right) - \frac{4\pi}{3} \delta(\mathbf{r}) \mathbf{U}. \quad (\text{B.4})$$

Expanding Eq. B.4, we see that at all points excluding $z = z'$,

$$\begin{aligned} G_L^o(\mathbf{r}) &= \frac{1}{4\pi\epsilon_0\epsilon_1} \left(\frac{3\hat{r}\hat{r} - \mathbf{U}}{r^3} \right) \\ &= \frac{1}{4\pi\epsilon_0\epsilon_1} \left(\frac{3\mathbf{r}\mathbf{r} - \mathbf{U}r^2}{r^5} \right) \\ G_L^o(\mathbf{r}) &= \frac{1}{4\pi\epsilon_0\epsilon_1} \frac{1}{[R^2 + (z - z')^2]^{5/2}} \left\{ (-\hat{x}\hat{x} - \hat{y}\hat{y} + 2\hat{z}\hat{z})(z - z')^2 \right. \\ &\quad + 3(z - z') [(\hat{x}\hat{z} + \hat{z}\hat{x})x + (\hat{y}\hat{z} + \hat{z}\hat{y})y] + (x^2 + y^2) \left(\frac{1}{2}\hat{x}\hat{x} + \frac{1}{2}\hat{y}\hat{y} - \hat{z}\hat{z} \right) \\ &\quad \left. + \frac{3}{2} [(x^2 - y^2)(\hat{x}\hat{x} - \hat{y}\hat{y}) + 2xy(\hat{x}\hat{y} + \hat{y}\hat{x})] \right\}, \end{aligned} \quad (\text{B.5})$$

which will be a useful form of the function to be used in chapter 3.

- G_L^o extracts the longitudinal component (reciprocal space)

$$\begin{aligned} G_L^o(\kappa, z, z') &= \frac{\kappa}{2\epsilon_0\epsilon_1} (\hat{z}\hat{z} - \hat{\kappa}\hat{\kappa} - i\hat{z}\hat{\kappa} - i\hat{\kappa}\hat{z}) \theta(z - z') e^{-\kappa(z - z')} \\ &\quad + \frac{\kappa}{2\epsilon_0\epsilon_1} (\hat{z}\hat{z} - \hat{\kappa}\hat{\kappa} + i\hat{z}\hat{\kappa} + i\hat{\kappa}\hat{z}) \theta(z' - z) e^{-\kappa(z - z')} \\ &\quad - \frac{\hat{z}\hat{z}}{\epsilon_0\epsilon_1} \delta(z - z') \end{aligned} \quad (\text{B.6})$$

- G^R , the full Green function to correct for the multilayer structure, (reciprocal space)

$$G^R(\kappa; z, z') = \frac{i\tilde{\omega}^2}{2\epsilon_0\omega_1} (\hat{\mathbf{s}}R_{1N}^s\hat{\mathbf{s}} + \hat{\mathbf{p}}_{1+}R_{1N}^p\hat{\mathbf{p}}_{1-}) e^{i\omega_1(z + z')}, \quad (\text{B.7})$$

- G_I^R , the electrostatic Green function to correct for the multilayer structure, (reciprocal space)

$$G_I^R(\kappa; z, z') = \frac{\kappa}{2\epsilon_0\epsilon_1} \frac{\epsilon_2 - \epsilon_1}{\epsilon_2 + \epsilon_1} (\hat{\mathbf{z}}\hat{\mathbf{z}} + \hat{\kappa}\hat{\kappa} + i\hat{\mathbf{z}}\hat{\kappa} - i\hat{\kappa}\hat{\mathbf{z}}) e^{-\kappa(z + z')} \quad (\text{B.8})$$

- G_C^R , provides additional corrections to the electrostatic Green function such that,
(reciprocal space)

$$\begin{aligned}
 & G_C^R(\kappa; z, z') \\
 = & \frac{i\tilde{\omega}^2}{2\epsilon_0 w_1} (\hat{\mathbf{s}} R_{1N}^s \hat{\mathbf{s}} + \hat{\mathbf{p}}_{1+} R_{1N}^p \hat{\mathbf{p}}_{1-}) e^{i w_1(z+z')} \\
 & - \frac{\kappa}{2\epsilon_0 \epsilon_1} \frac{\epsilon_2 - \epsilon_1}{\epsilon_2 + \epsilon_1} (\hat{\mathbf{z}} \hat{\mathbf{z}} + \hat{\kappa} \hat{\kappa} + i \hat{\mathbf{z}} \hat{\kappa} - i \hat{\kappa} \hat{\mathbf{z}}) e^{-\kappa(z+z')},
 \end{aligned} \tag{B.9}$$

Appendix C

Codes

```
function [] =  
    wgsensor(mode,D2tmp,n1r,n1i,npc,n2,np3,np4,rad,rcad,d,sp,pol,set,path,plt,der2)  
%  
% Description:  
%  
% The function wgsensor.m accepts the user specified input parameters and  
% passed them on to the function turbid.m where the calculations to  
% determine the new resonant waveguide mode are performed. This function  
% also controls the numerical differntiation procedure and quadratic  
% programming elements. All outputs are written to data files of the form  
% of wgsense*****.dat, wgfit*****.dat and wgopt*****.dat, where '*****'  
% denotes specific titling by the input parameters.  
%  
% Input Parameters:  
%  
% mode    - determine whether analysis is for bulk (H) or bioconjugation  
%          (G) sensing  
% D2      - thickness of tethering layer
```

```
% n1(r/i) - real/imaginary component of top medium refractive index
% npc      - refractive index of nanoparticle shell
% n2       - refractive index of tethering layer
% np3      - refractive index of guiding layer
% np4      - refractive index of substrate
% rad      - radius of spherical particles
% rcad     - radius of particle core (if core/shell model used). Default
%           rcad=rad
% d        - height of particles above tethering layer (default set to rad)
% sp       - interparticle spacing
% pol      - polarization of incident electric field (s or p)
% set      - specifies if bulk sensing done WRT to real (r), imaginary (i),
%           or both (b) components of cladding refractive index
% path     - path to location output files will be written
% plt      - toggles whether matlab will generate a plot of the output data
%           (y/n)
% der2     - toggle to calculate second derivatives, do quadratic expansion
%           and solve QP minimization problem
```

```
global omegat kappa g e1 e2 e3 e4 D2 D3
```

```
ptdiff=3; % number of points to include in numerical differentiation
          % Options: 2 for forward - difference
          %           3 for central - difference
```

```
if real(e1) == 1
    ptdiff=2; % avoid anomalous dispersion ( e1 < 1 )
end
```

```
wave11=400;
wave12=800;
step=2;
```

```
sz=wavel2-wavel1+1;

%-----Initialize data arrays
%
shift(1:2)=0;
change(1:10)=0;
sense(1:sz,1:4)=0;
ab(1:10)=0;
mshift(1:10)=0;
fsense(1:sz,1:3)=0;
C(1:sz,1:3)=0;
H(1:sz,1:4)=0;
Eg(1:sz,1:3)=0;
x(1:sz,1:2)=0;
perm=importdata('diel.tab.jc');
%
%-----End initialization

fidsense=fopen(strcat(path,'wgsense_n1i',sprintf('%6.5f',n1i),'_r', ...
    sprintf('%6.5f',rad),'_a',sprintf('%6.5f',sp),'_pol',pol,'_diff',set,'.dat'),'w');
fidop=fopen(strcat(path,'wgop_n1i',sprintf('%6.5f',n1i),'_r', ...
    sprintf('%6.5f',rad),'_a',sprintf('%6.5f',sp),'_pol',pol,'_diff',set,'.dat'),'w');
fidfit=fopen(strcat(path,'wgfit_n1i',sprintf('%6.5f',n1i),'_r', ...
    sprintf('%6.5f',rad),'_a',sprintf('%6.5f',sp),'_pol',pol,'_diff',set,'.dat'),'w');

D2=D2tmp;
D3=3;

r=rad;
rc=rcad;

n1(1)=n1r;
```

```
n1(2)=n1i;

ep1=n1(1)^2 - n1(2)^2;
ep1i=2*n1(1)*n1(2);
e2=n2^2;

dif=0.0001;    % difference between particle size/spac used and expansion and
               % the actual input parameters.
del=0.000001; % for num. diff of GNPs size and spacing.

dele=10^floor(log10(ep1i))*1d-4; %for num. diff. of re(e1).

if iep1i > 0

    delei=10^floor(log10(ep1i))*1d-4; %for num. diff of im(e1).

else

    delei=dele;

end

if set == 'i'
    numdel=delei;
else
    numdel=dele;
end

w=0;

for k=wavel1:step:wavel2

    w=w+1;
```

```
alambda=k/1000;
omegat=2*pi/alambda;
eps=complex(perm(k-wave11+1,5),perm(k-wave11+1,6));

if np3 == 0 || np4 == 0
    e4=bk7(alambda);
    e3=(sqrt(e4)+0.01553)^2;
else
    e3=np3^2;
    e4=np4^2;
end

if D2 <= 0
    D2=0.;
    e2=e3;
    g=-1.;
else
    g=1.;
end

if mode == 'H'
    r=rc;
end

if d < r
    d=r; % Ensures particles are above surface
end

if der2=='y'
    num=10;
```

```
    sp=sp-dif;    % adjust parameters for series expansion
    rad=rad-dif;
    rcad=rad;

    a=sp;
    r=rad;
    rc=rcad;
else
    num=1;
    a=sp;
    r=rad;
    rc=rcad;
end

for m=1:num

    switch m
        case 1

        case 2
            a=sp+del;
            r=rad;
            rc=rcad;
        case 3
            a=sp-del;
            r=rad;
            rc=rcad;
        case 4
            a=sp;
            r=rad+del;
            rc=rcad+del;
        case 5
            a=sp;
```

```
        r=rad-del;
        rc=rcad-del;
    case 6
        a=sp+del;
        r=rad+del;
        rc=rcad+del;
    case 7
        a=sp+del;
        r=rad-del;
        rc=rcad-del;
    case 8
        a=sp-del;
        r=rad+del;
        rc=rcad+del;
    case 9
        a=sp-del;
        r=rad-del;
        rc=rcad-del;
    case 10
        sp=sp+dif;    % readjust back to initial point
        rad=rad+dif;
        rcad=rad;

        a=sp;
        r=rad;
        rc=rcad;
    otherwise
        fprintf('Mistake in Hessian matrix calculation!');
end

for j=1:ptdiff

    switch j
```

```
case 1
    e1=complex(ep1,ep1i);
    ec=npc^2;
case 2
    if mode == 'H'
        if set == 'r'
            e1=complex(ep1+dele,ep1i);
        else
            if set == 'i'
                e1=complex(ep1,ep1i+delei);
            else
                if set == 'b'
                    e1=complex(ep1+dele,ep1i+delei);
                else
                    fprintf('How are we differentiating?');
                end
            end
        end
    end

    ec=npc^2;

else

    e1=complex(ep1,ep1i);
    ec=npc^2+dele;

end

case 3
    if mode == 'H'
        if set == 'r'
            e1=complex(ep1-dele,ep1i);
        else
            if set == 'i'
```

```
        e1=complex(ep1,ep1i-delei);
    else
        if set == 'b'
            e1=complex(ep1-dele,ep1i-delei);
        else
            fprintf('How are we differentiating?');
        end
    end
end

ec=npc^2;

else

    e1=complex(ep1,ep1i);
    ec=npc^2-dele;

end

otherwise

    fprintf('Error in differentiation');

end

shift(j)=turbid2(eps,ec,r,rc,d,a,pol);

end

if j == 3
    change(m)=real(shift(2)-shift(3))/(2*numdel*imag(shift(1)));
else
    change(m)=real(shift(2)-shift(1))/(numdel*imag(shift(1)));
end
```

```
    ab(m)=2*imag(shift(1));
    mshift(m)=real(shift(1)) - kappa;

end

sense(w,1)=k;
sense(w,2)=change(num); % change with real part of e1
sense(w,3)=ab(num);      % absorption calcs
sense(w,4)=mshift(num); % mode shift calcs

if der2=='y'

% Calculate elements of Hessian matrix

H(w,1)=(change(2)-2*change(1)+change(3))/(del^2); % second WRT "a"
H(w,2)=(change(6)-change(7)-change(8)+change(9))/(4*del^2); % mixed term
H(w,3)=H(w,2); % mixed term
H(w,4)=(change(4)-2*change(1)+change(5))/(del^2); % second WRT "r"

% Calculate first derivatives WRT size and spacing
C(w,1)=k;
C(w,2)=(change(2)-change(3))/(2*del); % spacing
C(w,3)=(change(4)-change(5))/(2*del); % size

% Quadratic approximation to sensing figure or merit
fsense(w,1)=k;
fsense(w,2)=change(1) + C(w,2:3)*[dif;dif] ...
    + 0.5*[dif,dif]*[H(w,1:2);H(w,3:4)]*[dif;dif];
```

```
A=eig([H(w,1:2);H(w,3:4)]);

Eg(w,1)=k;
Eg(w,2)=A(1); % spacing eig.
Eg(w,3)=A(2); % size eig.

A2=[-1,2;1,0;0,1;0,-1];
b2=[-1;50;10;-5]/1000;

% x(k,1:2)=convexQP(-[C(w,2);C(w,3)],-[H(w,1:2);H(w,3:4)], ...
% 0,0,A2,b2,'dump.txt',0);

xtmp=quadprog([H(w,1:2);H(w,3:4)], [C(w,2);C(w,3)],A2,b2);

x(k,1)=xtmp(1);
x(k,2)=xtmp(2);

fprintf(fidop,'%i\t%7.6g\t%7.6g\t%7.6g\t%7.6g\n',k,A(1),A(2),x(w,1),x(w,2));

fprintf(fidfit,'%i\t%7.6g\t%7.6g\t%7.6g\t%7.6g\t%7.6g\t%7.6g\t%7.6g\n',k, ...
C(w,2),C(w,3),H(w,1),H(w,2),H(w,3),H(w,4),fsense(w,2));

end

fprintf(fidsense,'%i\t%7.6g\t%7.6g\t%7.6g\n',k,change(num),ab(num),mshift(num));

end

fclose(fidsense);
fclose(fidop);
```

```
fclose(fidfit);

if plt=='y'
% Generate plot of sensing and optimization results

    plot(sense(1:end,1),x(1:end,1),sense(1:end,1),x(1:end,2))
    legend('spac opt.','size opt.','Location','NorthWest')
    ylabel('Opt. Sols [nm]')
    subplot(2,3,6)

    plot(Eg(1:end,1),Eg(1:end,2),Eg(1:end,1),Eg(1:end,3))
    legend('spacing','size','Location','SouthWest')
    ylabel('Eigs.')
    subplot(2,3,1)

    plot(sense(1:end,1),sense(1:end,3))
    ylabel('Abs.')
    subplot(2,3,3)

    plot(sense(1:end,1),sense(1:end,2))
    ylabel('FoM: H')
    subplot(2,3,2);

    plot(sense(1:end,1),sense(1:end,4))
    ylabel('Mode Shift')
    subplot(2,3,4)

    plot(sense(1:end,1),sense(1:end,2),fsense(1:end,1),fsense(1:end,2))
    legend('Actual','Quad.','Location','NorthWest')
    ylabel('FoM: H')
    subplot(2,3,5)

end
```

end

```
function [ shift ] = turbid(eps,ec,r,rc,d,a,pol)
%
% Description:
%
% The function turbid.m calculates the resonant waveguide mode for the bare
% multilayer structure and the shift to the new mode due to the presence of
% the selvedge.
%
% Input parameters:
%
% eps - dielectric data for selvedge
% ec - ec dielectric data for particle coating
% r - outer radius of particles
% rc - core radius of particles
% d - height of particles above multilayer structure
% a - interparticle spacing between particles (centre - to - centre)
% pol - polarization of incident light (s or p)
%
% Output parameters:
%
% shift - new waveguide mode due to presence of selvedge
```

```
global omegat kappa g e1 e2 e3 e4 D2 D3
```

```
ac=9.03;
```

```
epsav=ec*(1+2*(rc/r)^3*(eps-ec)/(eps+2*ec))/(1-(rc/r)^3*(eps-ec)/(eps+2*ec));
```

```
dc=bd(d,a);
```

```
aa=pi/D3*(0.00001);
bb1=omegat*sqrt(e3-e4)*0.99999;
bb2=pi/D3*(0.99999);
bb=min(bb1,bb2);

if bb < aa
    fprintf('Error with mode solution');
end

epsi=1d-10;
delta=1d-10/(bb-aa);
M=100;

%-----determine kappa for bare multilayer structure

h=bisect(aa,bb,pol,epsi,delta,M);

kappa=sqrt(e3*omegat^2-h^2);

%-----kappa has been found

if pol == 's'

    aq=1;
    ap=1;
    au=1;

else

    aq=e3/e1;
    ap=e3/e4;
    au=e3/e2;
```

```
end

beta=-imag(aq*sqrt((e3-e1)*omegat^2-h^2));

if beta <= 0d-32
    beta=1d-32; % avoid division by zero
end

q=real(aq*sqrt((e3-e1)*omegat^2-h^2));
p=ap*sqrt((e3-e4)*omegat^2-h^2);

u=g*au*sqrt((e3-e2)*omegat^2-h^2);

corr=sign(omegat^2*real(e1)-kappa^2);

deff2=(ap^2*h^2+p^2)/(h^2+p^2)/p;

f1=sqrt(kappa^2-omegat^2*real(e1) ...
    -corr*sqrt((omegat^2*real(e1)-kappa^2)^2+(omegat^2*imag(e1))^2))/sqrt(2);

f2=sqrt(omegat^2*real(e1) - kappa^2 ...
    -corr*sqrt((omegat^2*real(e1)-kappa^2)^2+(omegat^2*imag(e1))^2))/sqrt(2);

if f2 <= 1d-32
    f2=1d-32;
end
```

```
ar=real(aq);
ai=imag(aq);

gam=corr*(omegat^2*real(e1)-kappa^2)/ ...
      sqrt((omegat^2*real(e1)-kappa^2)^2+omegat^4*imag(e1)^2);

turbr1=1i*h/((beta+1i*q)^2+u^2)*(au^2/u*(q-1i*beta) ...
-
      u/2*(1i*ai*sign(omegat^2*imag(e1))+ar)*(1+gam)/f1+(ai-1i*ar*sign(omegat^2*imag(e1)))*

if D2==0
    perb=1d-32*(1+1i);
else
    perb=0;
end

D23eff=D3-1i*au^2*h*D2/u+deff2 + turbr1;
D3eff=D3+deff2+(au^2*h^2+u^2)/(h^2+u^2+perb)/u;
D2eff=-1i*au^2*h*D2/u + turbr1 +(au^2*h^2+u^2)/(h^2+u^2+perb)/u;

r12=(beta+1i*(q-u))/(beta+1i*(q+u));
r32=(h-1i*u)/(h+1i*u);
r34=(h-1i*p)/(h+1i*p);

rnum=h*(r12^2-1.)*(r32-r34*exp(2*1i*h*D3));
rdenom=2*1i*kappa*(r12*r32*D2eff ...
      + r32*r34*D3eff*exp(2*1i*h*D3+2*u*D2) ...
      - r12*r34*D23eff*exp(2*1i*h*D3));
```

```
rho13=rnum/rdenom;

w1=sqrt(e1*omegat^2-kappa^2);

alpha=4*pi*r^3*e1*(epsav-e1)/(e1+(1/3)*(epsav-e1))/3.;

atilde=1i/(2*e1*w1*a^2);

if pol == 's'

    alspar=(dc+ac)/(8*pi*a^3)/e1+1i*omegat^2/a^2/2./w1;
    als=alpha/(1.-alpha*alspar);

    rfactor=omegat^2*e1*atilde*als;
else

    nok=w1^2*atilde*alpha/(1.-alpha*(dc+ac)/(8*pi*e1*a^3));
    noz=kappa^2*atilde*alpha/(1.-alpha*(dc-ac)/(4*pi*e1*a^3));

    rfactor=(noz-nok)/(1.-noz-nok);
end

shift=kappa+rfactor*rho13;

end

function [ c ] = bisect( a,b,au,aq,ap,epsi,delta,M )
%
%Description:
% The function bisect.m implements a bisection method algorithm
% to determine find the zeros of an expression.
%
% Inputs:
```

```
% a - initial point to begin algorithm
% b - secondary point to begin algorithm
% au,aq,ap - coefficients determined by polarization
% epsi, delta - error bounds
% M - maximum number of iterations
%
% Output:
% c - possible solution

escape=0;
k=0;

fa=solcon(a,au,aq,ap);
fb=solcon(b,au,aq,ap);

if sign(fa) == sign(fb)
    fprintf('Function does not change sign over sign interval')
end

while escape ~=1

    error=b-a;

    error=error/2;
    c=a+error;
    fc=solcon(c,au,aq,ap);

    if abs(fc) < epsi || abs(error) < delta || k >=M
        escape=1;
    end

    if sign(fa) ~= sign(fc)
        b=c;
        fb=fc;
    end
```

```
else
    a=c;
    fa=fc;
end

k=k+1;

end

if escape ~=1
    fprintf('Hard to find solution!');
end
```

```
function [ f ] = solcon( x,au,aq,ap )
%
% Description:
%
% The function solon.m contains the solution condition for the
% resonant waveguide mode of the bare multilayer structure. It
% is solved via bisect.m.

global omegat g e1 e2 e3 e4 D2 D3

q=real(aq*sqrt((e3-e1)*omegat^2-x^2));
beta=-imag(aq*sqrt((e3-e1)*omegat^2-x^2));
p=ap*sqrt((e3-e4)*omegat^2-x^2);

u=g*au*sqrt((e3-e2)*omegat^2-x^2);

part1=cot(x*D3);

num=beta^2*(x^2-u*p-(x^2+u*p)*exp(-2*u*D2))^2 ...
```

```
- 4*x*beta*u^2*(x^2+p^2)*exp(-2*u*D2) ...
+ ((x^2-u*p)*(q+u)-(x^2+u*p)*(q-u)*exp(-2*u*D2))^2;

denom=x*((beta^2*(x^2-u*p)-(x^2+u*p)*exp(-2*u*D2)) ...
* (u+p+(u-p)*exp(-2*u*D2)) ...
+ ((x^2-u*p)*(q+u)-(x^2+u*p)*(q-u)*exp(-2*u*D2)) ...
* ((q+u)*(u+p)+(q-u)*(u-p)*exp(-2*u*D2)));

part2=real(num/denom);

f = part1 - part2;

end
```

Appendix D

Copyright Releases

Permissions for the inclusion of portions of copyright materials are provided in this appendix. Permission was requested and granted to incorporate the development of the formalism of [43]. As the work presented in this thesis is an extension of the formalism developed in [43], the inclusion of such material was necessary.

Dear Mr. Travo,

Thank you for contacting The Optical Society.

OSA considers your requested use of its copyrighted material to be Fair Use under United States Copyright Law. It is requested that a complete citation of the original material be included in any publication.

Let me know if you have any questions.

Kind Regards,

Susannah Lehman

July 17, 2013

Authorized Agent, The Optical Society

To: pubscopyright

Subject: Permission request Doc. ID 174060

To Whom It May Concern,

I am requesting permission to include a modified portion of the article entitled "Metallic nanoparticles on waveguide structures: effects on waveguide mode properties and the promise of sensing applications," by T. Cheng, C. Rangan, and J. E. Sipe of J. Opt. Soc. Am. B, Vol. 30 (3), March 2013, pages 743-765 (Doc. ID 174060) in my MSc. thesis.

I am a student of Dr. C. Rangan and the project extends upon the original work. A discussion of the original formalism and approach used by the above article is thus necessary for a proper development of the new content. Of the original article portions from pages 746 - 755 and 762 - 763 would be used. Modifications made would be the removal of all figures and non-relevant equations.

Thank you for your time.

Best Regards,

Daniel Travo

Bibliography

- [1] L. Silberstein. The transparency of turbid media. *Journal of the Franklin Institute*, 204(6):815, 1927.
- [2] W.W. Lepeschkin. Longitudinal dispersion of infrared rays in optically empty and turbid media, and molecular weights of substances. *Journal of Physical and Colloid Chemistry*, 51(3):875–884, 1947.
- [3] J.M. Adams. Light extinction photometer for measurement of particle sizes in poly-dispersions. *Review of Scientific Instruments*, 39(11):1748–1751, 1968.
- [4] Gustav Mie. Contributions on the optics of turbid media, particularly colloidal metal solutions. *Annalen der Physik, Series IV*, 25:377–445, 1908.
- [5] Ernest O. Herreid. The Babcock Test; A Review of the Literature. *Journal of Dairy Science*, 25(4):335–370, 04 1942.
- [6] W. R. Calhoun, H. Maeta, S. Roy, L. M. Bali, and S. Bali. Sensitive real-time measurement of the refractive index and attenuation coefficient of milk and milk-cream mixtures. *Journal of dairy science*, 93(8):3497–3504, 08 2010.
- [7] D.M. Barbano, J.L. Clark, and C.E. Dunham. Comparison of Babcock and ether extraction methods for determination of fat content of milk: collaborative study. *Journal of the Association of Official Analytical Chemists*, 71(5):898–914, 1988.
- [8] J.M. Lynch, D.M. Barbano, and J.R. Fleming. Comparison of Babcock and ether extraction methods for determination of fat content of cream: Collaborative study. *Journal of AOAC International*, 79(4):907–916, 1996.
- [9] J.M. Lynch, D.M. Barbano, P.A. Healy, and J.R. Fleming. Effectiveness of temperature modification in decreasing the bias in milk fat test results between the Babcock and ether extraction methods. *Journal of AOAC International*, 86(4):768–774, 2003.
- [10] J.M. Lynch, D.M. Barbano, and J.R. Fleming. Modification of Babcock method to eliminate fat testing bias between Babcock and ether extraction methods (modification of aoac official methods 989.04 and 995.18): Collaborative study. *Journal of AOAC International*, 80(4):845–859, 1997.

- [11] M.E. Al Omar, R.H. Gough, and J.H. Gholson. Effect of milk sample condition on replicate milkfat tests analyzed by a milko tester mk ii. *J. Milk Food Technol.*, 37(7):372–376, 1974.
- [12] V.S. Packard Jr, R.E. Ginn, and J.R. Rosenau. A comparison of the Babcock, mojonier, and milko tester mark iii methods in the analysis of milkfat in cream. *J. Milk. Food. Technol.*, 36(10):523–525, 1973.
- [13] Jianwei Qin and Renfu Lu. Hyperspectral diffuse reflectance imaging for rapid, noncontact measurement of the optical properties of turbid materials. *Appl. Opt.*, 45(32):8366–8373, Nov 2006.
- [14] W. R. Calhoun, H. Maeta, A. Combs, L. M Bali, and S. Bali. Measurement of the refractive index of highly turbid media. *Opt. Lett.*, 35(8):1224–1226, Apr 2010.
- [15] Augusto García-Valenzuela, Rubén Barrera, Celia Sánchez-Pérez, Alejandro Reyes-Coronado, and Eugenio Méndez. Coherent reflection of light from a turbid suspension of particles in an internal-reflection configuration: Theory versus experiment. *Opt. Express*, 13(18):6723–6737, Sep 2005.
- [16] Wenping Guo, Min Xia, Wei Li, Jie Dai, Xiaohui Zhang, and Kecheng Yang. A local curve-fitting method for the complex refractive index measurement of turbid media. *Measurement Science and Technology*, 23(4):047001, 2012-04-01 2012.
- [17] Stefan Busse, Josua Kshammer, Stephan Krmer, and Silvia Mittler. Gold and thiol surface functionalized integrated optical machzehnder interferometer for sensing purposes. *Sensors and Actuators B: Chemical*, 60(2-3):148–154, 1999.
- [18] T.E. Plowman, J.D. Durstchi, H.K. Wang, D.A. Christensen, J.N. Herron, and W.M. Reichert. Multiple-analyte fluoroimmunoassay using an integrated optical waveguide sensor. *Analytical Chemistry*, 71(19):4344–4352, 1999.
- [19] W. Lukosz. Integrated optical chemical and direct biochemical sensors. *Sensors and Actuators: B. Chemical*, 29(1-3):37–50, 1995.
- [20] K. Kneipp, H. Kneipp, I. Itzkan, R.R. Dasari, and M.S. Feld. Surface-enhanced raman scattering and biophysics. *Journal of Physics Condensed Matter*, 14(18):R597–R624, 2002.
- [21] K.M. Hansen, H.-F. Ji, G. Wu, R. Datar, R. Cote, A. Majumdar, and T. Thundat. Cantilever-based optical deflection assay for discrimination of dna single-nucleotide mismatches. *Analytical Chemistry*, 73(7):1567–1571, 2001.
- [22] W.S. Bakr, A. Peng, M.E. Tai, R. Ma, J. Simon, J.I. Gillen, S. Flling, L. Pollet, and M. Greiner. Probing the superfluid-to-mott insulator transition at the single-atom level. *Science*, 329(5991):547–550, 2010.
- [23] J.E. Chomas, P. Dayton, D. May, and K. Ferrara. Threshold of fragmentation for ultrasonic contrast agents. *Journal of Biomedical Optics*, 6(2):141–150, 2001.

- [24] H. Arwin. Ellipsometry on thin organic layers of biological interest: Characterization and applications. *Thin Solid Films*, 377-378:48–56, 2000.
- [25] H.-J. Jordan, M. Wegner, and H. Tiziani. Highly accurate non-contact characterization of engineering surfaces using confocal microscopy. *Measurement Science and Technology*, 9(7):1142–1151, 1998.
- [26] T.J.A. Ilander, A.P. Leskinen, T.M. Raunemaa, and L. Rantanen. Characterization of diesel particles: Effects of fuel reformulation, exhaust aftertreatment, and engine operation on particle carbon composition and volatility. *Environmental Science and Technology*, 38(9):2707–2714, 2004.
- [27] G. Udupa, M. Singaperumal, R.S. Sirohi, and M.P. Kothiyal. Characterization of surface topography by confocal microscopy: I. principles and the measurement system. *Measurement Science and Technology*, 11(3):305–314, 2000.
- [28] K. Mbius, A. Savitsky, A. Schnegg, M. Plato, and M. Fuchs. High-field epr spectroscopy applied to biological systems: Characterization of molecular switches for electron and ion transfer. *Physical Chemistry Chemical Physics*, 7(1):19–42, 2005.
- [29] Michael McClimans, Charles LaPlante, David Bonner, and Samir Bali. Real-time differential refractometry without interferometry at a sensitivity level of 10⁻⁶. *Appl. Opt.*, 45(25):6477–6486, Sep 2006.
- [30] J. Rty and K-E Peiponen. Measurement of refractive index of liquids using s- and p-polarized light. *Measurement Science and Technology*, 11(1):74–76, 2000-01-01 2000.
- [31] A. Reyes-Coronado, A. Garca-Valenzuela, C. Snchez-Prez, and R. G. Barrera. Measurement of the effective refractive index of a turbid colloidal suspension using light refraction. *New Journal of Physics*, 7(1):89–89, April 2005.
- [32] J.V. Champion, G.H. Meeten, and M. Senior. Refractive index of particles in the colloidal state. *Journal of the Chemical Society, Faraday Transactions 2: Molecular and Chemical Physics*, 74:1319–1329, 1978.
- [33] G. H. Meeten. Refractive index errors in the critical-angle and the brewster-angle methods applied to absorbing and heterogeneous materials. *Measurement Science and Technology*, 8(7):728–733, 1997-07-01 1997.
- [34] G. H. Meeten and A. N. North. Refractive index measurement of absorbing and turbid fluids by reflection near the critical angle. *Measurement Science and Technology*, 6(2):214–221, 1995-02-01 1995.
- [35] A. J. Jskelinen, K. . Peiponen, and J. A. Rty. On reflectometric measurement of a refractive index of milk. *Journal of dairy science*, 84(1):38–43, 200101 2001.
- [36] Zhang Yingying, Lai Jiancheng, Yin Cheng, and Li Zhenhua. Determination of effective complex refractive index of a turbid liquid with surface plasmon resonance phase detection. *Appl. Opt.*, 48(7):1262–1267, Mar 2009.

- [37] R. Naraoka and K. Kajikawa. Phase detection of surface plasmon resonance using rotating analyzer method. *Sensors and Actuators, B: Chemical*, 107(2):952–956, 2005.
- [38] E.M. Vartiainen, T. Asakura, and K.-E. Peiponen. Generalized noniterative maximum entropy procedure for phase retrieval problems in optical spectroscopy. *Optics Communications*, 104(1-3):149–156, 1993.
- [39] E.M. Vartiainen and K.-E. Peiponen. Meromorphic degenerate nonlinear susceptibility: Phase retrieval from the amplitude spectrum. *Physical Review B*, 50(3):1941–1944, 1994.
- [40] K.F. Palmer, M.Z. Williams, and B.A. Budde. Multiply subtractive kramers-kronig analysis of optical data. *Applied Optics*, 37(13):2660–2673, 1998.
- [41] J. Brun, D. De Sousa Meneses, B. Rousseau, and P. Echegut. Dispersion relations and phase retrieval in infrared reflection spectra analysis. *Applied Spectroscopy*, 55(6):774–780, 2001.
- [42] In *Kramers-Kronig Relations in Optical Materials Research*, volume 110 of *Springer Series in Optical Sciences*. 2005.
- [43] T. Cheng, C. Rangan, and J. E. Sipe. Metallic nanoparticles on waveguide structures: effects on waveguide mode properties and the promise of sensing applications. *J. Opt. Soc. Am. B*, 30(3):743–765, Mar 2013.
- [44] Stefan A. Maier, SpringerLink, and Springer. *Plasmonics*. 2007.
- [45] U. Kreibig and M. Vollmer. *Optical properties of metal clusters*, volume 25. Springer-Verlag, New York, 1995.
- [46] Erik M. Vartiainen, Jarkko J. Saarinen, and Kai-Erik Peiponen. Method for extracting the complex dielectric function of nanospheres in a water matrix from surface-plasmon resonance data. *J. Opt. Soc. Am. B*, 22(6):1173–1178, Jun 2005.
- [47] R. Ruppin. Evaluation of extended maxwell-garnett theories. *Optics Communications*, 182(4):273–279, 2000.
- [48] J.C. Maxwell-Garnett. Colours in metal glasses and in metallic films. *Philos. Trans. R. Soc. London*, 203:385–420, 1904.
- [49] J.E. Sipe and R.W. Boyd. Nonlinear susceptibility of composite optical materials in the maxwell garnett model. *Physical Review A*, 46(3):1614–1629, 1992.
- [50] H.C. Van de Hulst. *Light Scattering by Small Particles*, 1957.
- [51] Rubén G. Barrera and Augusto García-Valenzuela. Coherent reflectance in a system of random mie scatterers and its relation to the effective-medium approach. *J. Opt. Soc. Am. A*, 20(2):296–311, Feb 2003.

- [52] L. Tsang and J.A. Kong. Effective propagation constants for coherent electromagnetic wave propagation in media embedded with dielectric scatters. *Journal of Applied Physics*, 53(11):7162–7173, 1982.
- [53] R.J. Birkett, A. Clark, and G.H. Meeten. The effects of cell windows on the optical reflectance of diffusely-scattering materials. *Colloids and Surfaces*, 24(2-3):259–263, 1987.
- [54] W.E. Vargas. Optimization of the diffuse reflectance of pigmented coatings taking into account multiple scattering. *Journal of Applied Physics*, 88(7):4079–4084, 2000.
- [55] A.A. Kokhanovsky, R. Weichert, M. Heuer, and W. Witt. Angular spectrum of light transmitted through turbid media: Theory and experiment. *Applied Optics*, 40(16):2595–2600, 2001.
- [56] Keith Alexander, Ainsley Killey, Gerald Meeten, and Malcolm Senior. Refractive index of concentrated colloidal dispersions. *Journal of the Chemical Society, Faraday Transactions 2: Molecular and Chemical Physics*, 77(2):361–372, 1981.
- [57] Ilpo Niskanen, Jukka Rätty, and Kai-Erik Peiponen. Complex refractive index of turbid liquids. *Opt. Lett.*, 32(7):862–864, Apr 2007.
- [58] W. Calhoun, H. Maeta, A. Combs, L. M. Bali, and S. Bali. Measurement of the refractive index of highly turbid media: reply to comment. *Opt. Lett.*, 36(16):3172–3172, Aug 2011.
- [59] K.-E. Peiponen, J. Rätty, and I. Niskanen. Measurement of the refractive index of highly turbid media: comment. *Opt. Lett.*, 35(24):4108–4108, Dec 2010.
- [60] Huafeng Ding, Jun Q. Lu, Kenneth M. Jacobs, and Xin-Hua Hu. Determination of refractive indices of porcine skin tissues and intralipid at eight wavelengths between 325 and 1557 nm. *J. Opt. Soc. Am. A*, 22(6):1151–1157, Jun 2005.
- [61] Jiri Homola, Ivo Koudela, and Sinclair S. Yee. Surface plasmon resonance sensors based on diffraction gratings and prism couplers: sensitivity comparison. *Sensors and Actuators: B.Chemical*, 54(1-2):16–24, 19990125 1999.
- [62] Alexandre A. Kolomenskii, Paul D. Gershon, and Hans A. Schuessler. Surface-plasmon resonance spectrometry and characterization of absorbing liquids. *Appl. Opt.*, 39(19):3314–3320, Jul 2000.
- [63] Cesar Rodriguez-Emmenegger, Oxana A. Avramenko, Eduard Brynda, J. Skvor, and Aldo B. Alles. Poly(hema) brushes emerging as a new platform for direct detection of food pathogen in milk samples. *Biosensors and Bioelectronics*, 26(11):4545–4551, 20110715 2011.
- [64] Ftima Fernandez, Daniel G. Pinacho, Francisco Snchez-Baeza, and M. P. Marco. Portable surface plasmon resonance immunosensor for the detection of fluoroquinolone antibiotic residues in milk. *Journal of Agricultural and Food Chemistry*, 59(9):5036–5043, 2011.

- [65] Nikolai G. Khlebtsov N.G. and Lev A. Dykman L.A. Optical properties and biomedical applications of plasmonic nanoparticles. *Journal of Quantitative Spectroscopy and Radiative Transfer*, 111(1):1–35, 201001 2010.
- [66] Chenxu Yu and Joseph Irudayaraj. Multiplex biosensor using gold nanorods. *Analytical Chemistry*, 79(2):572–579, 2007.
- [67] Katherine A. Willets and Richard P. Van Duyne. Localized surface plasmon resonance spectroscopy and sensing. *Annual Review of Physical Chemistry*, 58:267–297, 5 May 2007 2007.
- [68] Fook Chiong Cheong, Bo Sun, Rémi Dreyfus, Jesse Amato-Grill, Ke Xiao, Lisa Dixon, and David G. Grier. Flow visualization and flow cytometry with holographic video microscopy. *Opt. Express*, 17(15):13071–13079, Jul 2009.
- [69] F. C. Cheong, K. Xiao, and D. G. Grier. Technical holographic video microscopy. *Journal of dairy science*, 92(1):95–99, 200901 2009.
- [70] H. Mukundan, A. S. Anderson, K. M. Grace, N. Hartman, J. S. Martinez, and B. I. Swanson. Waveguide-based biosensors for pathogen detection. *Sensors*, 9(7):5783–5809, 2009.
- [71] Nimi Gopalakrishnan, Mads Brøkner Christiansen, and Anders Kristensen. Nanofiltering via integrated liquid core waveguides. *Opt. Lett.*, 36(17):3350–3352, Sep 2011.
- [72] D. Axelrod. Evanescent excitation and emission in fluorescence microscopy. *Biophysical Journal*, 104(7):1401–1409, 2013.
- [73] Craig F. Bohren and Donald R. Huffman. *Absorption and Scattering of Light by Small Particles*. John Wiley & Sons, New York, 1983.
- [74] Bruce T. Draine and Piotr J. Flatau. Discrete-dipole approximation for scattering calculations. *J. Opt. Soc. Am. A*, 11(4):1491–1499, Apr 1994.
- [75] Bruce T. Draine and Piotr J. Flatau. Discrete-dipole approximation for periodic targets: theory and tests. *J. Opt. Soc. Am. A*, 25(11):2693–2703, Nov 2008.
- [76] J. Vaillant, A. Crocherie, F. Hirigoyen, A. Cadien, and J. Pond. Uniform illumination and rigorous electromagnetic simulations applied to cmos image sensors. *Optics Express*, 15(9):5494–5503, 2007.
- [77] John D. Jackson. *Classical Electrodynamics Third Edition*. Wiley, third edition, August 1998.
- [78] Lev D Landau and Evgenij M Lifsic. *Electrodynamics of continuous media*. Elsevier [u.a.], Amsterdam [u.a.], 2009.
- [79] J. E. Sipe. New green-function formalism for surface optics. *J. Opt. Soc. Am. B*, 4(4):481–489, April 1987.

- [80] M. Sametband, I. Shweky, U. Banin, D. Mandler, and J. Almog. Application of nanoparticles for the enhancement of latent fingerprints. *Chemical Communications*, (11):1142–1144, 2007.
- [81] T. Karakouza, B.M. Maoz, G. Lando, A. Vaskevich, and I. Rubinstein. Stabilization of gold nanoparticle films on glass by thermal embedding. *ACS Applied Materials and Interfaces*, 3(4):978–987, 2011.
- [82] Y.-I. Su. A strategy for immunoassay signal amplification using clusters of immunogold nanoparticles. *Applied Surface Science*, 253(3):1101–1106, 2006.
- [83] M. Okumura, K. Tanaka, A. Ueda, and M. Haruta. The reactivities of dimethylgold(iii)-diketone on the surface of tio2 a novel preparation method for au catalysts. *Solid State Ionics*, 95(1-2):143–149, 1997.
- [84] P.a Wohlfart, J.b Wei, J.a Kshammer, C.b Winter, V.a Scheumann, R.A.b Fischer, and S.a Mittler-Neher. Selective ultrathin gold deposition by organometallic chemical vapor deposition onto organic self-assembled monolayers (sams). *Thin Solid Films*, 340(1):274–279, 1999.
- [85] J.a Kshammer, P.a Wohlfart, J.b Wei, C.b Winter, R.b Fischer, and S.a Mittler-Neher. Selective gold deposition via cvd onto self-assembled organic monolayers. *Optical Materials*, 9(1-4):406–410, 1998.
- [86] M. Kleefstra and G. C. Herman. Influence of the image force on the band gap in semiconductors and insulators. *Journal of Applied Physics*, 51(9):4923–4926, 1980.
- [87] Amitabha Bagchi, Rubén G. Barrera, and Ronald Fuchs. Local-field effect in optical reflectance from adsorbed overlayers. *Phys. Rev. B*, 25:7086–7096, Jun 1982.
- [88] J.E. Sipe. Bulk-selvedge coupling theory for the optical properties of surfaces. *Physical Review B*, 22(4):1589–1599, 1980.
- [89] J.E. Sipe. A new treatment of the growing wave problem in surface optics. *Solid State Communications*, 39(3):493–496, 1981.
- [90] J.E. Sipe and J. Becher. Surface energy transfer enhanced by optical cavity excitation: A pole analysis. *Journal of the Optical Society of America*, 72(2):288–295, 1982.
- [91] J.J. Saarinen, S.M. Weiss, P.M. Fauchet, and J.E. Sipe. Optical sensor based on resonant porous silicon structures. *Optics Express*, 13(10):3754–3764, 2005.
- [92] Daniel A. Travo, Ruby Huang, Taiwang Cheng, Chitra Rangan, Erden Ertorer, and Silvia Mittler. Experimental and theoretical issues of nanoplasmonics in medicine. In Mordechay Schlesinger, editor, *Applications of Electrochemistry in Medicine*, volume 56 of *Modern Aspects of Electrochemistry*, pages 343–379. Springer US, 2013.
- [93] Patrick Rooney, Asad Rezaee, Songbo Xu, Touraj Manifar, Abdollah Hassanzadeh, Ganna Podoprygorina, Volker Böhmer, Chitra Rangan, and Silvia Mittler. Control of surface plasmon resonances in dielectrically coated proximate gold nanoparticles immobilized on a substrate. *Phys. Rev. B*, 77:235446, Jun 2008.

- [94] A. K. A. Aliganga, I. Lieberwirth, G. Glasser, A. S. Duwez, Y. Sun, and S. Mittler. Fabrication of equally oriented pancake shaped gold nanoparticles by sam-templated omcvd and their optical response. *Organic Electronics*, 8(2-3):161–174, 2007.
 - [95] Hao Jiang, J. Sabarinathan, T. Manifar, and S. Mittler. 3-d fdtd analysis of gold-nanoparticle-based photonic crystal on slab waveguide. *Journal of Lightwave Technology*, 27(13):2264–2270, 2009 JULY1, 2009.
 - [96] Eric W. Weisstein. “square root.” from mathworld—a wolfram web resource, June 2013.
 - [97] P. B. Johnson and R. W. Christy. Optical constants of the noble metals. *Phys. Rev. B*, 6:4370–4379, Dec 1972.
 - [98] Pierre Berini. Bulk and surface sensitivities of surface plasmon waveguides. *New Journal of Physics*, 10(10):1–37, October 2008.
 - [99] Wen-Hui Yang, George C. Schatz, and Richard P. Van Duyne. Discrete dipole approximation for calculating extinction and raman intensities for small particles with arbitrary shapes. *The Journal of Chemical Physics*, 103(3):869–875, 1995.
 - [100] Ivn O. Sosa, Cecila Noguez, and Rubn G. Barrera. Optical properties of metal nanoparticles with arbitrary shapes. *The Journal of Physical Chemistry B*, 107(26):6269–6275, 2003.
 - [101] Traci Jensen, Lance Kelly, Anne Lazarides, and GeorgeC. Schatz. Electrodynamics of noble metal nanoparticles and nanoparticle clusters. *Journal of Cluster Science*, 10(2):295–317, 1999.
 - [102] Encai Hao and George C. Schatz. Electromagnetic fields around silver nanoparticles and dimers. *The Journal of Chemical Physics*, 120(1):357–366, 2004.
 - [103] LinLin Zhao, K. L. Kelly, and George C. Schatz. The extinction spectra of silver nanoparticle arrays: Influence of array structure on plasmon resonance wavelength and width. *The Journal of Physical Chemistry B*, 107(30):7343–7350, 2003.
 - [104] U. Fano. Effects of configuration interaction on intensities and phase shifts. *Phys. Rev.*, 124:1866–1878, Dec 1961.
 - [105] R.W. Wood. On a remarkable case of uneven distribution of light in a diffraction grating spectrum. *Proceedings of the Physical Society of London*, 18(1):269–275, 1901.
 - [106] Eric W. Weisstein. Bessel function of the first kind. from mathworld—a wolfram web resource., January 2012.
 - [107] I. S. Gradshteyn and I. M. Ryzhik. *Table of integrals, series, and products*. Elsevier/Academic Press, Amsterdam, seventh edition, 2007.
-

VITA AUCTORIS

NAME: Daniel-Anthony Travo

PLACE OF BIRTH: Windsor, Ontario

YEAR OF BIRTH: 1990

EDUCATION:

St. Thomas of Villanova Catholic Secondary School, LaSalle, Ontario
2004-2008

University of Windsor, Windsor, Ontario
2008-2012 B.Sc. [Honours] Medical Physics, Co-op with Thesis

University of Windsor, Windsor, Ontario
2012-2013 M.Sc. Physics